Montanuniversität Leoben

Grain boundary segregations in technically pure molybdenum

Diploma thesis

by

Katharina Babinsky

This thesis was carried out at the Department of Physical Metallurgy and Materials Testing at the Montanuniversität Leoben in cooperation with Plansee SE, Reutte, Austria.

Leoben, June 2013

Affidavit

I declare in lieu of oath that I wrote this thesis and performed the associated research myself, using only literature cited in this volume.

Eidesstattliche Erklärung

Ich erkläre an Eides statt, dass ich diese Arbeit selbständig verfasst, andere als die angegebenen Quellen und Hilfsmittel nicht benutzt und mich auch sonst keiner unerlaubten Hilfsmittel bedient habe.

Leoben, Juni 2013 Katharina Babinsky

Acknowledgments

First of all I want to thank Univ.-Prof. Dipl.-Ing. Dr.mont. Helmut Clemens and Priv.-Doz. Dipl.-Ing. Dr.mont. Harald Leitner for the possibility to write such an interesting thesis on the Department of Physical Metallurgy and Materials Testing at the Montanuniversität Leoben in collaboration with the company Plansee SE. Furthermore, I want to express my gratitude for the support and the assessment of the work.

My sincere thanks and appreciation goes to my supervisor Dipl.-Ing. Dr.mont. Sophie Primig. Due to the best support and encouragement I could complete my thesis successfully. Her great professionalism and her friendly manner helped me all time.

Furthermore, I would like to express my sincere appreciation to Dipl.-Ing. Dr.mont. Wolfram Knabl, Dipl.-Ing. Dr.mont. Alexander Lorich, Dipl.-Ing. Dr.mont. Michael Schober, and all other members of the “Plansee refractory team”. We always had very interesting and constructive discussions at our meetings.

Thanks to all my colleagues of the Department of Physical Metallurgy and Materials Testing for supporting my investigations. I will never forget the interesting discussion during our coffee breaks. Especially, I want to thank Dipl.-Ing. Dr. Francisca Mendez-Martin for her assistance with my analyses.

I also want to thank Prof. Hans-Olof Andrén for the great opportunity to accomplish my final investigations at his laboratory at the Department of Applied Physics on the Chalmers University of Technology in Gothenburg. Due to the perfect assistance of his group member Dr. Jonathan Weidow I got interesting results for my thesis.Thank you for the great time in Gothenburg.

Acknowledgments

Furthermore, this work was carried out with the support of the European Community. I appreciate the support of the European Research Infrastructure EUMINAfab (funded under the FP7 specific programme Capacities, Grant Agreement Number 226460) and its partner, the Karlsruhe Institute of Technology. The technical assistant of the Auger nanoprobe, Tobias Weingärtner, supported me during all my Auger analyses. Thank you very much!

I would also like to say "thank you" to all my friends for the great time in Leoben. You always supported me in any way and had an open ear for my problems. Thank you so much for the last five years.

A special thanks goes to my family, who have always supported me and backed me up in my decisions during my thesis. Due to my parents I got the chance to study in Leoben and to complete the master degree. Thank you for everything!

Contents

Abbreviations

Atom probe tomography	APT
Auger electron spectroscopy	AES
Body centered cubic	bcc
Focused ion beam	FIB
Transmission electron microscope	TEM
Glow discharge mass spectroscopy	GDMS
Scanning electron microscope	SEM
Atom probe field ion microscopes	APFIM
Low-energy electron diffraction	LEED
Ionization loss spectroscopy	ILS
Electron energy loss spectroscopy	EELS
Secondary ion mass spectroscopy	SIMS
Ion scattering spectroscopy	ISS
Ultra-high vacuum	UHV
X-ray photoelectron spectroscopy	XPS
X-ray absorption spectroscopy	XAS
X-ray emission spectroscopy	XES

Abstract

Molybdenum, a metal with excellent physical, chemical and mechanical properties, is an interesting material for applications e.g. in lighting-technology, high performance electronics, high temperature furnace construction and coating technology. However, its applicability as a structural material is reduced because of the poor oxidation resistance and a brittle-to-ductile transition at room temperature, which is influenced by the microstructure and the content of interstitial impurities. In this thesis, it was attempted to analyze grain boundary segregations in technically pure molybdenum to understand the influence of impurities on the resulting mechanical properties. Therefore, high sensitive analysis techniques such as atom probe tomography (APT), Auger electron spectroscopy (AES) and other chemical analysis methods were performed. APT is a powerful tool to study the concentration and location of segregations due to its almost atomic resolution for all elements. However, a site-specific sample preparation of grain boundaries with a dual focused ion beam/scanning electron microscope was required. Therefore, several methods such as the lift-out technique or the sharpening of electro-polished tips by focused ion beam were applied. The most applicable method was a combination of focused ion beam tip preparation with intermediate transmission electron microscope studies. Furthermore, AES analyses were carried out to compare the obtained results with the APT measurements.

Abstract (German)

Molybdän ist mit seinen einzigartigen physikalischen, chemischen und mechanischen Eigenschaften ein hervorragender Werkstoff für Anwendungen in der Lichtindustrie, in der Leistungselektronik, im Hochtemperaturofenbau und in der Beschichtungstechnik. Ein Nachteil dieses Metalls ist die schlechte Oxidationsbeständigkeit als auch der Spröd-Duktil-Übergang bei Raumtemperatur, welcher durch die Korngröße und den Grad an Verunreinigungen beeinflusst wird. In dieser Diplomarbeit wurden Korngrenzenverunreinigungen in Molybdän analysiert, um deren Einfluss auf die mechanischen Eigenschaften zu verstehen. Hochsensible Analyseverfahren wie Atomsondentomographie und Augerelektronenspektroskopie als auch weitere chemische Analysemethoden wurden angewendet. Aufgrund des nahezu atomaren Auflösungsvermögens der Atomsonde kann mit dieser Technik die Zusammensetzung der Segregationen sowie deren Ort in der Probe bestimmt werden. Durch den Einsatz von Focused Ion Beam Systemen ist es möglich ort-spezifische Probenpräparationen durchzuführen. Verschiedene Methoden wie zum Beispiel die Lift-out Technik sowie das Präparieren elektrolytisch hergestellter Spitzen mit Focused Ion Beam Systemen wurden angewendet. Die Focused Ion Beam Methode kombiniert mit Untersuchungen am Transmissionselektronenmikroskop zwischen den Präparationsschritten zeigte die beste Anwendbarkeit. Um die Ergebnisse der Atomsonde besser deuten zu können, diente die Augerelektronenspektroskopie als Referenzmethode.

1 Introduction

Molybdenum is a metal with excellent physical, chemical and mechanical properties for applications e.g. in lighting-technology, high performance electronics, high temperature furnace construction and coating technology. It belongs to the so-called refractory metals (molybdenum, tungsten, niobium, tantalum, etc.) and exhibits a body centered cubic (bcc) lattice, a melting point of 2620°C and a high stacking fault energy. Furthermore, a low vapor pressure, a high thermal and electrical conductivity and a low thermal expansion coefficient characterize this metal. It has a good corrosion resistance, however, at temperatures above 600°C a protective atmosphere or vacuum has to be used due to the formation of volatile MoO_3 [1–3]. The properties of pure molybdenum are summarized in Table 1.1.

Table 1.1: Physical properties of pure molybdenum. Temperature dependent properties are valid at room temperature [1].

Properties			
Atomic number	42	Lattice constant	0.3147 nm
Atomic mass	95.94 g/mol	Linear thermal expansion coefficient	$5.2*10^{-6}$ m/(m K)
Melting point	2620°C	Thermal conductivity	140 W/(m K)
Density	10.28 g/cm³	Specific heat	0.254 J/(g K)
Crystal structure	bcc	Elastic modulus	320 GPa

The majority of molybdenum products are produced via powder metallurgical processing [4]. Its fabrication and applicability as a structural material are limited because of the typical change of fracture behavior due to the brittle-to-ductile transition temperature near room temperature [5]. In the deformed state molybdenum is ductile at room temperature, but recrystallization leads to room temperature embrittlement which is believed to be caused by impurity segregations at grain boundaries [6]. Furthermore, it was observed that an increase in deformation leads to an increase in ductility because it is assumed that individual grain boundaries need to accommodate either less impurities per area with decreasing grain size or that the impurity atoms are forced inside the grains during deformation [6–8].

The intergranular fracture is typical for bcc metals, like iron and molybdenum, but the influence of interstitial atoms on the mechanical properties is not well understood. An essential tool to analyze grain boundary segregations is Auger electron

spectroscopy (AES). With this method, it is possible to detect monolayers of elements on a surface and to investigate the concentration and location of the impurities in the microstructure. Besides, the atom probe with its almost atomic resolution is a high sensitive tool to detect individual atoms within a needle shaped specimen. Today´s new techniques for the preparation of atom probe tips by focused ion beam (FIB) systems expand the areas of application of atom probe tomography (APT) to analyze grain boundaries with atomic resolution. Especially, with site-specific preparation, tips from a special region of interest in the bulk material can be produced. For an improved visibility of this region of interest in such tips transmission electron microscope (TEM) studies can support the sample preparation.

M.K. Miller et al. [8,9] studied the influence of impurities in welded molybdenum alloys by APT. However, technically pure molybdenum with no additional elements has not been examined so far.

In the present thesis, two different molybdenum sheets with different impurity concentrations were studied by FIB/APT and AES as a complementary technique. The main focus was to find the ideal preparation technique to analyze grain boundary segregations in molybdenum by APT. Additional measurements were performed in order to evaluate the feasibility of a combined FIB/TEM technique to produce specimens with grain boundaries in the first 100 nm of the tip.

2 State-of-the-art

2.1 Grain boundary segregations

Grain boundary segregations influence significantly the mechanical properties of metals with a bcc crystal structure as reported in [10,11]. These impurities either originate from the raw material or from the manufacturing and subsequent processing where they cannot be avoided completely. Investigations of the amount and location of the impurities are essential to understand their influence on the mechanical properties [12].

2.1.1 Structure of grain boundaries

As described by Gottstein [13], grain boundaries are two-dimensional lattice defects in a crystalline material and separate two region of a crystalline structure with different orientations. Four parameters describe the two-dimensional representation of a grain boundary as visible in Figure 2.1. The orientation relationship of two grains is described with the angle φ. Ψ defines the spatial orientation of the grain boundary planes. The translation vector t with its two components t_1 and t_2 characterizes the shift of the grains with respect to each other [14].
The dislocation-model is the most frequently used representation to describe grain boundaries. It explains a grain boundary as a network of dislocations. In metals the atoms built a regular periodical order in the transition zone of the grains boundaries [15].

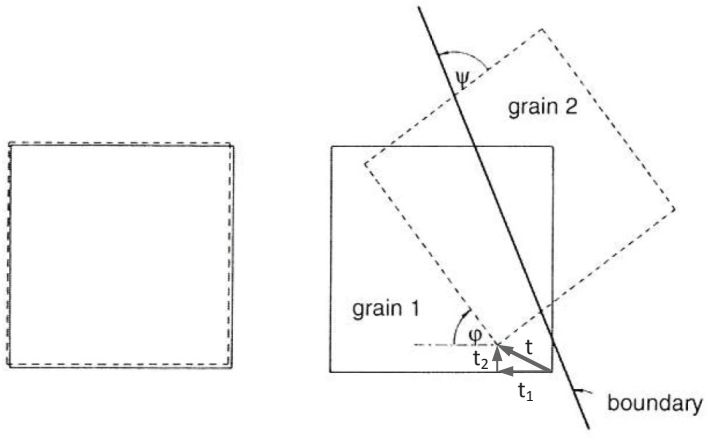

Figure 2.1: Schematic drawing of the four parameters that are necessary to define a two-dimensional grain boundary [14].

If dislocations arrange themselves one below the other, the orientation difference (misorientation) is low and, therefore, the tilt angle is below 15°. Such a low-angle boundary (subgrain boundary) is shown in Figure 2.2 (a).
Generally, low-angle tilt and twist boundaries exist. Symmetrical low-angle tilt boundaries are composed of a single set of dislocations. They are described with the following equation (b…Burger´s vector, D…dislocation spacing, θ…rotation angle):

$$\frac{b}{D} = 2\sin\frac{\theta}{2} \approx \theta \text{ [13]}$$

For asymmetrical low-angle tilt boundaries at least two sets of edge dislocations are necessary. Low-angle twist boundaries contain two sets of screw dislocations. Furthermore, the grain boundary energy increases with the misorientation. According to Figure 2.2 (b), the energy stays constant after achieving an orientation difference of 15°. The dislocation cores overlap whereby they lose their significance in the structure. At tilt angles over 15° high-angle boundaries are present [13].

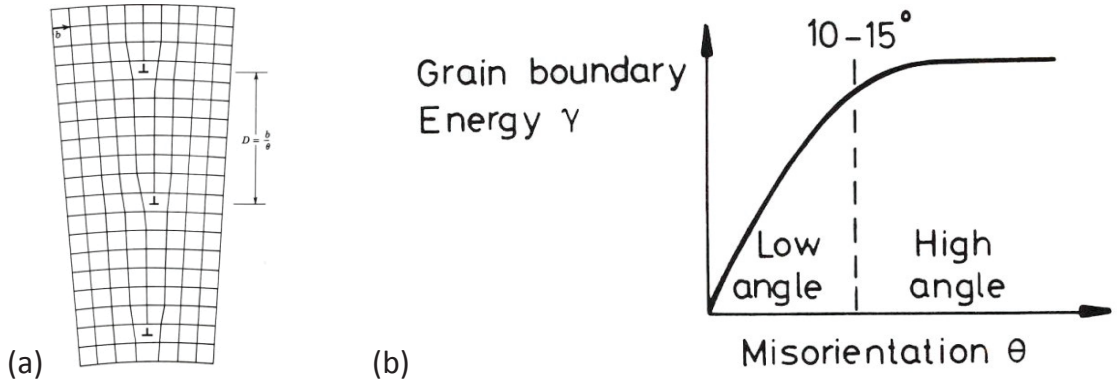

Figure 2.2: (a) Low-angle tilt boundary, arranged of edge dislocations [13]. (b) Misorientation versus grain boundary energy. The energy stays constant after achieving an orientation difference of about 15° [13].

These high-angle boundaries consist of regions of good and poor matching between the two grains. The atomic structure at the grain boundary is defined by relaxation of the atoms with dependence on the nature of the atomic bonding forces. The energy of the boundary reaches a minimum for an exact coincidence relationship (Figure 2.3). An increase can be observed when the orientation deviates from this due to the energy of the network of accommodating boundary dislocations [16]. However, also grain boundary segregations influence the grain boundary energy as shown in Figure 2.3 (a) in case of Ag–Au and Cu–Pb, investigated by Gleiter [15] and Sautter [17]. In this case, the segregations reduce the energy of the grain boundary. However, due to the change of

solute concentration at grain boundaries the energy could increase or decrease depending on the band structure variation and the boundary structure [17].

Furthermore, the mobility of the grain boundaries depends on the misorientation angle as shown in Figure 2.3 (b). In the range between 0.5° and 1.7° the grain boundary velocity is inversely dependent on the misorientation angle. In regime II the mobility increases with increasing angle before it stays constant in regime III. The motion of high-angle grain boundaries can be described by jumps of atoms across the grain boundary. Therefore, the mobility should be independent of the misorientation angle [18,19].

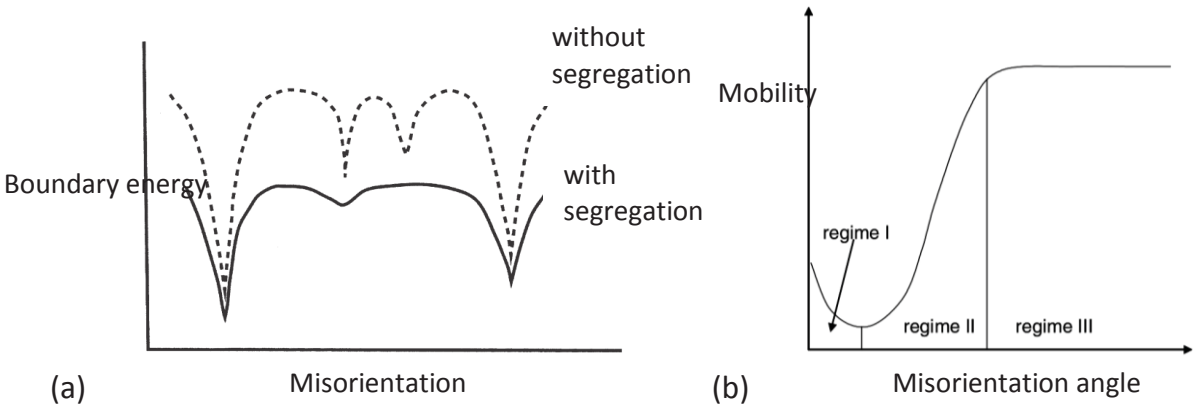

Figure 2.3: (a) Schematic drawing of the changes in the energy versus misorientation due to solute atoms, with and without segregation at the boundaries. The energy of the boundary is a minimum for an exact coincidence relationship [16]. (b) Schematic drawing of the expected dependence of the grain boundary mobility on the misorientation angle. Three different regimes can be distinguished [18,19].

2.1.2 Grain boundary properties and segregation processes

The behavior of grain boundaries is affected by four typical properties. Firstly, the grain boundaries can slide vertically to the tangential-plane (grain boundary displacement). Secondly, foreign atoms can accumulate at the boundaries and change the chemical composition of the alloy close to the grain boundaries (grain boundary segregations). Furthermore, the grain boundary planes can slide relative to each other if a shear stress is applied parallel to the grain boundary (grain boundary sliding). Finally, the grain boundaries can appear as a source or sink for lattice defect. In addition, grain boundaries influence the electric, magnetic, thermic and optic properties of a crystal [20].

In this thesis, grain boundary segregations in molybdenum are studied. In the last decades many investigation methods were developed to study grain boundary segregations. Direct methods as chemical analyses, activation analyses, AES, autoradiography, field ion microscopy, ion backscattering spectroscopy, luminescence

measurements or electron energy loss spectroscopy have allowed a direct measurement of the amount of segregated atoms [15]. Due to substitutional and interstitial atoms structural and chemical changes appear at the grain boundaries. Especially in iron, impurities as for example carbon, chromium and vanadium modify the properties. For example, phosphor leads to embrittlement in iron [10]. H. Gleiter [15] explained that the difference in the electron structure of the grain boundary area and the perfect lattice lead to segregation of alloying atoms. Between the grain boundary and the alloying atoms there is an electrostatic interaction which causes the accumulation or depletion of impurities at the grain boundary [15]. Messmer und Briant [21] postulated that electronegative impurities pull the charge away from the surrounding area of atoms and weaken the metal bonding at the grain boundary. Electropositive impurities add charge to the metal bonding and increase the cohesion. This model is in contradiction to the positive effect of the electronegative elements like boron and carbon in iron. Haydock [22] explained that a charge transfer between impurity and bulk material atoms influence the grain boundary strength. For his assumption the bonding between impurities and neighboring metal atoms has to be covalent and highly directional [23].
The segregation process itself is influenced by thermodynamical and kinetical effects. Two models describe this procedure. On the one hand, the McLean model [24,25] describes the accumulation of impurities to the grain boundaries over volume diffusion. On the other hand, Chang [26] specified the transportation over dislocation-pipe-diffusion. The segregations accumulate under equilibrium state, according to McLean, or under a time depending process as described by Chang. In Figure 2.4 the saturation time for the Chang- and McLean model for segregations of bismuth to copper grain boundaries is shown. The Bi concentration is plotted in monolayers (ML) [25].

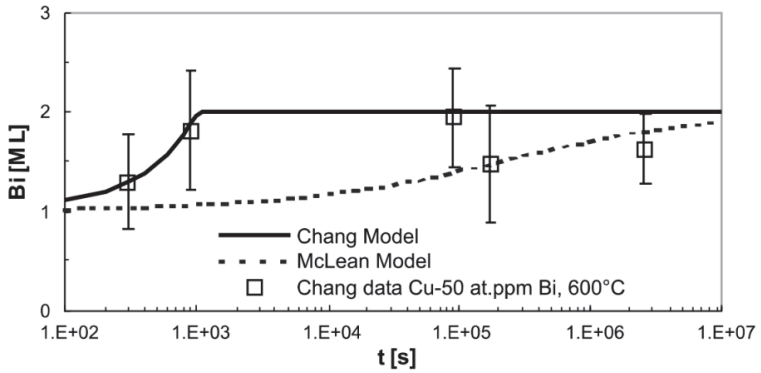

Figure 2.4: Comparison of the saturation time for the Chang- and McLean model for segregations of bismuth to copper grain boundaries. The bismuth (Bi) concentration is plotted in monolayers (MLs, 1 ML = 9,3 atoms/nm^2) over the time (t) [25].

2.1.3 Molybdenum and its grain boundary segregations

Intergranular fracture is typical for bcc metals such as molybdenum but the influence of interstitial atoms on the mechanical properties is not well understood so far [27]. In previous studies, A. Kumar and B.L. Eyre [6] investigated binary molybdenum-oxygen and ternary molybdenum-oxygen-carbon alloys. These alloys showed intergranular fracture due to oxygen segregations. However, their measurements revealed that carbon has a beneficial effect on the grain boundary strength. Suzuki et al. [28] investigated the effect of recrystallization on the ductility of high purity molybdenum. He confirmed the increase of grain boundary strength due to the addition of carbon. V. Krajnikov et al. [29] studied welded molybdenum based alloys and suggested that in annealed molybdenum carbon strengthens the grain boundaries and reduces the oxygen segregation. Further investigations on bcc metals like molybdenum and iron were performed by H. Kimura [11]. Recrystallized molybdenum showed intergranular fracture even if the grain boundaries were almost free of impurities. Other authors assumed that the brittleness is an intrinsic property of molybdenum [30–32]. M.K. Miller et al. [8,9] investigated welded molybdenum alloys to understand the influence of the elements zirconium, carbon and boron. His APT results showed no significant oxygen but zirconium, carbon and boron segregations at the grain boundaries. The depletion of oxygen at the grain boundary also causes a change in fracture mode from intergranular to transgranular failure [8]. However, B. Gludovatz [33] investigated the influence of impurities on the fracture behavior of the refractory metal tungsten. Among other findings he discovered phosphor at the grain boundaries. His results showed that intergranular fracture does not have a direct relation to the differences in grain boundary impurities. Effects like the shape of grains, grain size distribution, texture, dislocation density, and temperature influence the fracture behavior more than grain boundary segregations. B. Gludovatz assumed that small amounts of impurities have no direct correlation to the fracture behavior in tungsten, but they do have an impact on the ductility in the form of initiators of cracks or pores.

Although, M.K. Miller et al. [8,9] studied the influence of impurities in welded molybdenum alloys, technically pure molybdenum with no additional elements has not been examined so far. Surface analyses as well as APT should give information about grain boundary segregations in pure molybdenum.

2.2 Methods for grain boundary segregations analyses

In order to investigate grain boundary segregations in molybdenum different techniques are available. In the next sections methods of chemical analyses, several surface analysis techniques and the APT combined with FIB are presented.

2.2.1 Methods of chemical analyses

Analytical chemistry is used to study chemical compositions of bulk materials. Combustion analysis for carbon detection and carrier gas analysis for oxygen and nitrogen are commonly used. Inductively coupled plasma–atomic emission spectrometry is performed for most of the elements except of iron and tungsten which are measured over graphite tube-atomic adsorption spectrometry [4]. Furthermore, glow discharge mass spectroscopy (GDMS) has become a standard analysis for trace elements in the industry. A direct analysis of element compositions in solid samples is possible [34]. However, no micro-spot analyses are possible and non-flat samples such as screws and tubes are not suitable for direct mounting on the GD source. Porous materials such as foams and many plasma-sprayed ceramic coatings are difficult to handle because they are not vacuum tight. The glow discharge is a kind of plasma which is created by inserting two electrodes in a cell filled with a gas at low pressure. Commonly, the analysis is performed in argon but reactive gases are used as well. For the analysis a potential difference is applied at two electrodes which cause a gas breakdown. A plasma is formed and collisions in form of excitations and ionization of gas atoms occur. The ionization collision can be measured in a mass spectrometer. In reality, the glow discharge is a complex plasma with different kind of species like ions, atoms, electrons, photons etc. Due to the detection limits for all elements of the periodic table also high purity metals can be analyzed. The spectral interferences by various types of cluster ions are a problem of the GDMS measurements [34–37].

2.2.2 Atom probe tomography with focused ion beam preparation

Due to the small amounts of impurities in technically pure metals, APT is a very suitable method to study grain boundary segregations. The APT, with its almost atomic resolution and the possibility to detect all elements of the periodic system, combined with site specific preparation techniques of FIB systems, is a powerful tool for investigations of the content and location of grain boundary segregations [8,38–43].

The first investigations with the atom probe started in 1935 when Müller created the first microscope where a needle shaped specimen was placed in front of a phosphor screen. A voltage was applied and a field electron emission image was produced on the screen [44]. The atom probe field ion microscope (APFIM), the forerunner of the modern 3D atom probe was equipped with a time-of-flight mass spectrometer. The APFIM, a field ion microscope, is a combination of a field ion microscope and a mass spectrometer with the main removal process of field evaporation [41,44]. Due to the small acceptance angle of the mass spectrometer new variants were developed as for example the three-dimensional atom probe. The instrument produces three-dimensional images of the atoms on the specimen by recording the coordinates of the field evaporated atoms which fly towards the two-dimensional position-sensitive detector. Each atom from the specimen surface evaporates and exposes the next layer. The sequence of atom hits on the detector are used to track both the serial evaporation of atoms in a given layer and the serial evaporation of the layers [42,44]. The latest generation of atom probes are local electrode atom probes (LEAP®) which were commercially introduced by Kelly et al. [44] in 2003. They consist of a local electrode in close proximity to the specimen as shown in Figure 2.5. Individual tips may be field evaporated with a voltage pulse superimposed on the standing voltage or by a laser pulse that momentarily increases the temperature of the apex region so that field evaporation occurs on the standing voltage. With local electrodes lower-amplitude standing and pulse voltages are possible and the field of view is increased [41].

A state-of-the-art atom probe works with a time-to flight mass spectrometer with a point projection microscope capable of atomic scale imaging. The measurements are performed by applying a standing voltage on the apex of a sharp specimen at a cryogenic temperature whereby a high electrical field is created on the top of the tip. The atom probe can be applied in voltage and laser mode. For voltage mode, additional voltage pulses are set between the specimen and the local electrode (Figure 2.5) whereby field evaporation occurs and the ions are accelerated to the imaging detector.

To analyze the chemical composition the flight time can be measured and used for calculation of the mass-to-charge ratio. The magnification, η, is described with:

$$\eta = \frac{d}{b * r}$$ [41]

d … specimen-to-detector distance

b … projection parameter known as the image compression factor

r … specimen radius of curvature, which generally increases during the experiment

The position of the atoms in the specimen can be analyzed by the incidence point of the ions on the detector.

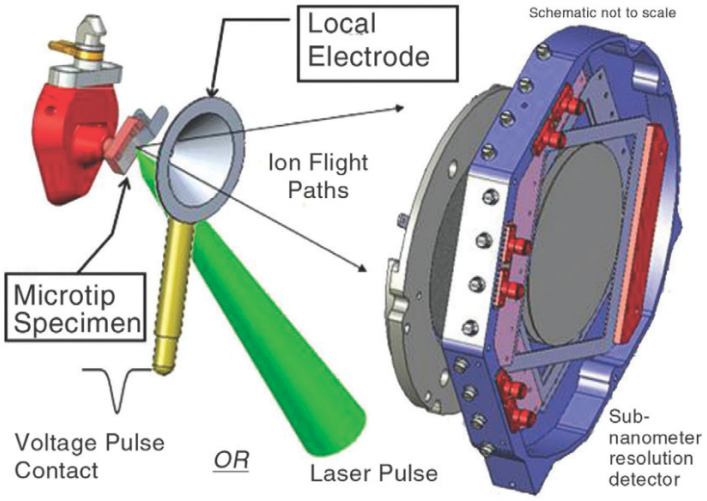

Figure 2.5: Schematic diagram of a local electrode atom probe with a cryogenically cooled multi-tip array specimen. Individual tips may be field evaporated with a voltage pulse superimposed on the standing voltage or by a laser pulse that momentarily increases the temperature of the apex region so that field evaporation occurs on the standing voltage [43].

An electrical conductivity is required for the use of voltage pulses which cause limits in the application of specimen materials. The specimen must have an electrical conductivity of more than 10^2 S/cm [44]. For nonelectrical materials short laser pulses (< 1 ns) can be used. Voltage pulsing creates field evaporation at a constant temperature by increasing the applied field. Laser pulses generate field evaporation at a constant field by raising the temperature. Laser pulsing opens up the field of applied specimen materials, however, the specimen preparation still causes problems [43,45].

The APT is used for a wide field of applications. Multiphase materials, segregations at dislocations or grain boundaries as well as precipitates can be studied with atomic resolution. Furthermore, investigations of interfaces in multilayer films are possible. In addition, each element of the periodic system can be detected out of a specimen with any chemical composition. The three-dimensional compositional imaging at the nanoscale of buried features, the high analytical sensitivity and the excellent image resolution make APT to a strong tool. APT achieves a spatial resolution of around 0.3 nm which makes it to an outrider in comparison to other scientific instruments. APT has a wide field of view. About 250000 atoms per atomic layer can be recorded. The sensitivity for interfacial segregations is around 40 appm/atomic layer and for bulk materials

around 10 appm or better. The sensitivity is typically limited by the background signal. However, an atom probe also has its limitations as for example the specimen preparation. Furthermore, the high mechanical stresses in the specimen near the apex influence the measurement significantly. Specimen fracture is common in atom probes when the cohesive strength of the material is achieved. The stress in the specimen increases with the square of the applied field. Lower fields, for example by applying laser pulsing, can reduce the fracture of the tips. Ideal atom probes detect all atoms but in reality this is not possible. With a microchannel plate, modern atom probes have a detection efficiency of 60% [44]. A LEAP 3000X HR from Cameca equipped with a reflectron has a detection efficiency of > 35% [46]. Additionally, the APT applications are limited by the analyzed volume. Nowadays, the image data sets are 100 nm diameters by 100 nm in depth with 10^7-10^8 atoms. The APT is an “out-looking” technique but there must be major advances that simplify, facilitate and automate specimen preparations [44].

The geometry of an atom probe tip must be well defined. It should be a needle shaped specimen with a taper angle of < 10° and a top radius of 50 to 150 nm [44]. The small apex radius is necessary to produce the high field for the field evaporation. A uniform cross-section is required for an accurate reconstruction of the tip. Furthermore, the low taper-angle allows the analyzation of a significant depth before the maximum voltage is exceeded [41]. High quality specimen surfaces should not exhibit any protrusions in their surroundings for a successful APT analysis [39,44].
In the past, electro-polishing was the preferred technique to create needle-shaped specimens [41,44,47–50]. The main process is the reaction of the specimen with an electrolyte influenced by the electrical driving force. The entire process is described in chapter 3.2.2. The active electrolyte, solvent, electrolyte concentration, solution viscosity, temperature, type, and magnitude of voltage, immersion method, solution container (material and size), counter electrode (material and geometry), shielding, and washing procedure have an influence on the polishing procedure [49]. Furthermore, pulse polishing can be used to remove very small amounts of the material to bring special region of interest into the first 100 nm of the tip [40,44]. However, material with insufficient electrical conductivity as well as powders, flakes, surface films, and implanted regions are not suitable for this method. Also phases, as for example carbides and borides, have different polishing rates and can protrude out of the final tip as shown

in Figure 2.6. Additionally, electro-polished tips can exhibit non-circular cross-sections (see Figure 2.6) [51].

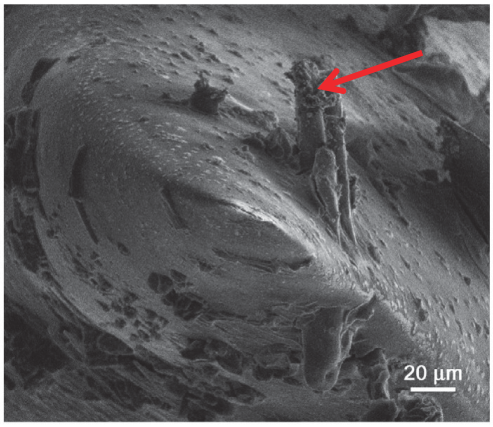

Figure 2.6: Example of an electro-polished iron-based bulk metallic-glass specimen that exhibits a non-uniform cross section and phases (red arrow) that are resistant to the electro-polishing process [51].

Nowadays, it is possible to produce specimens out of site-specific regions of interest due to application of FIB systems [45]. Furthermore, FIB preparation methods increase the facilities of possible specimen material. With this technique, site-specific specimen preparations of features as grain boundaries are possible for further APT or TEM analysis [40,44].

The FIB is called the “Swiss Army Knife” in microscopy [52]. The FIB operates with the same principle as a SEM. High-energy ionized atoms (ions) of a relatively massive element are focused in a beam on a sample surface for the purpose of imaging, etching or milling. The equipment of the FIB with a platinum/tungsten gas injection system deposition is also possible. Today´s FIBs are based on high-brightness gallium liquid-metals ion sources. Furthermore, dual FIB/SEM instruments give the opportunity to switch between ion and electron mode. The ion beam is predominately used for sputtering and the electron beam for imaging [53]. The FIB is mostly used for TEM and APT specimen preparation, for imaging, 3D tomography, and micromachining. However, the use of a high energetic beam of ions can cause artefacts as for example “waterfalling” or “curtaining” [52]. Furthermore, gallium atoms are implanted into the first 10-30 nm of the surface. Gallium atoms are larger than most of the transition elements and cause internal stresses. This can lead to failure during APT analysis due to hydrostatical pressure. Furthermore, the gallium intermixes phases and crystalline regions may turn into amorphous ones. Therefore, platinum or tungsten layers are used to protect the surface [54].

Today´s state-of-the-art FIB instruments are suitable for many processes:

a) *Imaging with 5 nm or better spatial resolution using secondary electrons or secondary ions, exhibiting a number of novel contrast mechanisms.*
b) *Creating a precise cut or cross-section from a few tens of nanometers to a few hundreds of micrometers in size, with positional placement accuracy on the order of 20 nm (and in many cases tilting the specimen in-situ for immediate imaging).*
c) *Introducing several different gases into the vacuum chamber to either (i) deposit a range of materials up to 20 µm or more over areas ranging from the sub-micrometers to tens of thousands of square micrometers or (ii) selectively etch of one material rapidly while barely affecting another* [55].

Many different FIB methods have been used to cut out atom probe tips. The most common ones are the lift-out technique, the post or moat and cut-out method. In all methods, a needle-shaped tip is produced by using different steps of milling procedure and sharpened in an annular milling process as described in chapter 3.2.1.
Applying the post/moat method, a platinum cap is deposited on the region of interest and a large annular region around this cap is removed as visible in Figure 2.7. As a final step, annular milling is performed. Redeposition, long milling times as well as the alignment problems of the tip in the atom probe limit this method as a suitable one [54].

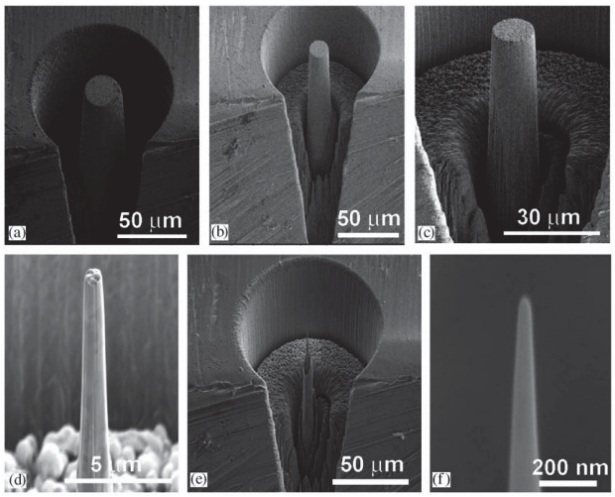

Figure 2.7: FIB-based moat method to prepare an atom probe specimen at a selected location. (a) The central post and the moat after the first rough mill, (b) and (c) general views after additional rough milling stages, (d) the central post after the rough milling stages, (e) after annular milling into a sharp needle, and (f) the apex region of the final atom probe specimen [54].

In case of the cut-out technique the milling requirements are reduced by grinding the sample firstly to form a thin wedge. This process removes most of the bulk material. Furthermore, a region of interest is selected and triangular sections are removed by using line cuts.
In the final step, annular milling is performed. The procedure is shown in Figure 2.8. This method is applied when a quick fabrication out of a bulk material is necessary and electro-polishing is not possible. This technique is also suitable for site-specific specimen fabrications however, the lift-out technique has more flexibility in this case [56].

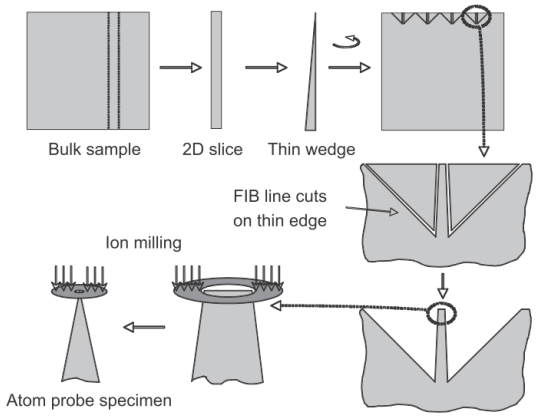

Figure 2.8: The cut-out method of specimen preparation [56].

The lift-out technique proposed by Miller [51,54] is used to fabricate tips out of the bulk material with special feature such as grain boundaries in the apex region of the needle shaped specimens. It is a perfect method for site-specific preparation of low volume fraction phases, grain boundaries, inhomogeneous microstructures etc. It is also possible to analyze surface films, multilayers and implanted or embedded layers [51]. The entire lift-out process is described in chapter 3.2.1. To study grain boundaries in the atom probe this tip preparation technique is the most common one. For example, P. Felfer et al. [38], F. Pérez-Willard et al. [39], R. Rachbauer et al. [57] and J.M. Cairney et al. [58] used and improved this technique.

2.2.3 Surface analysis

Besides APT, surface analysis methods are an essential tool to analyze grain boundary segregations. For surface analyses mostly particles such as electrons, photons, atoms, molecules or ions are used. Electrons have the widest application due to many reasons: Electrons can be easily focused into a beam and the energy can be varied easily with changing the potential. In addition, they are efficiently detectable. Finally, they disappear

from the vacuum after the surface analysis. However, high vacuum conditions are required for a good electron spectroscopy analysis. Furthermore, the electrons influence the surface, for example due to chemical reactions. Frequently oxygen and carbon deposition occur in poor vacuums. The information depth is also depending on the electron energy and material [59].

In electron scattering spectroscopies a primary electron beam is used to get a secondary electron signal. This signal is composed of coherent and incoherent elastically scattered electrons, inelastically scattered electrons, primary ionized electrons, and Auger electrons. The coherent and incoherent elastically scattered electrons are used for electron diffraction and SEM. Low-energy electron diffraction (LEED) is widely used for investigations of surface structures [59]. The primary ionized electrons and inelastically scattered electrons are detected and analyzed during electron scattering spectroscopies. Spectroscopy based on the analysis of ionized electrons is ionization loss spectroscopy (ILS) and that based on the analysis of inelastically scattered electrons is electron energy loss spectroscopy (EELS). The Auger electrons are analyzed in the AES [60].

During secondary ion mass spectroscopy (SIMS) the ion beam (positive or negative ions) is focused on a sample surface with a sufficient energy to ionize surface atoms. These ions are accelerated, focused and analyzed by a mass spectrometer to get information about the composition and chemistry of the surface. Most of the removed atoms and molecules are neutral but a percentage is ionized and, therefore, measured. This technique is typically performed for measurements of atomic monolayers on materials surfaces. SIMS has a high sensitivity for measurement of samples with low concentration levels (down to ppb levels) but not all elements can be analyzed quantitatively [61,62]. However, SIMS is a strong tool for surface analysis. It was used in the past, for example, for the investigation of doped tungsten [63].

In ion scattering spectroscopy (ISS) the ions are used as incident and detected species. Ions are scattered from the surface and their energy is measured. The technique is more sensitive to outermost atomic layers whereby a greater surface sensitivity is possible. The interpretation of the spectra is related to the energy loss of the incident ions and the masses of the surface atoms the ions have interacted with. The scattered intensities are measured over scattering angle and energy loss. Helium is used as favored incident beam due to its low mass. Furthermore, neon and argon are utilized for better mass resolution to analyze samples containing higher mass number elements. However, a greater amount of surface damage is caused by the use of argon and neon. Time-of-flight

analyzers are used commonly. For a good surface sensitivity it is necessary that the outermost surface is not destroyed. ISS gives no direct quantitative information about the composition. The intensities can be compared with ones from pure elements but normally ISS is used for determining surface compositions [61].

AES is a strong tool to detect fractions of monolayers of elements on a surface to investigate the concentration and location of impurities in the microstructure. The measurement is carried out as a function of the electron kinetic energy. The element of the material is distinguished by identifying the energy position of the Auger peaks and the concentration over the intensity of its peaks. Due to the surface specificity and the high spatial resolution, this method has widely used applications. Pierre Auger described this process first in 1925 [64]. Except of hydrogen and helium, every element can be detected. An Auger spectrometer consists of an ultra-high vacuum (UHV) system, an electron gun, a scanning electronics for imaging, an energy analyzer, and a computer for data storage and data processing. In addition, an ion gun can remove contaminated surface layers. AES belongs to the core-level spectroscopy as well as X-ray photoelectron spectroscopy (XPS), X-ray absorption spectroscopy (XAS) and X-ray emission spectroscopy (XES) due to the creation and decay of core holes [65]. The Auger process starts by creation of an ion (ejection of a core electron) with an inner shell vacancy (a core hole) due to interaction with an electron, a photon or an ion. The Auger electron is emitted when an electron from a higher energy level fills the inner shell vacancy. The kinetic energy of this emitted Auger electron exhibits information about the chemical properties of the atom. The Auger process is shown in Figure 2.9.

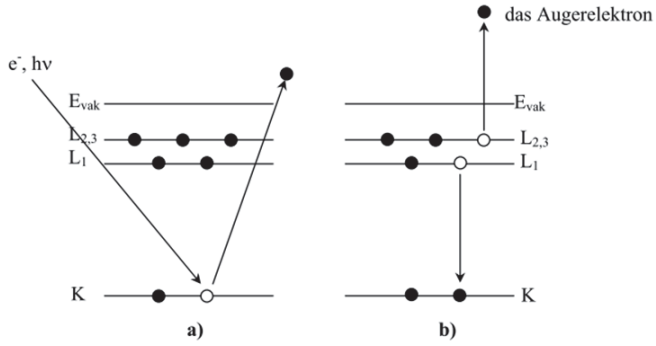

Figure 2.9: The AES process: (a) ionization of a deeper shell (K) with an electron or photon beam (b) emission of an Auger electron due to the release of energy after the transition of an electron from the L 1 to the ionized K shell [66].

The analysator records the electron and the kinetic energy is measured. Auger electron emission and X-ray fluorescence (a photon is emitted) are the two possible relaxation

mechanisms of an excited ion. Auger electron emission is rather used for low energy transitions (low atomic numbers). Auger electrons are activated close to the surface but also below. However, just an electron close to the surface leaves the material without energy loss and can be used for the analyses. Electrons which undergo inelastic processes before leaving the material lose kinetic energy and do not contribute [67].
The specimen preparation is simpler than for atom probe analysis and an information depth of several atomic layers to several ten monolayers is possible. This makes AES a strong surface analyzation technique. The detection limit for elementary analysis of solid states is 0.1 to 1 at. %. For the AES procedure two processes are important: the stimulation of an atom and the analysis of the emitted electron. In most of the cases the stimulation is caused by an electron beam with an acceleration voltage of 1 to 10 kV. The excitation current is around nA up to µA. The lateral resolution of AES is around 10 nm. At the detection limit of 0.1 at. % the analysis of 50 atoms on the surface is possible [66].
A good spatial resolution, the lateral resolution on the sample surface and the resolution in the depth are important. The lateral resolution for AES is limited by the diameter of the incoming electron beam [68]. AES is the most frequently used method for surface analyses. However, small signals are difficult to identify as well as overlaps of peaks [59].
In Table 2.1 XPS, AES, SIMS, and ISS are compared to each other.

Table 2.1: A comparison of the principle characteristics of XPS, AES, SIMS, ISS [61].

	Technique			
Characteristics	XPS	AES	SIMS	ISS
Probe species	X-ray	e^-	ion	ion
Detected species	e^-	e^-	ion	ion
Sensitivity	0.1%	0.1%	ppm-ppb	few% to 0.001%
Depth sensitivity	< 1 nm	< 1 nm	1 ml (static)*	1 ml*
Depth resolution	2-5 nm	2-5 nm	> 2 nm	>2 nm
Spatial resolution	few mm – 10 µm	100 nm	100nm	0.1-1 mm

*ml…monolayer

AES has a good sensitivity as well as high spatial resolution. Furthermore, the incoming electrons do not damage the surface as much as the used ions in SIMS or ISS. AES makes it possible to study the location and amount of impurities at grain boundaries. Therefore, AES was chosen in the present thesis as surface analysis method. Additionally, B. Gludovatz [33] successfully investigated the influence of impurities on the fracture behavior of tungsten with AES.

3 Experimental

3.1 Investigated material

The samples for the APT und AES analysis were taken out of two technically pure molybdenum sheets with the main difference in the potassium content. Table 3.1 summarizes the chemical composition of sheet 1 and 2. It was determined by using different analysis methods which are available at Plansee SE (a) and additionally by GDMS (b). The absolute accurateness of GDMS is typically +/- factor of 2. Especially, to study potassium segregations at grain boundaries sheet 2 was selected due to the increased potassium content. Oxygen, for example, has a really low solubility in molybdenum and, therefore, could accumulate at the grain boundaries [69].

Table 3.1: Chemical compositions of the two sheets determined by (a) Plansee SE and (b) by GDMS. Sheet 2 has an increased potassium content.

(a) Plansee SE Analyses		
Sample Element	Sheet 1 [µg/g]	Sheet 2 [µg/g]
C[a]	11	11
O[c]	19	31
La	<5	< 5
K[b]	7	21
Ba[b]	2	2
Co[b]	2	-
Cr[b]	3	2
Cu	3	2
Fe[b]	3	6
W[b]	143	150
Ti[b]	-	2

(b) GDMS Analyses		
Sample Element	Sheet 1 [µg/g]	Sheet 2 [µg/g]
C	< 8,5	< 6,5
O	≤ 12	< 5,9
N	< 1,3	< 0,4
K	4	19
Ba	1,0	2,2
P	2,4	1,2
La	0,02	0,4
Fe	3,7	3,2
Si	1,1	1,3
Mg	0,9	1,1
Al	0,2	0,2
Ca	0,2	0,3
S	0,09	0,08
W	120	140

[a] Combustion analysis
[b] Inductively coupled plasma–atomic emission spectrometry
[c] Carrier gas analysis
[d] Graphite tube-atomic adsorption spectrometry

For GDMS Analyses:
< below detection limit
≤ value not stable

For the APT measurements the as-deformed and the recrystallized states of each plate were analyzed. In case of the AES analyses only the recrystallized sheets were used. Table 3.2 shows an overview of the samples of the molybdenum sheets with their thickness. Furthermore, the hardness values for the as-deformed and recrystallized states of both sheets are listed.

Table 3.2: Overview of the two molybdenum sheets with their thickness. The as-deformed and recrystallized states are shown with their hardness values.

Sample material	Sheet 1	Sheet 2
Thickness	40 mm	48 mm
State	Hardness [HV10]	Hardness [HV10]
As-deformed	209	216
Recrystallized	175	168

The sheets were produced by cold-isostatic pressing of molybdenum powder followed by a conventional sintering process. During the subsequent hot-rolling process, the final passes were carried out to assure a sufficient degree of deformation (>60%) for complete recrystallization upon annealing. This subsequent recrystallization annealing was performed for 2 h at 1300°C in hydrogen atmosphere. The microstructure of sheet 1 in the as-deformed and recrystallized state was studied by electron channelling contrast imaging (ECCI) [70] in a Zeiss Evo 50 SEM and is shown in Figure 3.1. Figure 3.1 (a) shows the as-deformed microstructure with recovered subgrains. Such a microstructure consists of both, low- and high angle boundaries. During annealing at 1300°C for 2h this specimen did not recrystallize completely. Therefore, the sample was re-annealed for 2h at 1500°C. This additional heat treatment led to completely recrystallization with a grain size of ~ 48 µm parallel to the rolling direction as shown in Figure 3.1 (b).

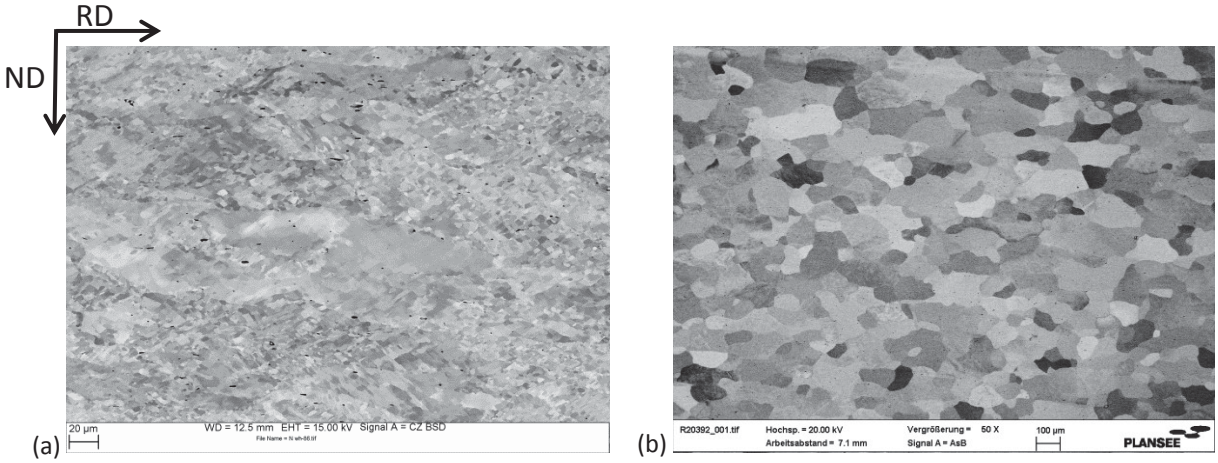

Figure 3.1: Microstructure of sheet 1 in the (a) as-deformed state and (b) recrystallized state as obtained by ECCI [70]. RD and ND indicate the rolling and the normal direction.

In Figure 3.2 the microstructure of sheet 2 in the as-deformed condition and recrystallized state as obtained by ECCI [70] is shown. The microstructure in Figure 3.2 (a) shows a recovered subgrain structure. Figure 3.2 (b) shows the microstructure of sheet 2 after subsequent annealing at 1300°C for 2h. The sufficient degree of deformation during hot rolling has led to completely recrystallization. The recrystallized grain size of sheet 2 was ~ 55 µm parallel to the rolling direction. Only high angle boundaries are present in the recrystallized structure.

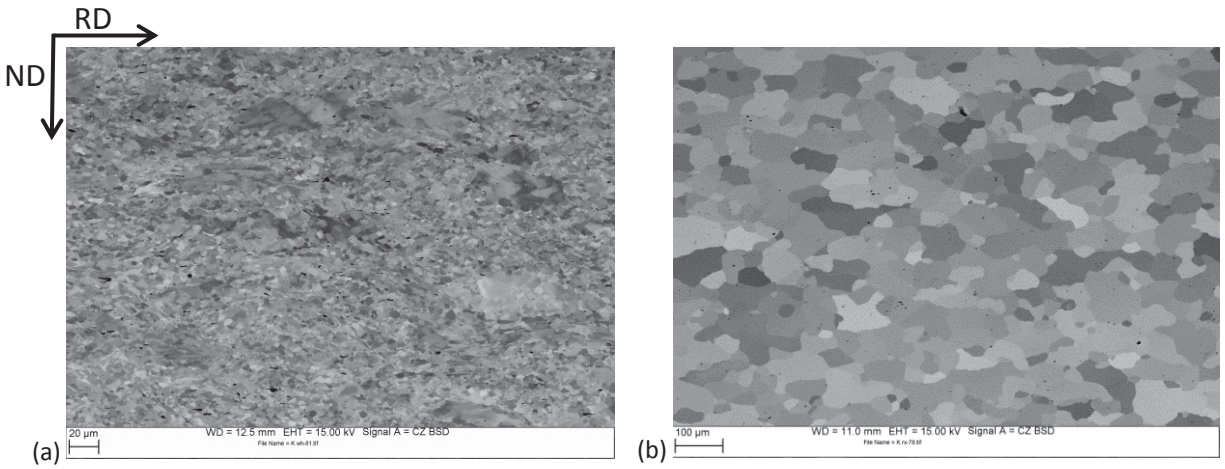

Figure 3.2: Microstructure of sheet 2 in the (a) as-deformed state and (b) recrystallized state studied by ECCI [70]. RD and ND indicate the rolling and the normal direction.

For the further APT tip preparation the microstructure, especially the grain sizes, played a significant role. The recrystallized state was used for the lift-out technique due to the good visibility of the grain boundaries as shown in Figure 3.1. and Figure 3.2. For the electro-polished tips the recrystallized state and as-deformed states were taken.

3.2 Tip preparation for the APT measurements

For atom probe tip preparation three different techniques were applied. Firstly, the lift-out technique proposed by Miller [51,54] was used. Secondly, electro-polished tips were produced and sharpened with the FIB. Finally, a FIB/TEM combination was applied for the fabrication of tips with a grain boundary in the first 100 nm of the tip.

3.2.1 Lift-out technique

The lift-out technique as proposed by Miller [51,54] gives the opportunity to fabricate tips with a grain boundary present in the bulk material. For this method the recrystallized state of sheet 1 and 2 was used (Figure 3.1 and Figure 3.2)

The FIB preparation was performed on a FEI Versa 3D DualBeam (FIB/SEM) microscope with a platinum gas injection system and an Omni probe 100-1 micromanipulator. The preparation was carried out with an acceleration voltage of 30 kV and a suitable current for a balance between re-deposition and cutting time. To protect the region of interest from gallium implantation, a platinum layer was deposited on the surface as shown in Figure 3.3. The progression of the grain boundary under the surface was unknown. For example, it could be possible that the grain boundary ran out of the wedge just below the surface.

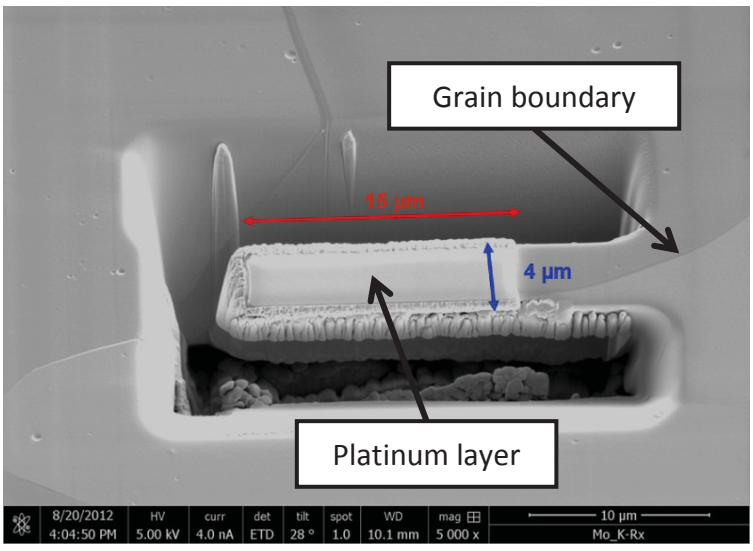

Figure 3.3: Lift-out technique for the molybdenum tip preparation of a wedge with a grain boundary. The grain boundary and the platinum layer are marked with arrows. The progression of the grain boundary under the surface is not visible.

After the clearance cut, the wedges were lifted out with the micromanipulator and transferred to a post which was a silicon needle pad or an electro-polished molybdenum tip [41,44,47–50]. The samples were attached to the post with platinum deposition weld. In Figure 3.4-Figure 3.17 the single steps of the lift-out-technique [51,54] are shown. Each step is described in detail:

The recrystallized microstructure of sheet 2 is shown in Figure 3.4 (a). A straight and clearly visible grain boundary was selected for the lift-out technique. This grain boundary is marked with an arrow in Figure 3.4 (a). To protect the region of interest, a platinum layer was deposited on the surface. The pattern (15 x 3 µm²) for the deposition is shown in Figure 3.4 (b).

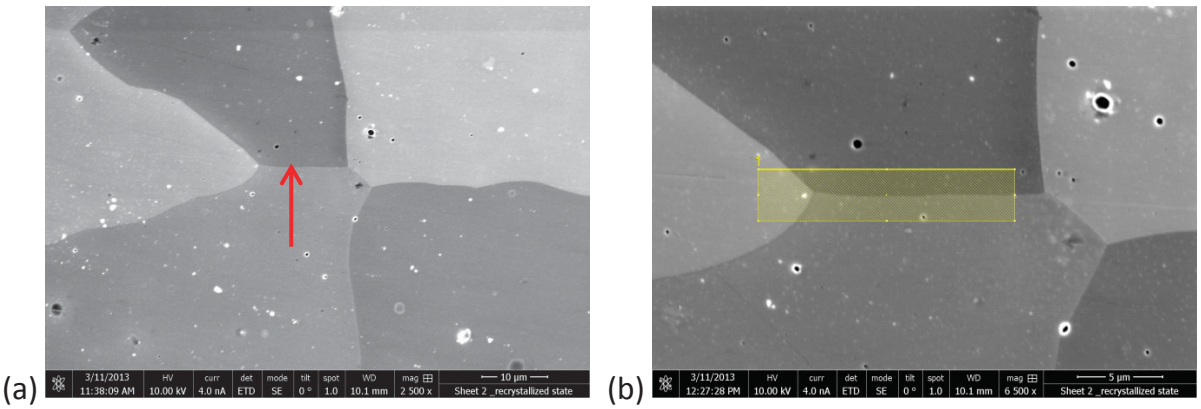

Figure 3.4: Microstructure of sheet 2, recrystallized state. (a) The grain boundary used for FIB preparation is marked with an arrow. (b) The yellow pattern (15 x 3 µm²) for the platinum deposition is shown.

Firstly, a platinum layer with the electron beam was deposited onto the surface at a tilt of 0° (electron beam perpendicular to the specimen surface). The voltage was set to 2kV. Secondly, after tilting the sample to 52° (ion beam perpendicular to the specimen surface) a second layer was deposited by the ion beam with 30kV. Figure 3.5 shows the layer after (a) electron and (b) ion beam deposition.

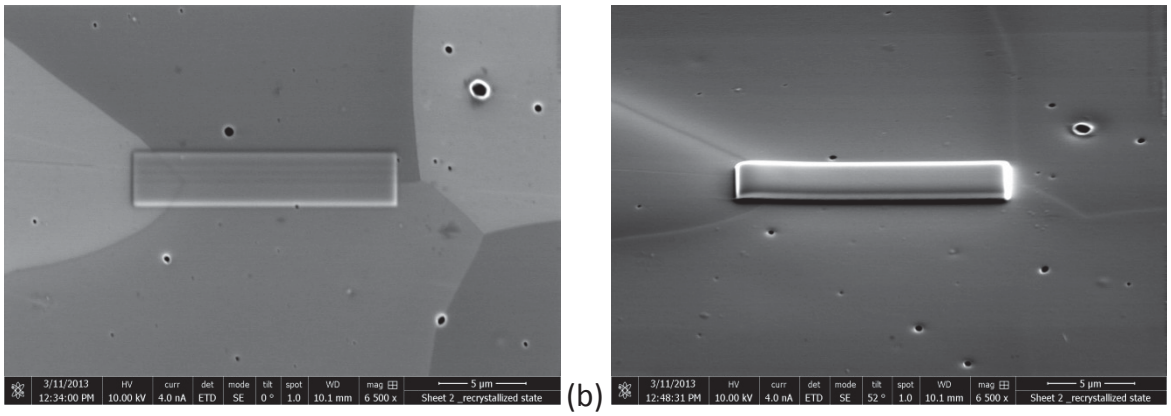

Figure 3.5: Microstructure of sheet 2, recrystallized state with a platinum layer after (a) electron beam and (b) ion beam deposition.

Subsequently, the specimen was tilted to 27° in order to mill deep sloped trenches alongside the platinum layer. Figure 3.6 shows a schematic cross-section of a wedge after milling the trenches. The ion beam is in an angle of 52° to the electron beam where by a tilt of 27° of the specimen caused an incident angle of 25° for the ion beam. In the ideal case, the apex angle of the wedge was 50° and the depth ~7 µm. Furthermore, a grain boundary should be in the cut out volume. The procedure is shown in Figure 3.7 (a-i). The selection of the milling parameters was carried out with consideration of the re-deposition and the milling time. The current was set to 7 nA for a milling pattern of 25 x 4 µm² and a milling depth of 8 µm. In Figure 3.8, a wedge after milling the trenches is visible. The platinum cap, the grain boundary and the area of re-deposition are marked in the figure.

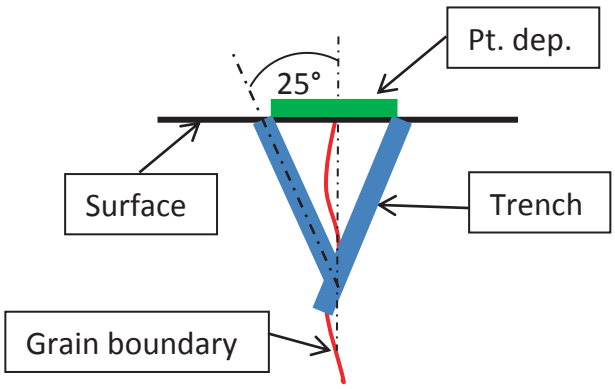

Figure 3.6: Schematic cross-section of wedge after platinum deposition and milling of the trenches.

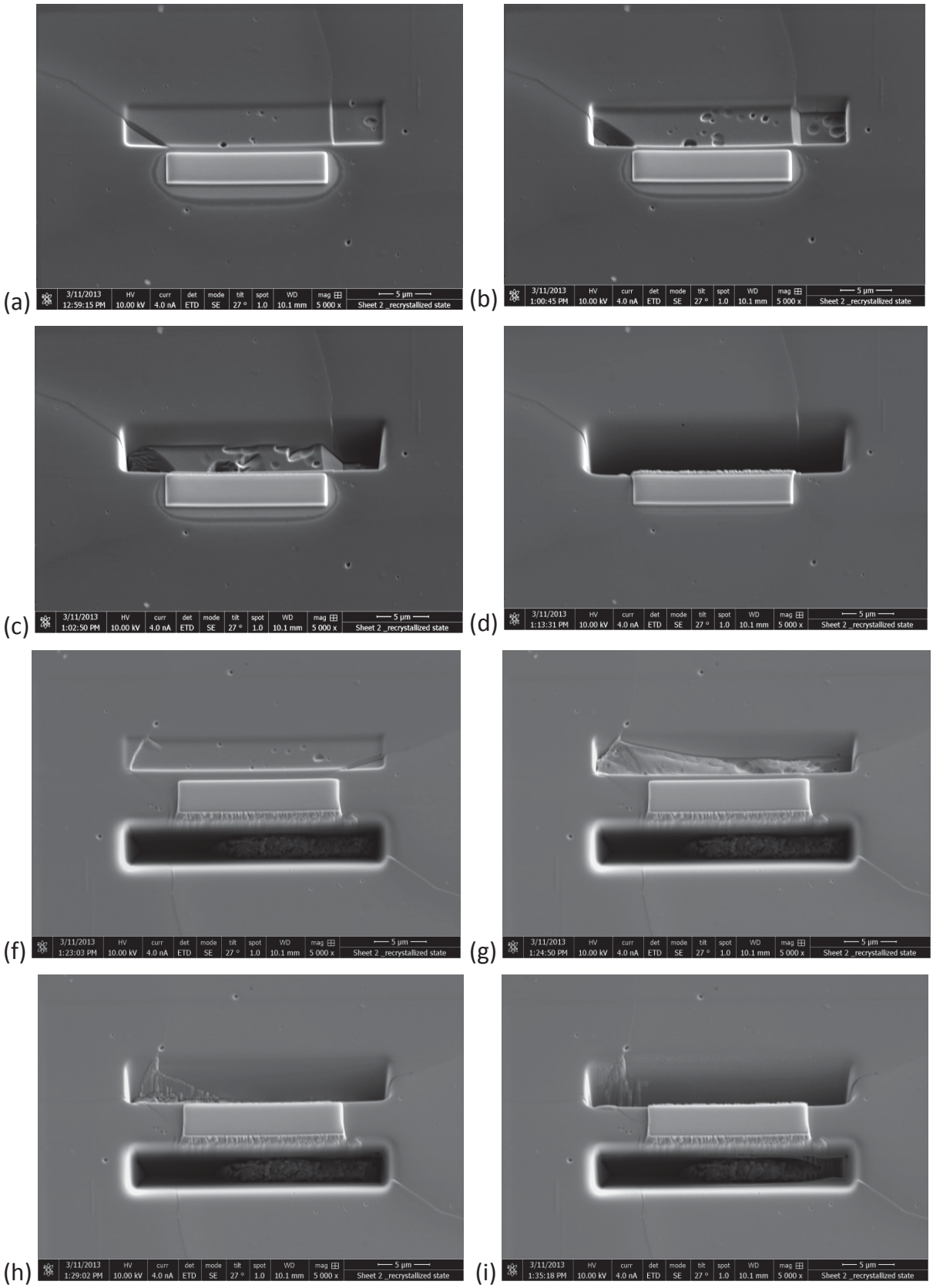

Figure 3.7: SEM images of the milling procedure of a wedge. The trenches were milled alongside of the platinum layer. The specimen was tilted to 27°. The current was set to 7 nA for a milling pattern of 25 x 4 µm² and a milling depth of 8 µm. After step (d) the specimen was rotated 180° for further milling.

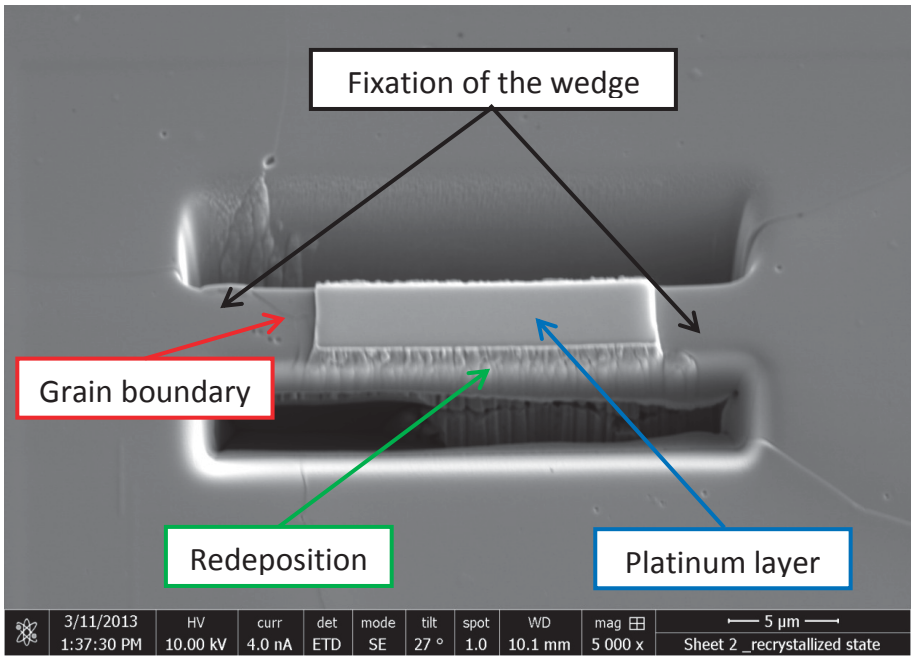

Figure 3.8: SEM image of the wedge after milling the trenches. The lift-out is still connected on the right and left side to the bulk material. The platinum cap and the grain boundary are marked with arrows. Re-deposition appears at the lateral surfaces of the wedge.

Furthermore, a deep sloped trench was milled on the left side of the protective cap as shown in Figure 3.9 (a-d) and Figure 3.10. After the milling procedure, the micromanipulator equipped with a sharp tungsten needle was inserted into the vacuum chamber as well as the platinum gas injection system. The micromanipulator was transferred towards the wedge and positioned at the surface of the platinum layer. The tungsten needle was attached to the wedge by a platinum weld. The procedure is visible in Figure 3.11 (a-d). After the welding process, a line cut was made on the right side of the wedge. Here, the last fixation between wedge and bulk material was removed and the specimen was lifted out with the micromanipulator (see Figure 3.12).

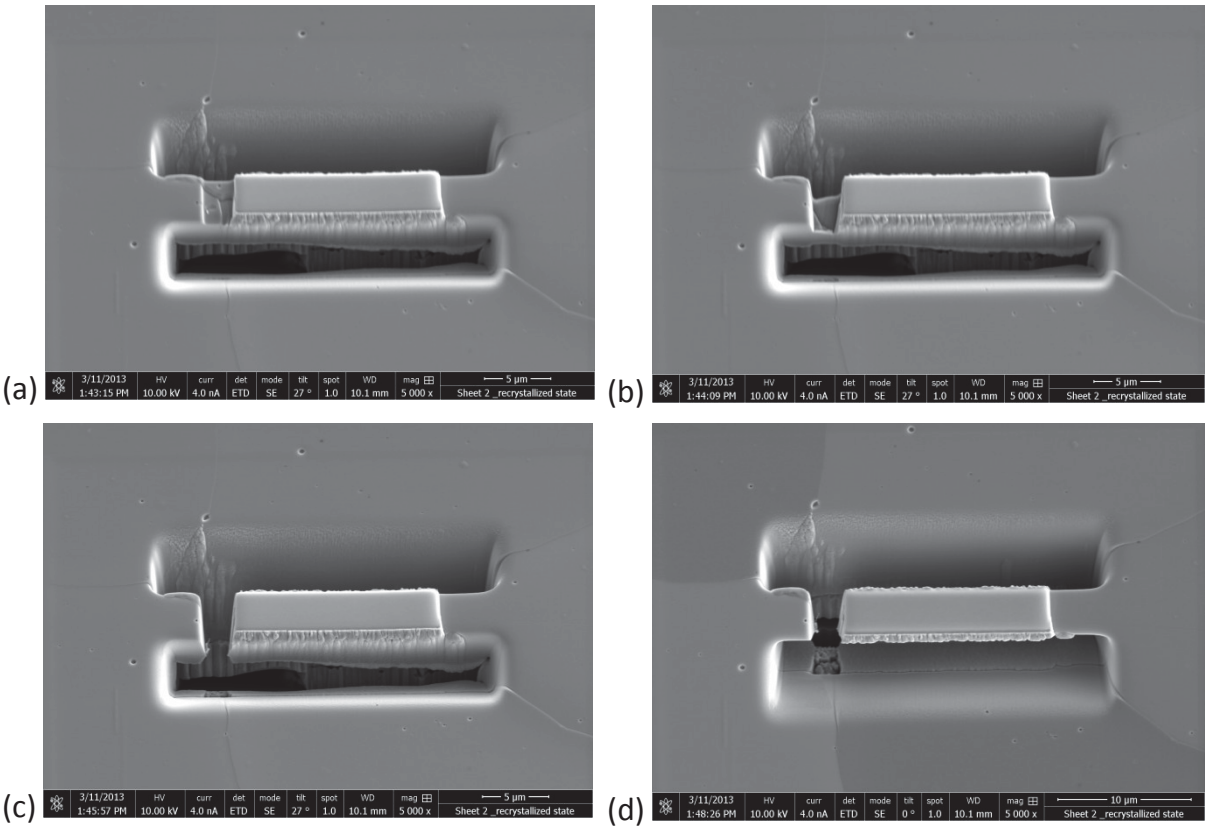

Figure 3.9: SEM images of the milling procedure. A trench is milled on the left hand side of the platinum cap.

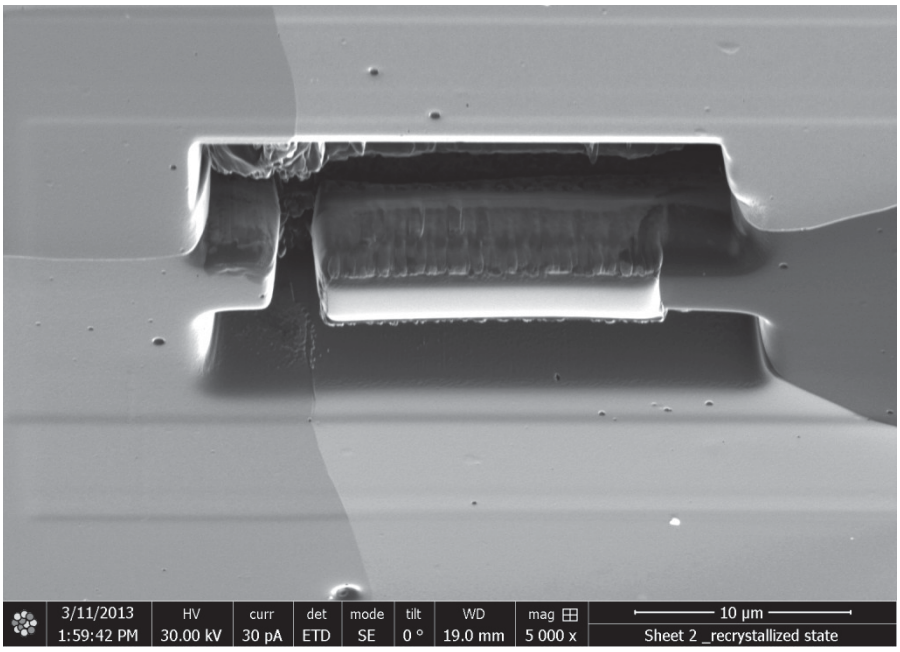

Figure 3.10: FIB image after milling the deep trenches. The wedge is now only attached to the bulk material on the right hand side.

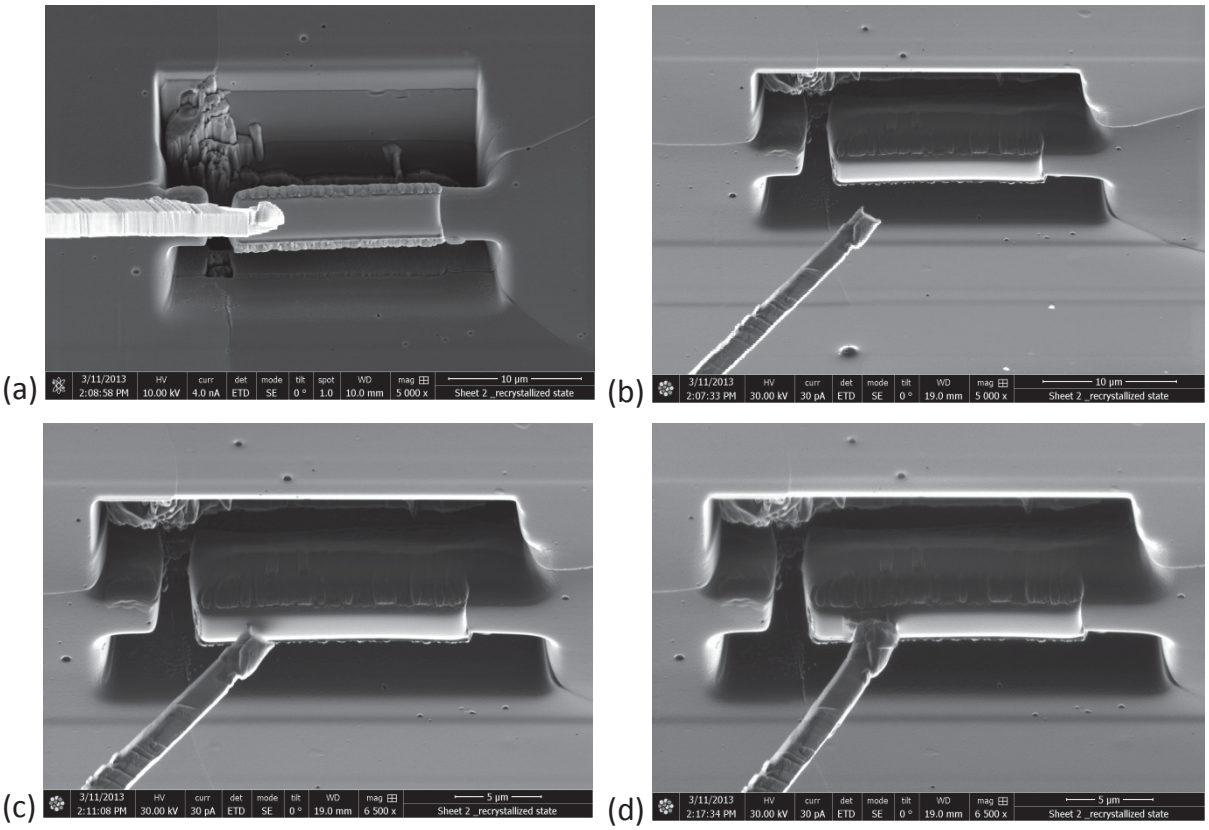

Figure 3.11: FIB images of the welding process. The tungsten needle of the micromanipulator is welded to the wedge with platinum deposition.

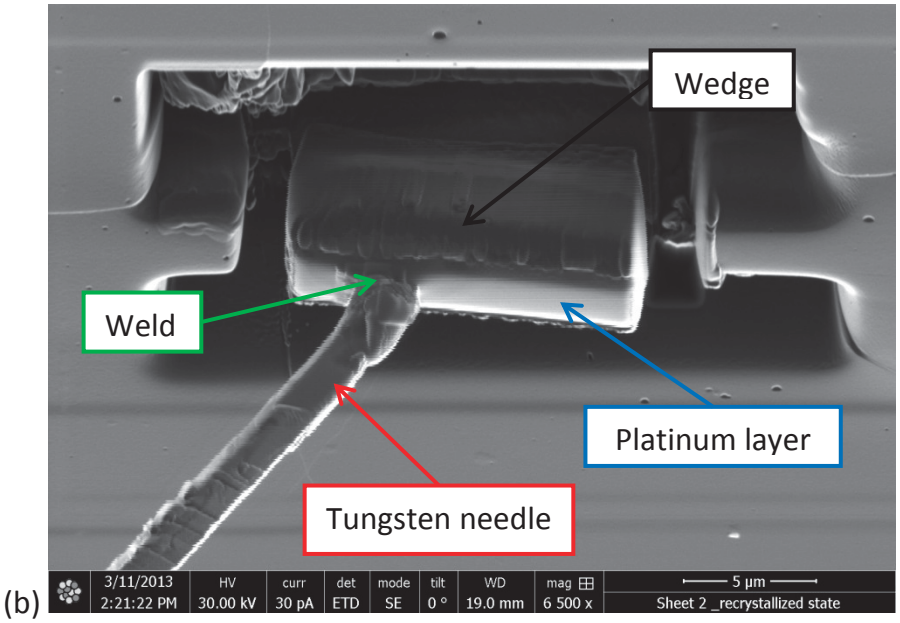

Figure 3.12: FIB images of the lift-out process of the wedge with the micromanipulator. The wedge, the tungsten needle, the platinum layer and the weld are marked with arrows.

As shown in Figure 3.13 (a-b), an electro-polished molybdenum tip can be used as a post. Its final shape was achieved by FIB preparation. As visible in Figure 3.14 and Figure 3.15, the micromanipulator was used to transfer the lifted out wedge to the top of the electro-polished tip. The wedge and the tip were fixed together with a platinum weld. Furthermore, a line cut was used to separate the rest of the wedge from the tip (see Figure 3.16). To create a perfect bond, the lift-out part was welded to the electro-polished tip on both sides (see Figure 3.16). The final lift-out tip before the annular milling procedure is shown in Figure 3.17.

(a) 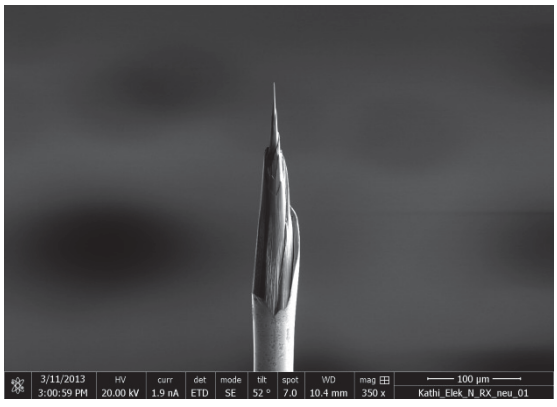

(b) 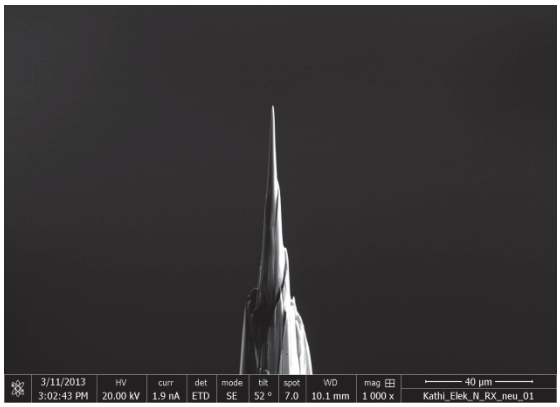

Figure 3.13: SEM image of an electro-polished tip. The appropriate shape was achieved by FIB preparation. This tip was then used as a post. (a) and (b) show different magnifications of the tip.

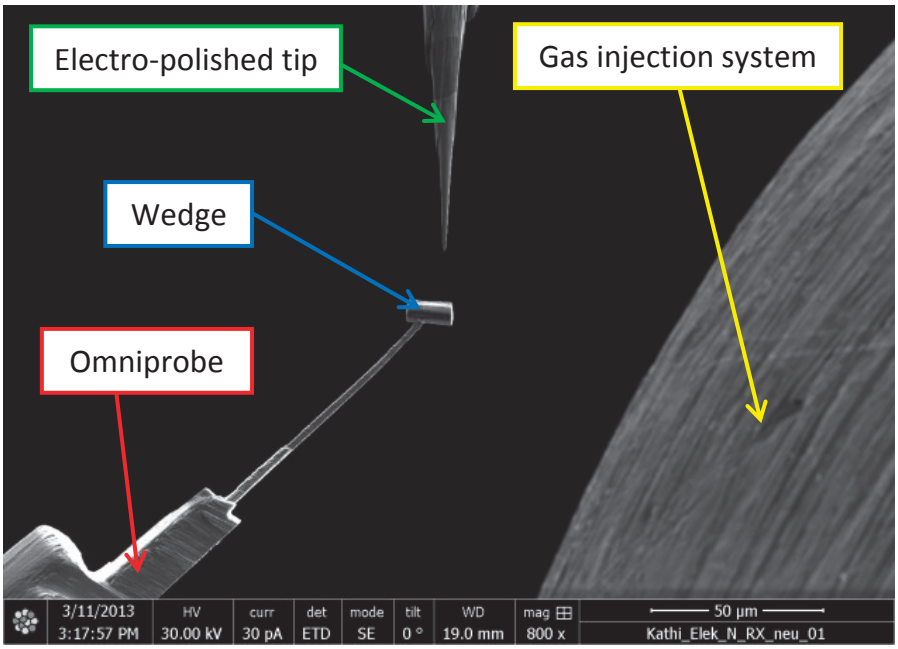

Figure 3.14: SEM images of the transferring procedure of the micromanipulator to the post. Electro-polished tip, Omniprobe (micromanipulator), wedge and platinum gas injection system are marked in the image.

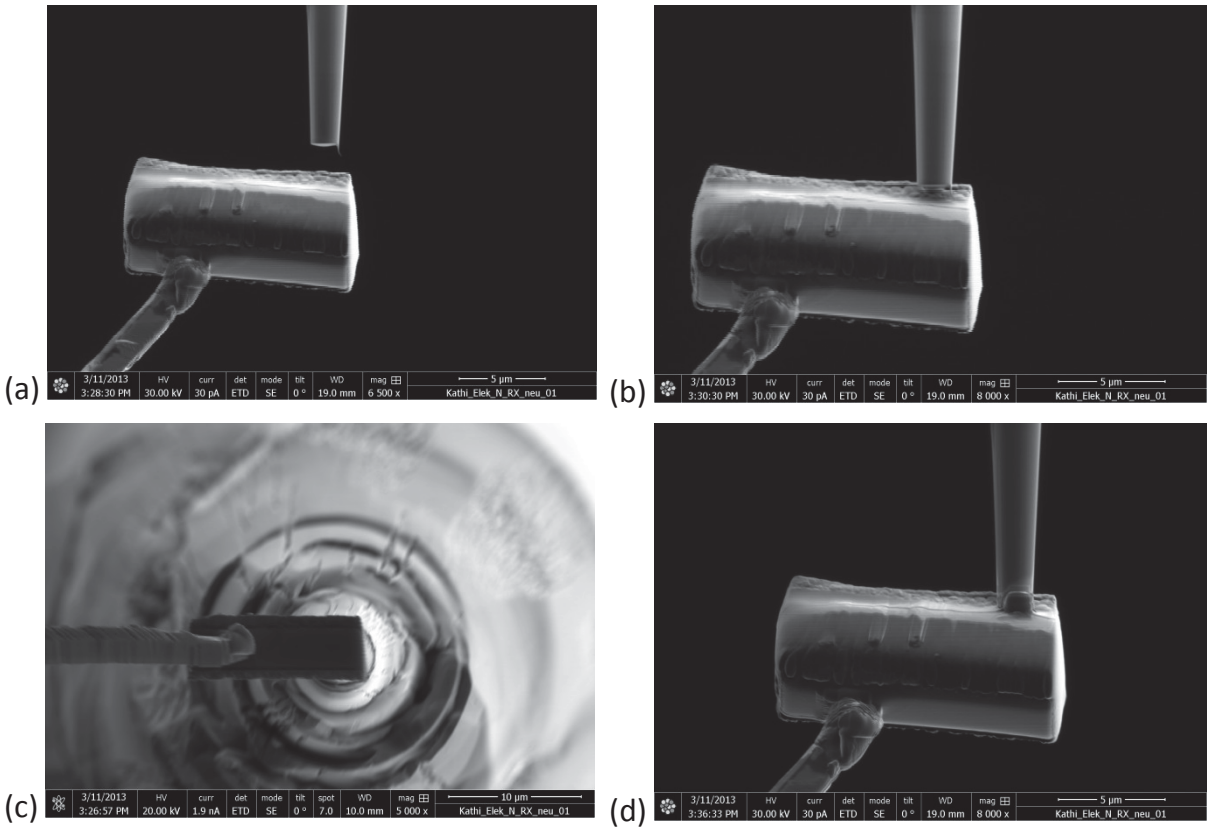

Figure 3.15: SEM images of the transfer procedure of the micromanipulator to the post. The lift-out is positioned on the top of the electro-polished tip (a-c) and fixed with a platinum weld (d).

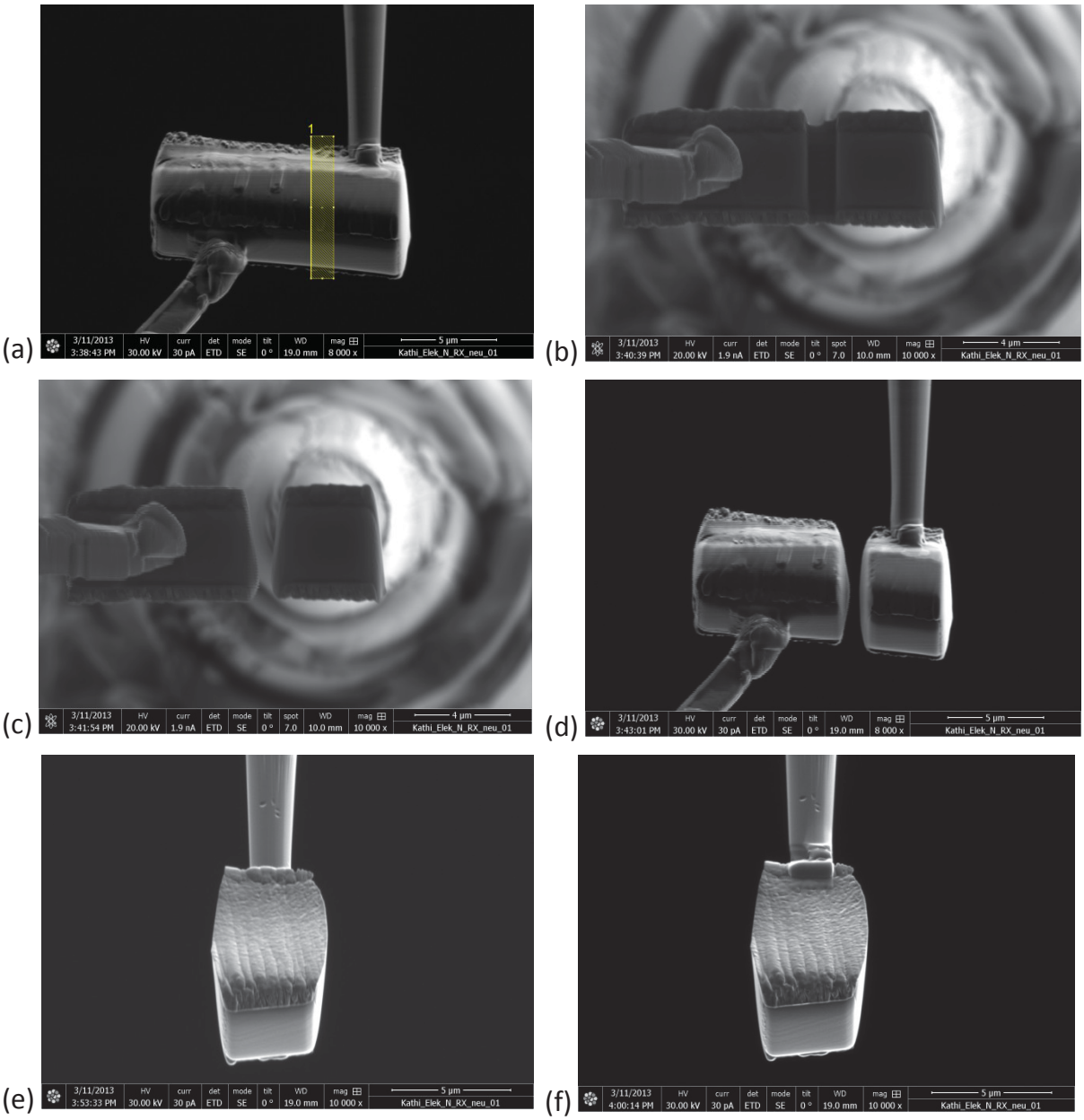

Figure 3.16: SEM images of the milling (a-c) and subsequent welding process (d-f). The lift-out tip was separated by a line cut from the rest of the wedge. After the milling procedure, the tip was rotated for 180° to deposit a platinum weld on the other side for a perfect bond between lift-out and electro-polished tip.

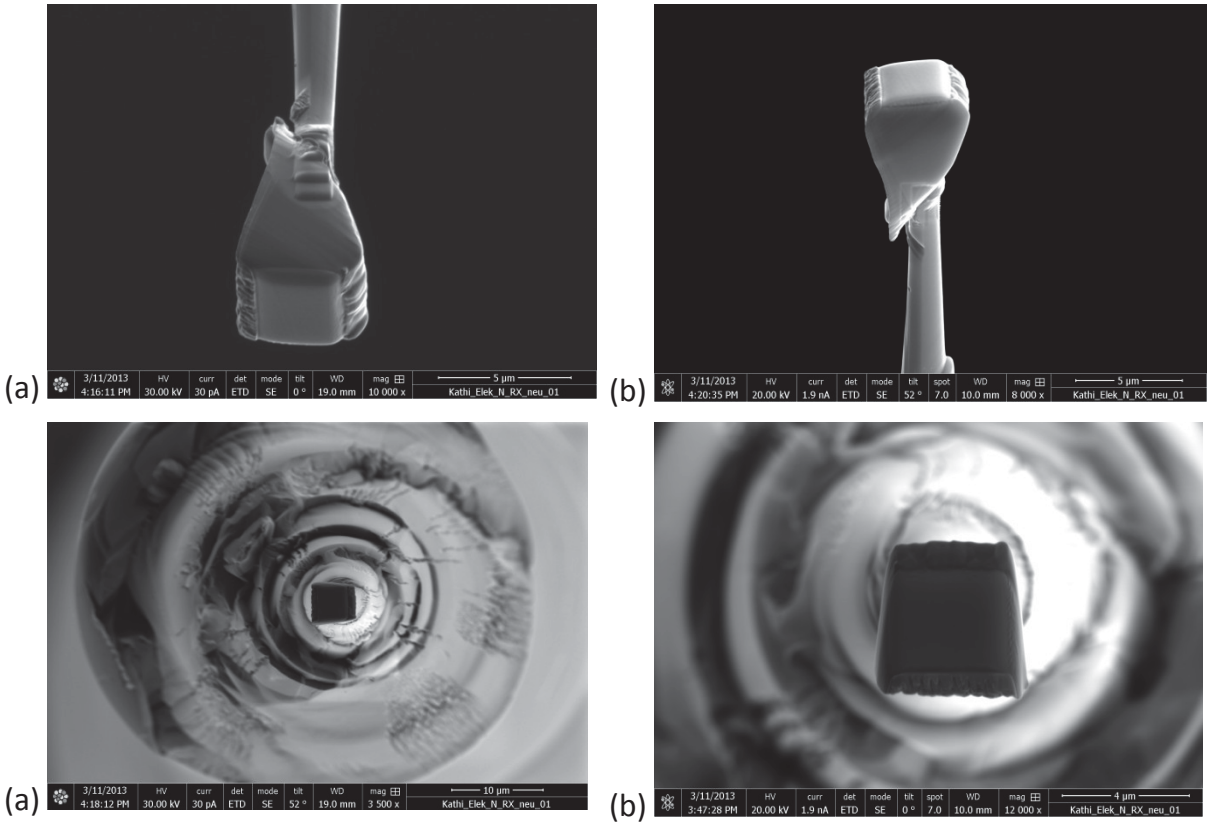

Figure 3.17: SEM images of the lift-out tip after the milling and welding process. Subsequently, the annular milling procedure follows.

Subsequently, annular milling was performed to give the tips the requested radius (~50 nm) and taper angle (< 10°) [51]. During annular milling, the selection of the annular mask and ion current play a significant role for the resulting shape of the tip. In actual research, parameters were specified (see Figure 3.18) by M. K. Miller and K.F. Russell [51]. The same parameters were used in this study.

Therefore, the mask and the current were decreased during the annular milling procedure as shown in Table 3.3 [51].

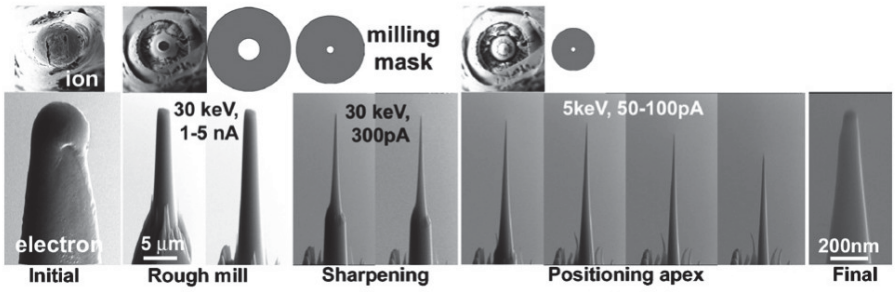

Figure 3.18: Annular milling procedure used by M. K. Miller and K.F. Russell [51]. The size of the annular mask and the ion current were gradually decreased.

The procedure was performed on a molybdenum tip welted towards a post. The inner diameter of the mask was decreased continually while the outer diameter stayed almost constant to avoid protrusions on the shank of the tip [71]. Besides, the outer diameter was set a little bit larger than the cross section of the tip (in this case first ~6 µm and then 2.5 µm) [54]. In Figure 3.19 a tip is shown after the first annular milling steps. The platinum layer, a grain boundary, the platinum weld and the silicon post are marked with arrows. The last preparation steps (cleaning) were carried out with an acceleration voltage of 5 and 2 kV in order to keep the gallium implantation low (see Table 3.3). Due to the beam spread, the end radius of the tips were smaller than the last inner diameter of the annular milling mask [54,71].

Table 3.3: Overview of the annular milling procedure of a molybdenum tip welded to a post. The outer diameter was set a little bit larger than the cross-section of the tip and kept constant. The inner diameter of the mask as well as the milling current was decreased gradually. The last two preparation steps were performed at an acceleration voltage of 5 and 2 kV to keep the gallium implantation low.

Parameter	**Annular Milling Steps**				
	Step 1	Step 2	Step 3	Step 4	Step 5
d_{outer} [µm]	~ 6	2- 2.5	2-2.5	1	1
d_{inner} [nm]	2000	700	500	500	0
HV [kV]	30	30	30	5	2
I [nA]	2.7	0.84	0.42	0.045	0.028

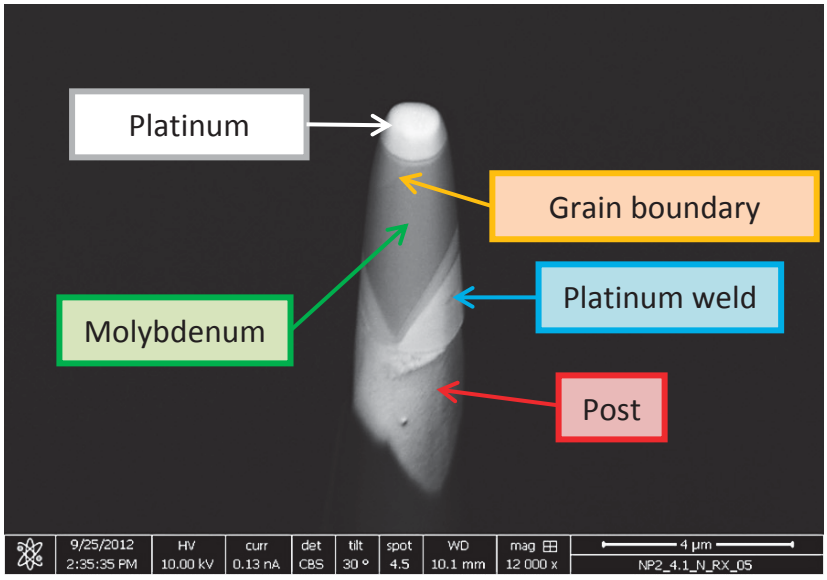

Figure 3.19: FIB- prepared molybdenum tip with a single grain boundary after the first annular milling steps. The platinum layer, the grain boundary, the platinum weld, and the post are marked with arrows.

A finished tip welded to a silicon post is shown in Figure 3.20. The protrusions were 18 µm away from the top of the tip and consequently do not influence the subsequent APT measurement [39].

The annular milling process gave the tips the proper shape. As shown in Figure 3.21 the tips had a radius of ~40 nm and a taper angle of less than 10°.

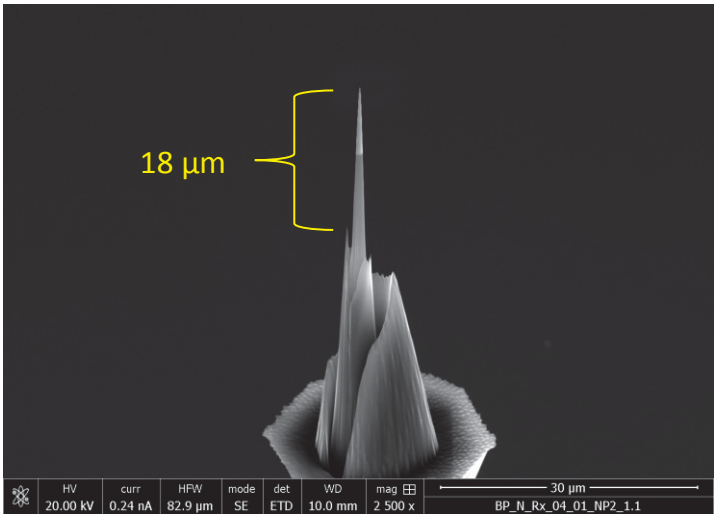

Figure 3.20: SEM image of a final tip welded to a silicon post. The specimen was taken out of sheet 1 (recrystallized state). Due to the distance of 18 µm to the top of the tip the protrusions do not influence the APT measurement [39].

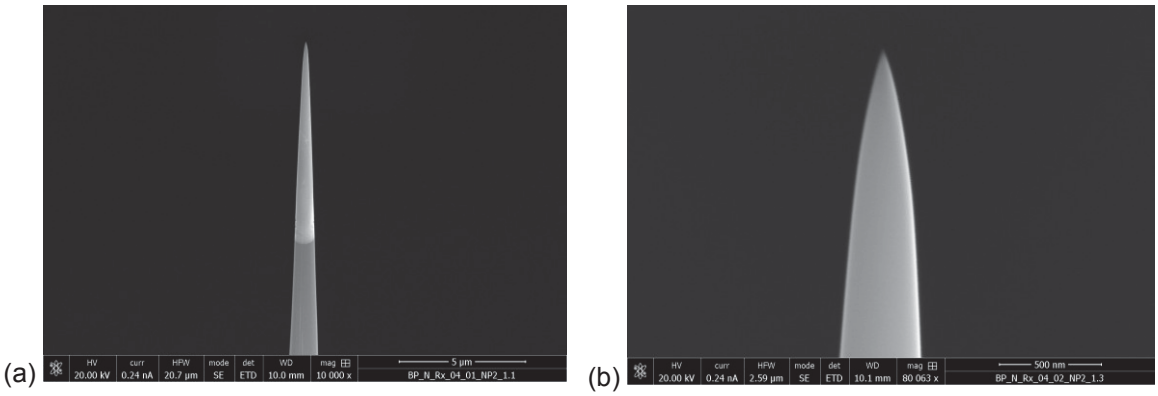

Figure 3.21: SEM images of a finished tip welded to a silicon post with two different magnifications in (a) and (b). The specimen was taken out of sheet 1 (recrystallized state). The radius of the tip was ~40 nm and the taper angle < 10°.

Applying this preparation method, problems occurred during the procedure. The grain boundaries were visible on the surface of the samples but their progression under the surface was not known as shown in Figure 3.3. It was never clear if the wedge included a grain boundary or not. Furthermore, at radii lower than~500 nm the visibility of the grain boundary was poor and led to a kind of “blind preparation”. Therefore, a second method was applied.

3.2.2 Electrolytic polishing method with subsequent FIB sharpening

The pre-electro-polished tips were prepared out of the as-deformed state and recrystallized state of sheet 1 and 2. As shown in Figure 3.22 the extraction of the needles was carried out perpendicular to the rolling direction. The green lines mark the extraction points of the atom probe needles for the electro-polishing process.

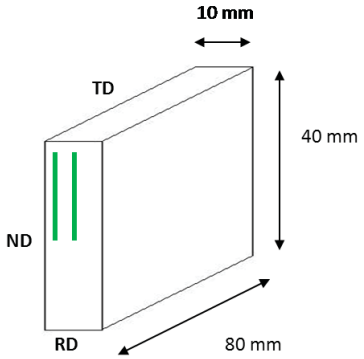

Figure 3.22: Illustration of the sample material of the molybdenum sheet. The green lines mark the extraction points of the atom probe needles for the electro-polishing process. RD stands for rolling direction, ND indicates the normal direction and TD stands for transverse direction.

After cutting the needles out of the bulk material, electro-polishing was performed [41,44,47–50]. The needles, with a length of ~12 mm and a cross-section of ~ 300 x 300 µm² were fixed in a copper holder for the further atom probe analyses. Subsequently, a two-stage electro-polishing process followed [50]. Firstly, a 5-7 mm thick layer of electrolyte was put onto a denser electrically and chemically inert liquid. The electrolyte for the molybdenum needles was 12,5% H_2SO_4 with ethanol [72] used at RT. Secondly, a tapering necked region was formed by moving the needle up and down with a voltage of ~15 V. Due to slow movements, the attack at the air-electrolyte interface was prevented and the dissolution occurred only at the electrolyte- inert liquid interface. The result was a needle-shaped specimen with a reduced cross-section in the middle. The second step preformed in the same electrolyte with lower voltage values (7-8 V) led to an additional removement of material in the reduced cross-section area of the specimen. Finally, the lower part broke off. The last step, the micropolishing, sharpened the tip to give it the right shape. As shown Figure 3.23, the needle was moved back and forth through a drop of electrolyte in a wire loop at a low voltage (~2-5 V). The entire polishing process was monitored with an optical microscope.

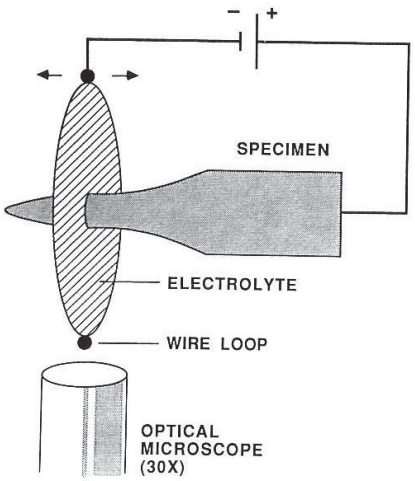

Figure 3.23: Image of the micropolishing process, the last step of the electrolytic polishing procedure. The needle is moved back and forth through a drop of electrolyte in a wire loop at a voltage of ~5 V to sharpen the tip [50].

The finished pre-electro-polished tips were transferred to the FIB for further sharpening. The annular milling procedure gave the tips the right radius and taper angle (see chapter 3.2.1, Figure 3.18). Furthermore, a grain boundary should be positioned close to the apex by milling. A pre-electro-polished tip contains many grain boundaries. By ion beam milling, one of these boundaries should be positioned in the first 100 nm of the tip. As shown in Figure 3.24, the grain boundary is clearly visible in the electro-polished tip after the first milling steps.

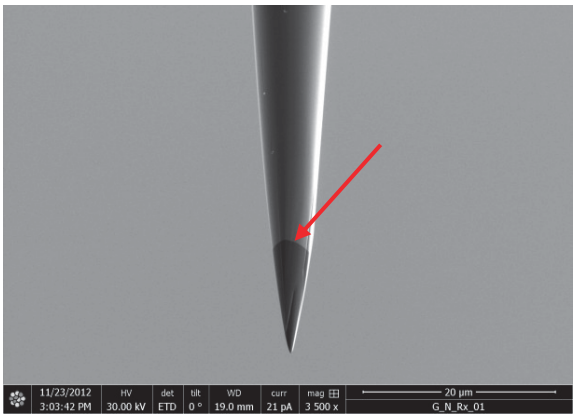

Figure 3.24: FIB image of a sharpened electro-polished tip with a grain boundary at ~10 µm below the top of the tip. The arrow marks the grain boundary.

However, for radii lower than ~500 nm it was always difficult to deduce if the grain boundary was in the volume examined or not. The poor visibility of the grain boundary during annular milling in the last preparations steps led to “blind preparation” during this preparation procedure. For the lift-out-technique as well as for the pre-electro-polished

tips the visibility of the grain boundaries at radii lower than 500 nm was poor. This led to the conclusion that only TEM examination could improve the preparation process. Therefore, a third method was applied.

3.2.3 Electrolytic polishing method with a FIB/TEM combination

Electro-polished tips were produced [41,44,47–50] and sharpened with the FIB as described before. Furthermore, TEM analyses were performed to get information about the exact location of the grain boundary at small radii. The recrystallized state and as-deformed state of sheet 1 and 2 were used for specimen preparation. The FIB work was carried out with a FEI Strata DB 235 DualBeam FIB at an acceleration voltage of 30 kV. The TEM analyses were performed with a FEI Tecnai G2 TEM equipped with a LaB6 filament at 200 kV. The pre-electro-polished tips were characterized with the TEM in-between the milling steps to obtain information about the distance of the grain boundaries to the top of the tip. After sharpening in the FIB, the tips were analyzed in the TEM and re-examined in the FIB again to bring the grain boundary into the first 100 nm. The Figure 3.25 shows a TEM image of a pre-electro-polished and FIB sharpened tip with a grain boundary. Due to the TEM investigations, it is obvious that the boundary is ~120 nm away from the top of the tip. A last annular milling step would be necessary to bring the interface into the first 100 nm for a good APT measurement.
A continuous change from FIB to TEM was necessary for this technique. Furthermore, as shown in Figure 3.26 the exact shape of the tip was investigated. Small protrusions which were not visible in the FIB/SEM could be analyzed with the TEM. These shape defects influenced the APT measurements intensively and caused many faulty runs.

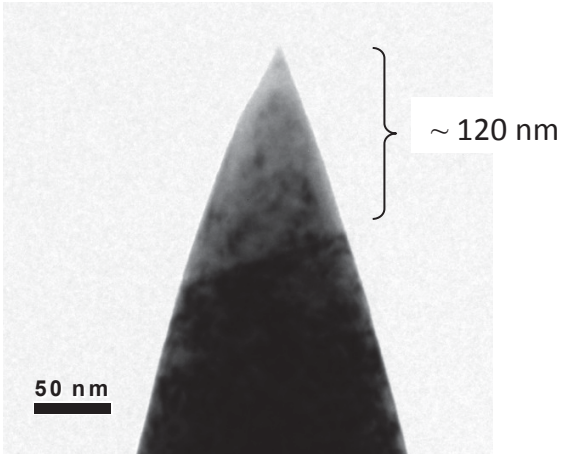

Figure 3.25: TEM image of a pre-electro-polished and FIB sharpened tip with a grain boundary at ~120 nm. It is obvious that a last annular milling step is necessary to bring the interface into the first 100 nm of the tip.

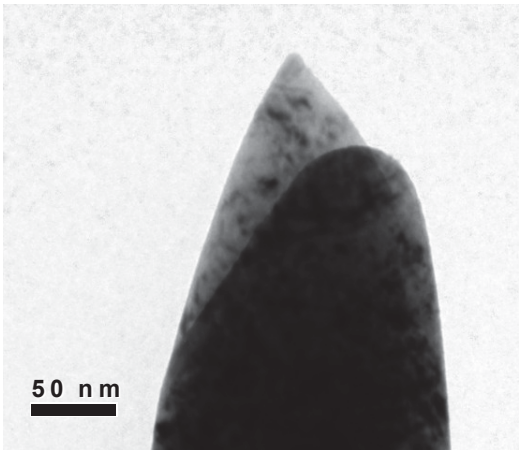

Figure 3.26: TEM image of a pre-electro-polished and FIB sharpened tip with a protrusion after ~50 nm. These defects influence the APT measurements intensively and caused many faulty runs.

The TEM investigations gave clear information about the location of the grain boundary. No visibility problems occurred. These investigations in-between the milling steps were a perfect option to bring the grain boundaries into the first 100 nm. Additionally, a clear image of the shape of each tip was available for later comparison with the reconstructions of the APT measurements.

3.3 APT measurements

The ATP tips were measured with a LEAP 3000X HR from Cameca. Voltage as well as laser mode runs were performed. For the analyses the lift-out tips with silicon and electro-polished posts as well as the pre-electro-polished and FIB sharpened tips were used.
The parameters for the measurements of the lift-out tips welded onto a silicon post and an electro-polished molybdenum tip are listed in the Table 3.4 and Table 3.5. The pulse rate for laser mode was 250 kHz and for voltage mode 200 kHz. The target evaporation rate was set to 1%.

Table 3.4: Parameters for the APT measurements of the lift-out tips with silicon post. The pulse rate for laser mode was 250 kHz and for voltage mode 200 kHz. The target evaporation rate was set to 1%.

		APT measurement			
Number	Specimen	Modus	T [K]	Laser energy [nJ]	Pulse fraction [%]
1	Sheet 2	Voltage	60	-	15
2	Sheet 1	Laser	60	0.6	

Table 3.5: Parameters for the APT measurements of the lift-out tips with electro-polished post. The pulse rate for laser mode was 250 kHz and the target evaporation rate was set to 1%. In this case only laser mode was used**.**

APT measurement				
Number	Specimen	Modus	Laser energy [nJ]	T [K]
1	Sheet 2	Laser	0.6	60
2	Sheet 2	Laser	0.6	80

The electro-polished and FIB sharpened tips were measured in laser and voltage mode. The as-deformed and the recrystallized state was used for the tip preparation. The pulse rate for laser mode was 250 kHz and for voltage mode 200 kHz. The target evaporation rate was set to 1%. The temperature was 60 K. Table 3.6 summarizes the parameters for these measurements.

Table 3.6: Parameters for the APT measurements of the pre-electro-polished and FIB sharpenend tips. The pulse rate for laser mode was 250 kHz and for voltage mode 200 kHz. The target evaporation rate was set to 1%. The temperature was 60 K.

APT measurement				
Number	Specimen	Modus	Laser energy [nJ]	Pulse fraction [%]
1	Sheet 2, as-deformed	Laser	0.6	-
2	Sheet 2, recrystallized	Voltage	-	15
3	Sheet 1, as-deformed	Voltage	-	15

The tips produced out of the FIB/TEM combination were measured in laser mode with a laser energy of 0,6 nJ, a temperature of 60 K and a pulse rate of 200 kHz. The target evaporation rate was set to 0.5%. For the reconstruction of the analyses the IVAS 3.6.0 data software from Cameca was used.

3.4 AES measurements

As a complimentary method, AES was performed. Both sheet 1 and 2 were analyzed in the recrystallized state. In Figure 3.27 the specimen geometry for the AES measurement is shown.

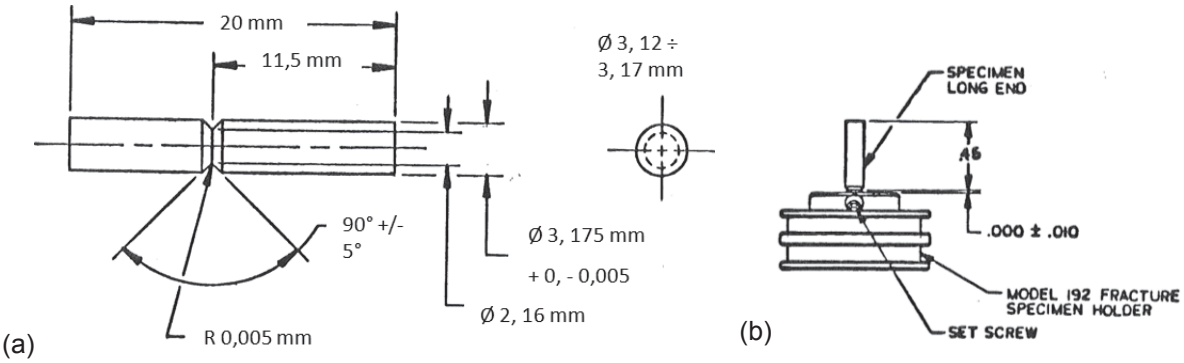

Figure 3.27: (a) Image of the specimen geometry for the AES measurements; (b) image of specimen holder with attached specimen [73].

A PHI 680 Auger Nanoprobe with a Schottky field emission electron gun was used at a pressure between $1x10^{-9}$ mbar and $1x10^{-10}$ mbar. The two sheets were analyzed after breaking them in-situ in the vacuum chamber. Due to fast deposition of oxygen on the surface, the measurement of oxygen was conducted within 5 min after breaking the samples. Inter- and transgranular fracture surfaces and micropores were characterized as shown in Figure 3.28. Element mappings as well as point analyses were performed to compare the difference between grain boundary and bulk material.

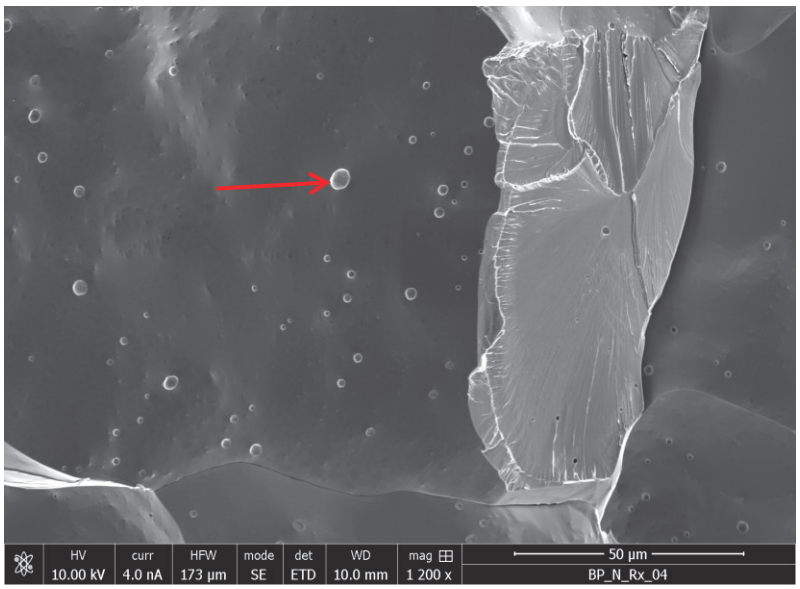

Figure 3.28: Fracture surface of sheet 1 (recrystallized state) with trans- and intergranular fracture. One micropore is marked with an arrow.

4 Results

According to the chemical analyses (see Table 3.1), sheet 1 and 2 contained impurity elements in the parts per million range. Especially the higher potassium content of sheet 2 was remarkable. For example, due to the low solubility of oxygen in molybdenum it should accumulate at interfaces like grain boundaries [69]. To investigate these grain boundary segregations APT and AES as complementary method were performed in this study.

4.1 APT results

4.1.1 Lift-out technique

The lift-out technique as proposed by M.K. Miller [51,54] was applied for the first time to study a grain boundary in the atom probe. In accordance with publications it should be a perfect technique to measure a grain boundary [38,39]. However, in this study many problems occurred:

First of all the progression of the grain boundary under the surface was not known as depicted in Figure 3.3. The course of the boundary did not have to be straight downwards as shown in Figure 3.6. It could be possible that the grain boundary ran out the wedge just below the surface. Furthermore, the grain boundary was not visible anymore at lower radii than ~500 nm during the annular milling process which caused "blind preparation". Although the annular milling produced perfectly shaped tips as shown in Figure 3.21, it was never clear if a grain boundary was in the examined volume or not. In addition, the selection of the post material played a significant role for the further APT analyses.

The wedges were welded onto silicon needle pads and on electro-polished molybdenum tips.

In case of the silicon posts problems with the heat discharge during the APT measurements occurred. The heat conductivity of molybdenum and silicon is different (see Table 4.1) which caused heat accumulation during the APT measurement [1].

Table 4.1: Heat conductivity of molybdenum and silicon at room temperature [1].

Heat conductivity	
Molybdenum [W/mK]	Silicon [W/mK]
140	83,7

This heat barrier led to melting of the tips in laser mode as visible in Figure 4.1 (a) and in voltage mode as shown in Figure 4.2 (a-b). Furthermore, the tips flashed due to the additional stresses during the measurements (see Figure 4.1 (b)). Thus, the appearing stress and the heat accumulation led to unsuccessful APT analyses (See Table 4.2).

(a) 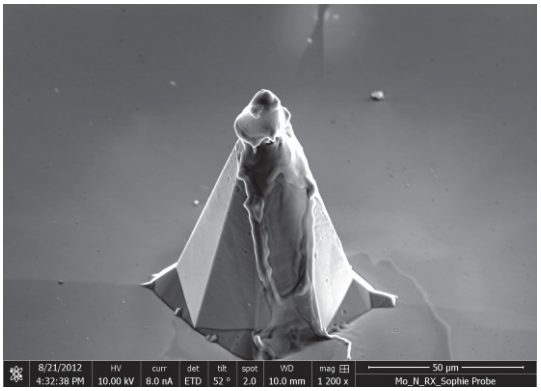 (b) 

Figure 4.1: Tips after the APT measurement analyzed in laser mode. (a) Due to the heat barrier between molybdenum and silicon the tip melted. (b) Some tips flashed due to additional stresses.

(a) 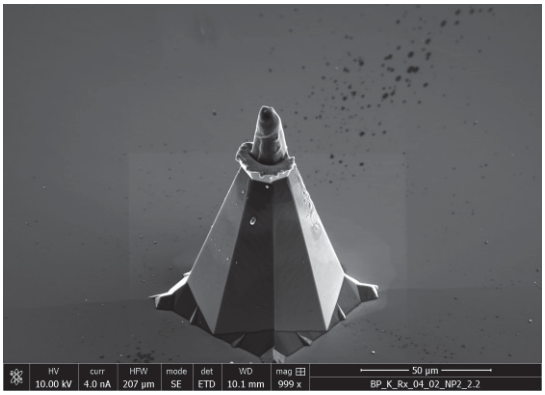 (b) 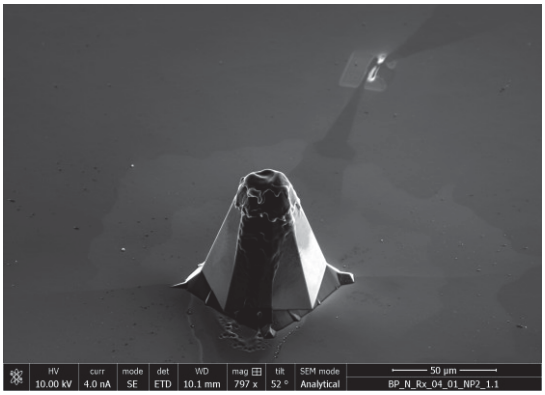

Figure 4.2: Tips after the APT measurement analyzed in voltage mode. Due to the heat barrier between molybdenum and silicon the tip melted.

Table 4.2 summarizes the APT measurement results of tips welded onto a silicon post. The APT parameters are listed in Table 3.4. The number of detected ions was low in all cases.

Table 4.2: Results of the APT measurements. The lift-out technique was used and the tips were welded to a silicon post. The parameters are listed in Table 3.4. The number of detected ions was low due to the applied stress and the heat accumulation during the measurement.

APT measurement				
Number	Specimen	Modus	Failure	Detected ions
1	Sheet 2	Voltage	melted	1.898.890
2	Sheet 1	Laser	flashed	343.701

The number of detected ions was low due to the appearing stress and the heat accumulation during the measurement. No successful analyses were achieved.

Also electro-polished tips of molybdenum were used as a post for the lifted out wedges. The heat conductivity was similar for the post and the tip in this case. Only the platinum layer interrupted the heat flow. In Figure 4.3, two tips are shown after the APT analyses. The platinum weld was a weak point and led to failure. The heat inserted by the laser beam caused melting. The amount of detected ions is higher than for the lift-out tips on silicon posts as visible in Table 4.3. The parameters for these measurements are shown in Table 3.5.

(a) 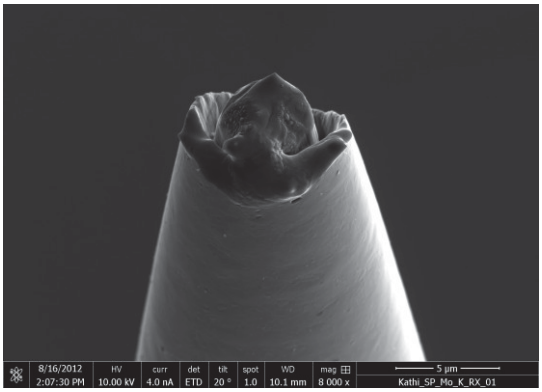

(b) 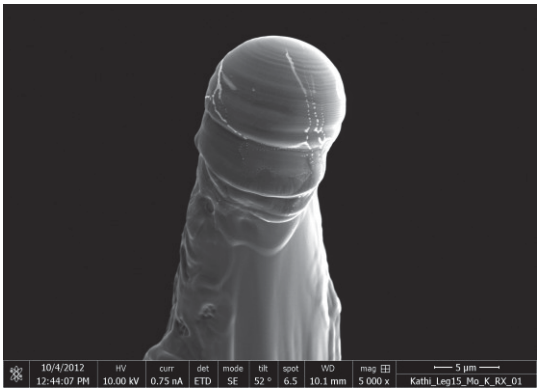

Figure 4.3: Tips after the APT measurement. (a) Voltage mode was used, the tip flashed at the platinum weld. (b) Laser mode was used, the tip melted.

Table 4.3: Results of the APT measurement. The lift-out technique was used and the tips were welded towards an electro-polished, out of a molybdenum alloy. The tips were out of sheet 2 in the recrystallized state. The laser mode was used and all tips failed due to melting.

APT measurement			
Number	T [K]	Modus	Detected ions
1	60	Laser	5.844.169
2	80	Laser	9.511.845

However, again “blind preparation” led to same problem as described before. Also in this case no segregations could be found. In order to avoid further failures during the APT measurements electro-polished tips were sharpened in the FIB.

4.1.2 Electrolytic polishing method with subsequent FIB sharpening

In the case of the second method similar problems appeared as for the lift-out technique. The grain boundary was clearly visible in the tips for radii bigger than ~500 nm, but lower radii led to “blind preparation” as well as for the lift-out technique. Figure 4.4 shows two images of a tip during annular milling. In the first milling steps the grain boundary was visible, but after the last preparation steps the grain boundary was not visible anymore.

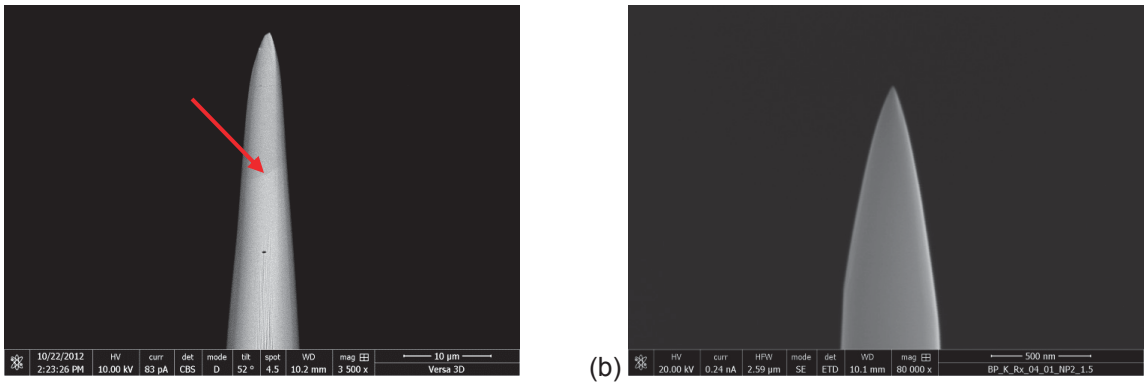

Figure 4.4: (a) SEM image of a FIB- prepared tip of sheet 2 (as-deformed state). The tip has a radius of ~2 µm after the first milling steps, the grain boundary is marked with an arrow. (b) SEM image of a FIB- prepared tip after the final annular milling with a tip radius of ~25 nm and a taper angle of < 10°, however, the grain boundary is not visible anymore.

Table 4.4 summarizes the APT results of pre-electro-polished and FIB sharpened tips. These tips did not contain any weld, therefore, no heat accumulation occurred. The results showed higher numbers of detected ions than for the measured lift-out tips. No weak spots were present in these tips which led to improved APT measurements. However, it was never clear if a grain boundary was in the examined volume or not due to the "blind preparation" during the last annular milling steps.

Table 4.4: Results of the APT measurement of pre-electro-polished and FIB sharpened tips.

APT measurement				
Number	Specimen	Modus	Failure	Detected ions
1	Sheet 2, as-deformed	Laser	melted	20.048.665
2	Sheet 2, recrystallized	Voltage	max. voltage	9.649.782
3	Sheet 1, as-deformed	Voltage	melted	20.868.543

The reconstruction of an analyzed tip from the as-deformed state of sheet 2 (number 1 in Table 4.4) shows just molybdenum and no impurities (see Figure 4.5.). No grain boundary is visible. However, it cannot be deduced without doubt if a grain boundary without segregations was present in the measured volume by APT. The bulk composition as determined by ATP is shown in Table 4.5. Although, tungsten was measured in the chemical analyses (Table 3.1), it was not detected by means of APT. Besides, no other elements except of small amounts of magnesium were found in this specimen.

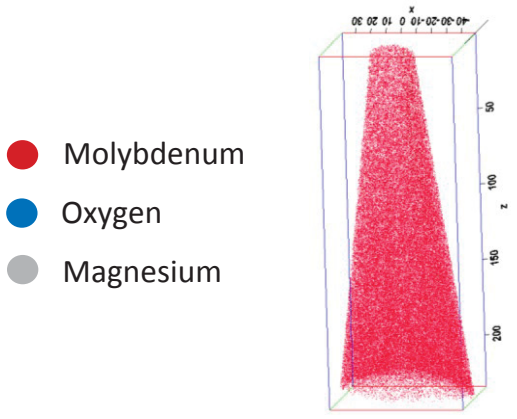

Figure 4.5: APT reconstruction of the tip (see Table 4.4) from Figure 4.4 after the atom probe measurement. It cannot be deduced without doubt if a grain boundary without segregations was present in the measured volume. The inset shows the corresponding color code for the ions/molecules detected. The oxygen and magnesium content is too low for a good visibility in the reconstruction.

Table 4.5: Bulk composition of sample out of sheet 2, as-deformed state, as determined by APT.

Element	Content [at.%]
Mo	99,973
O	0,024%
Mg	0,003%

4.1.3 Electrolytic polishing method with a FIB/TEM combination

Due to the poor visibility of the grain boundary during the last preparation steps with the FIB, TEM investigations were performed in order to determine the exact position of the boundary. These APT measurements were performed in laser mode to keep the applied field in then atom probe lower to reduce fracture failure during analysis.

In Figure 4.6, the TEM bright (a) and dark field (b) images of a tip and the related reconstruction of the APT measurement (c) are shown. In the dark field image (b) only the lower part of the tip is visible. The tip was prepared out of sheet 2 (as-deformed state).

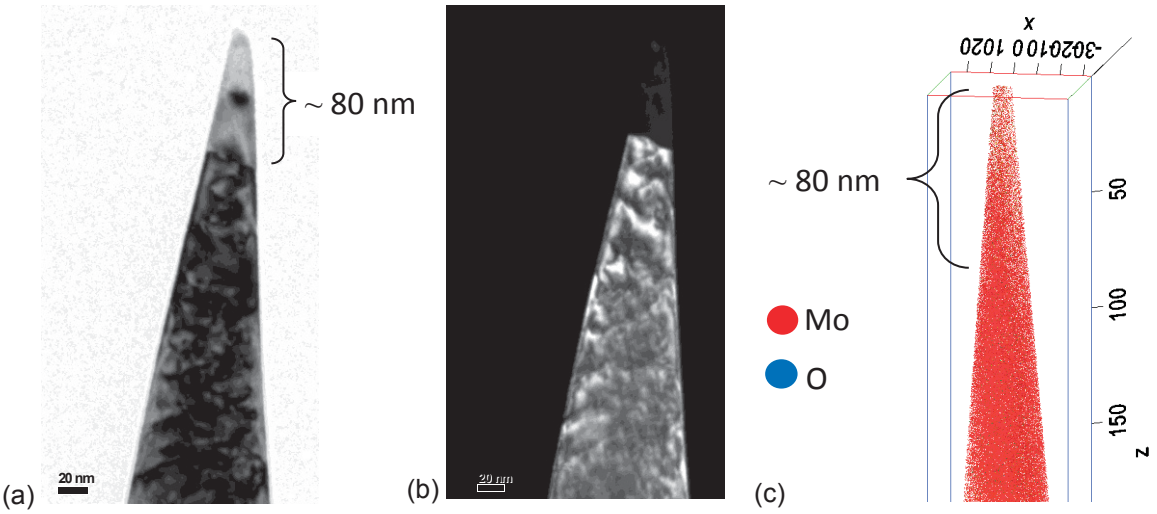

Figure 4.6: TEM image of FIB prepared tip (a) bright field image (b) dark field image (c) APT reconstruction of the tip after the atom probe measurement. The inset in (c) shows the corresponding color code for the ions/molecules detected. The oxygen content is too low for a good visibility in the reconstruction. Gallium is blanked.

A grain boundary is visible within the first 80 nm (according to TEM), but the reconstruction shows no impurities at the grain boundary. Molybdenum, oxygen and gallium atoms are in the tip. The molybdenum and the molybdenum oxygen molecules were preferentially detected on one side of the tip caused by the direction of the laser beam. Again, no segregation of impurities at the grain boundary can be seen (Figure 4.6).

However, grain boundary segregations were found in some other specimens. Figure 4.7 shows a TEM image (a) and the reconstruction (b) of a tip with a “segregated region” and a grain boundary with segregations. The sample is from sheet 1 in the recrystallized state.

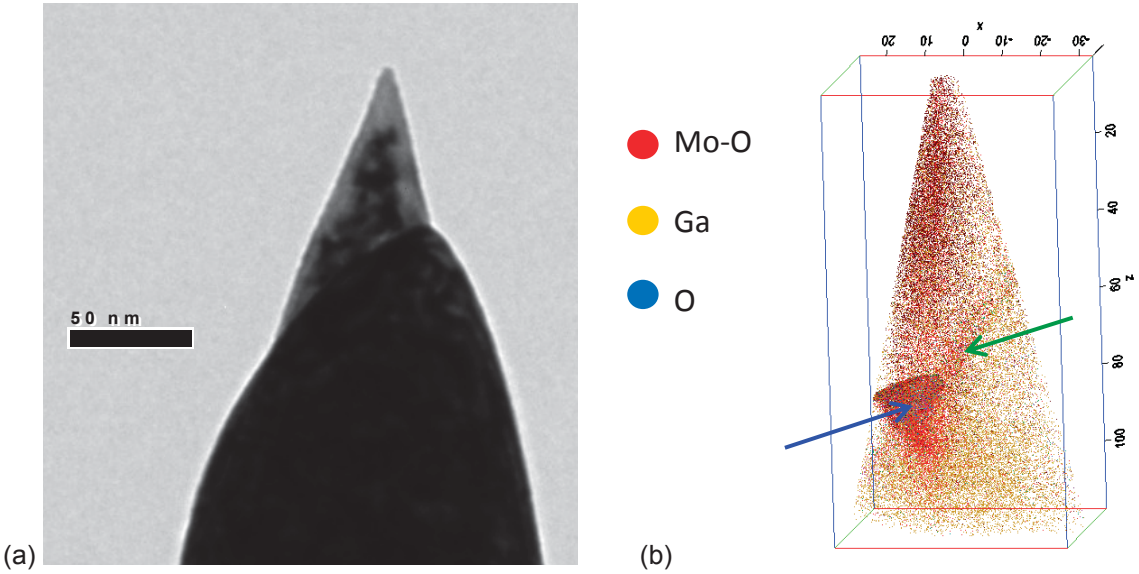

(a) (b)

Figure 4.7: TEM image of FIB prepared tip (a) bright field image (b) APT reconstruction of tip. The blue arrow in (b) marks a “segregated region”, the green arrow the grain boundary with segregations and the inset shows the color code for the ions/molecules detected. In the reconstruction all detected elements except of molybdenum-oxygen, gallium and oxygen are blanked.

The elements magnesium, oxygen, nitrogen, calcium, potassium, aluminum, barium, iron and silicon are concentrated in the segregated region which is marked by a blue arrow in Figure 4.7. Phosphor, nitrogen and oxygen were detected with the atom probe at the grain boundary (green arrow) as shown in the reconstruction of the same tip in Figure 4.8.

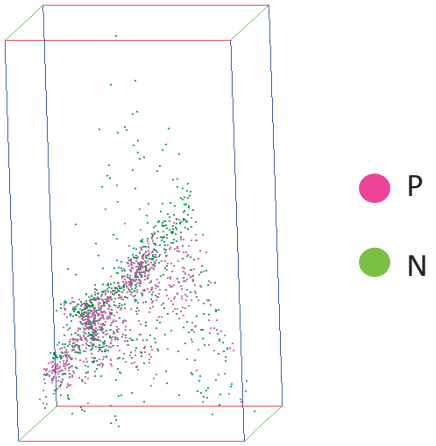

Figure 4.8: APT reconstruction of the grain boundary. The inset shows the color code for the ions/molecules detected. Molybdenum, molybdenum-oxygen, gallium, oxygen and the elements in the particle are blanked in the reconstruction. Only phosphor and nitrogen are visible in this reconstruction.

Molybdenum and molybdenum oxygen molecules are concentrated in the grain boundary, in the segregated region and on one side of the tip due to the direction of the laser beam. The concentration of gallium is also increased in the segregated region and at the grain boundary. The bulk composition as determined by ATP is summarized in Table 4.6.

Table 4.6: Bulk composition of sample out of sheet 1, recrystallized state, as determined by APT.

Element	Content [at.%]	Content [wt. %]
Mo	98,271	99,165%
Ga	0,882	0,647%
Mg	0,039	0,010%
O	0,591	0,099%
N	0,046	0,007%
P	0,031	0,010%
Ca	0,029	0,012%
K	0,025	0,010%
Al	0,009	0,003%
Ba	0,018	0,026%
H	0,039	0,000%
Fe	0,015	0,009%
Si	0,006	0,002%

To study the impurity elements in detail one-dimensional concentration profiles were created over special regions of interest. These regions of interest are shown in Figure 4.9. One area was selected to create a one-dimensional concentration profile over the "segregated region" and another one over the grain boundary. Furthermore, the impurity elements are clearly visible in the reconstruction in Figure 4.9. Only phosphor, nitrogen and oxygen were detected directly at the grain boundary, the other elements were accumulated in the "segregated region". The one-dimensional concentration profiles for the grain boundary shows that the content of oxygen, nitrogen and phosphor increase at around 10 nm. The other elements, which are listed in the bulk composition (see Table 4.7), are not present close to the grain boundary. The one-dimensional concentration profile for the "segregated region" shows that the content of magnesium, oxygen, nitrogen, calcium, potassium, aluminum, barium, iron, and silicon is increased in this area. Most of the potassium is on the upper part of this region and all other elements accumulate beneath.

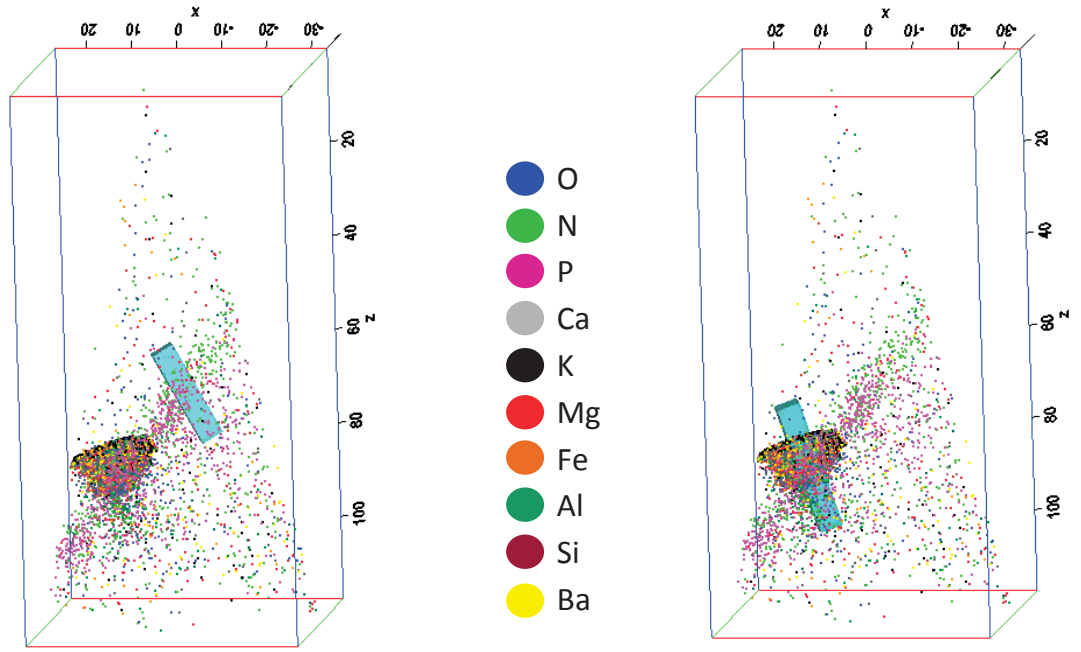

(a) (b)

Figure 4.9: APT reconstruction of the tip. (a) The region of interest for the one-dimensional concentration profile for the grain boundary is shown in turquois. (b) The region of interest for the one-dimensional concentration profile for the "segregated region" is indicated in turquois. The inset shows the color code for the ions/molecules detected. Mo and Ga atoms are blanked to point out the other elements.

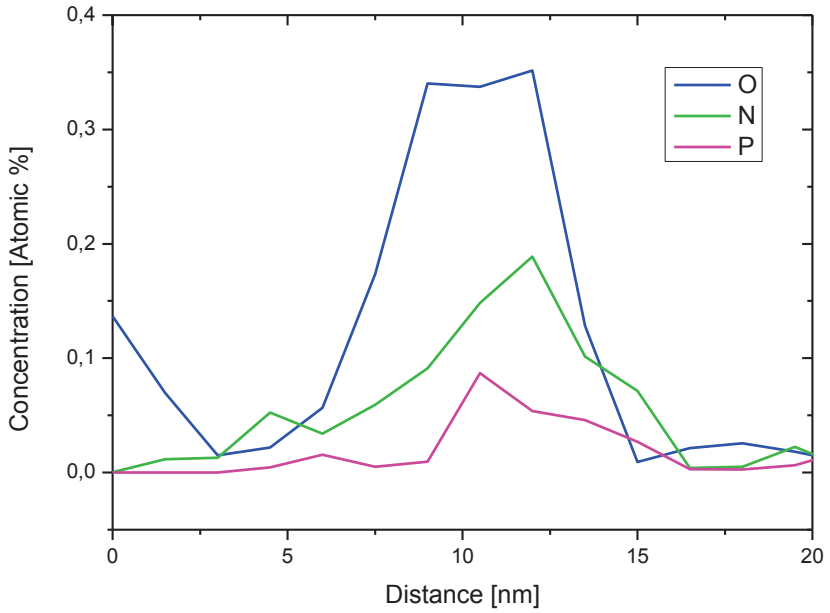

Figure 4.10: One-dimensional concentration profile of the region of interest marked in Figure 4.9 (a) in turquois. This profile runs through the grain boundary.

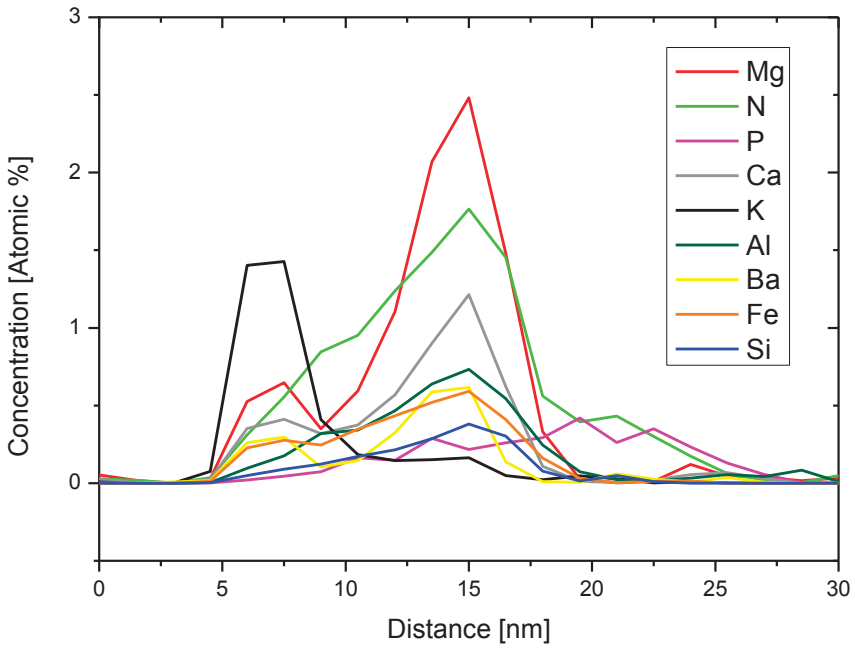

Figure 4.11: One-dimensional concentration profile of the region of interest marked in Figure 4.9 (b) in turquois. This profile runs through the “segregated region”. Molybdenum, oxygen and gallium are not shown to enhance the illustration of the other impurity elements.

4.2 AES measurements

In order to compare the obtained results of the atom probe analysis, AES was performed. AES is a useful tool to study grain boundary segregations on fracture surfaces [33].

Figure 4.12 shows a typical fracture surface of the recrystallized sheet 1. It is obvious that two kinds of fracture behaviour appear. Most of the area exhibits intergranular fracture, but transgranular failure is also visible. The circles indicate the point analyses for the AES spectra. To compare the results of the inter- and transgranular spectra, the curves were merged together as seen in Figure 4.13.

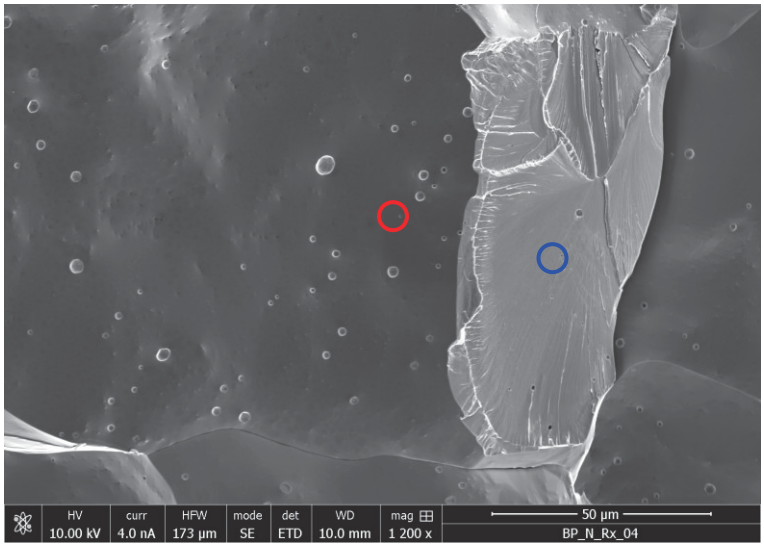

Figure 4.12: Fracture surface of sheet 1, recrystallized state, with trans- and intergranular fracture. The red circle indicates the position for the measurement of the AES spectrum of the intergranular fracture and blue circle of the transgranular fracture.

Figure 4.13 shows the AES spectra of the point analyses of the inter- (red) and transgranular (blue) fracture surfaces. To improve the visibility of the Auger electrons peaks, the differential signals of the curves were selected.

The Auger measurements show the characteristic molybdenum and oxygen peaks, but no impurities at the intergranular fracture surfaces. The inter- and transgranular fracture surfaces have no distinction in carbon, oxygen and potassium content, as shown in Figure 4.13. Therefore, no segregations of these elements are detected at the grain boundaries by AES. In the inset in the bottom right corner of Figure 4.13 it is apparent that the molybdenum peak at 125 eV for the intergranular analysis is sharper and higher than the peak for the transgranular analysis point. This led to the assumption that phosphor is present. Additionally, this peak shows a small shift towards a lower energy.

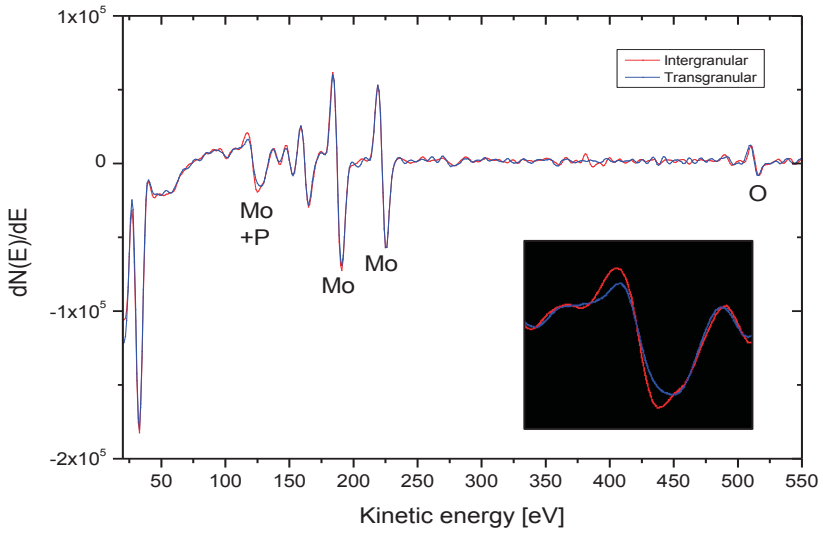

Figure 4.13: AES spectrum of sheet 1, recrystallized state, transgranular fracture (blue), intergranular fracture (red). The inset in the bottom right corner is the magnification of the molybdenum with phosphor peak at ~125 eV.

Furthermore, element mappings were carried out to study the location of the impurities. In Figure 4.15 it is apparent that oxygen and potassium are present in the micropores on the intercrystalline fracture surface. It should be noted that only in such pores a higher amount of these elements appeared.

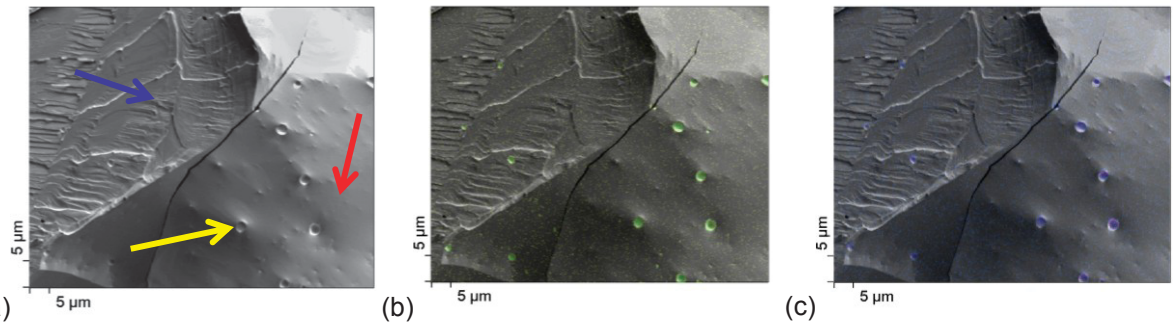

Figure 4.14: (a) SEM image of fracture surface of sheet 1, recrystallized state. The inter- (red) and transcrystalline (blue) fracture surface as well as the micropores (yellow) are marked with arrows. (b) Potassium element mapping. The appearance of potassium is indicated by green dots. (c) Oxygen element mapping. The appearance of oxygen is indicated by blue dots.

Figure 4.15 shows the SEM image of several micropores and the AES spectrum determined in such a pore. Oxygen and potassium are visible in the AES spectra of such micropores. Other elements as calcium, barium and phosphor are also detected in the pores, but their peaks are close to the noise level. Figure 4.16 shows another element mappings for potassium and oxygen. It is obvious that these elements occurred just in the micropores.

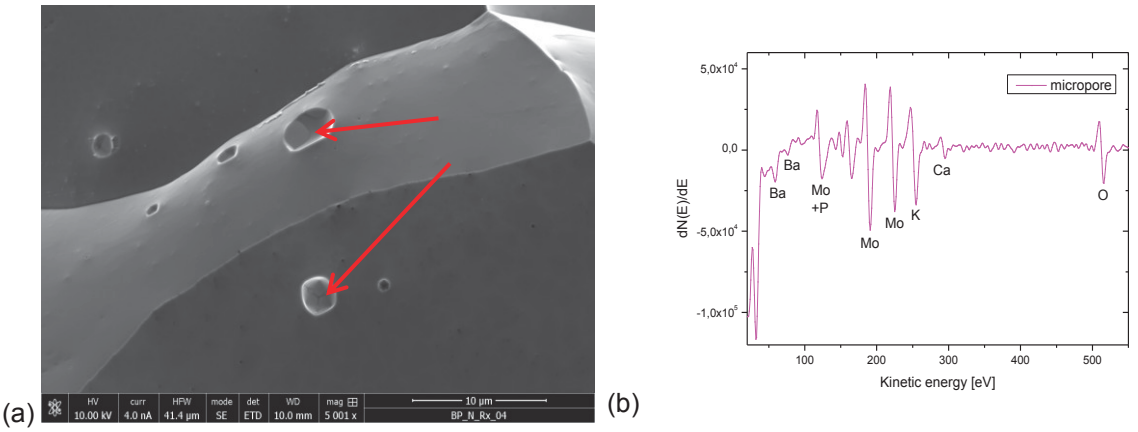

Figure 4.15: (a) SEM image of micropores in sheet 1, recrystallized state. Pores are marked by red arrows. (b) AES spectrum of a micropore in sheet 1, recrystallized state.

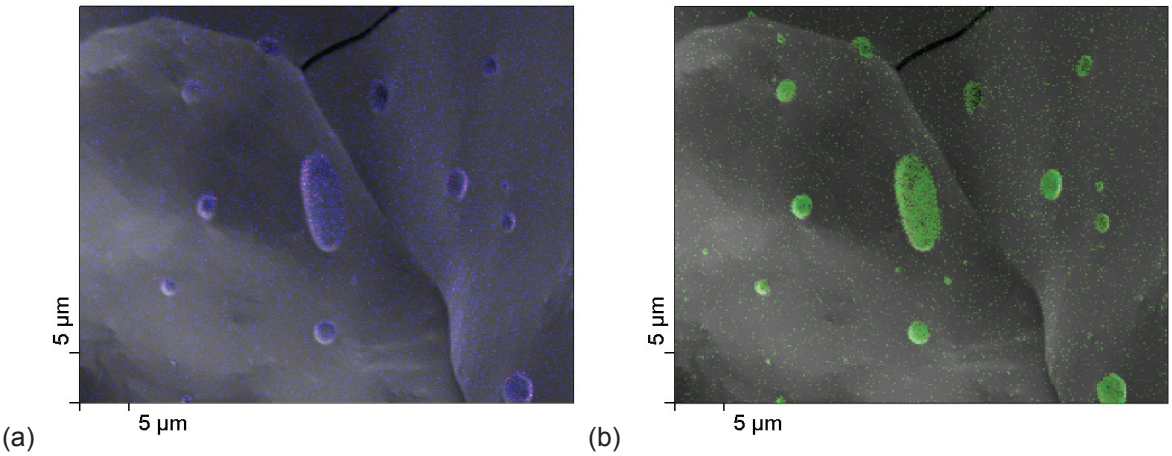

Figure 4.16: (a) Oxygen element mapping. The appearance of oxygen is indicated by blue dots. (b) Potassium element mapping. The appearance of potassium is indicated by green dots. Both elements were located in the micropores.

The AES investigations of sheet 2 led to the same results as for sheet 1. No distinct differences of the two sheets exist in the case of the AES measurements as shown in Figure 4.17. The spectrum shows the characteristic molybdenum and oxygen peaks, but no impurities at the intergranular fracture surfaces. Therefore, no segregations of these elements are detected at the grain boundaries. Oxygen and potassium occurred in the micropores, similar to sheet 1.

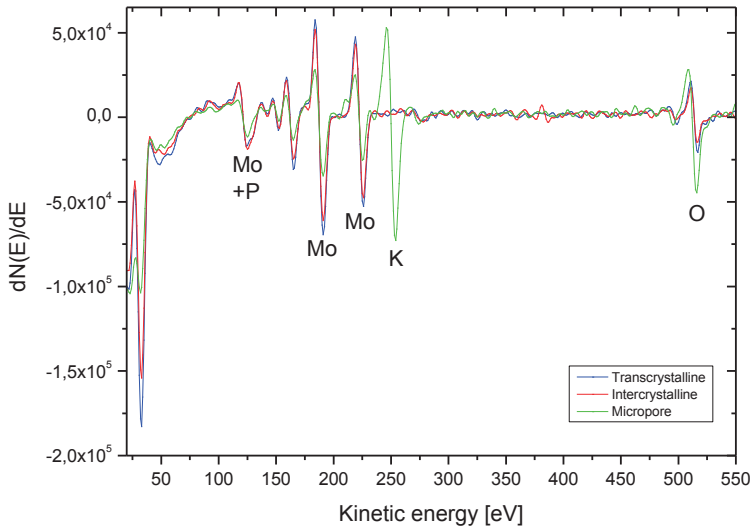

Figure 4.17: AES spectrum of sheet 2, recrystallized state, transgranular fracture (blue), intergranular fracture (red), micropore (green).

5 Discussion

Due to state-of-the-art industrial fabrication processes, it is possible to produce pure metals with impurity contents in parts per million ranges. However, impurities cannot be completely avoided during the production and subsequent processing. As shown in Table 3.1, technically pure molybdenum contains e.g. impurity elements such as potassium, barium, iron, aluminum, phosphor, magnesium, and silicon. Oxygen has a very low solubility and, therefore, tends to accumulate at grain boundaries [69]. Although chemical analyses as GDMS give information about the content of contaminating elements in a pure metal, the location of impurities in the bulk cannot be studied. Therefore, further analyses methods are necessary to study grain boundary segregations in molybdenum.

Due to the small amount of impurities in technically pure molybdenum, APT is a very suitable method to study grain boundaries. The APT with its atomic resolution and the possibility to detect all elements of the periodic system combined with site specific preparation techniques, e.g. FIB, is a powerful tool for investigations of the content and location of grain boundary segregations (see 2.2.2). Besides, interactions between elements can be studied. If an element accumulates at the grain boundary another one can be displaced.

However, the standard lift-out-technique (explained in 3.2.1) led to problems during the preparation process. The grain boundaries were visible on the surface of the samples, but their progression under the surface is not known as shown in Figure 3.3. It could be possible that the grain boundary exited the wedge after some nanometers below the surface. A three-dimensional view of the boundary was not possible. Furthermore, the visibility of the grain boundary during the annular milling process at radii lower than ~500 nm was very low and led to “blind preparation”. In case of the lift-outprepared tips there was no evidence if a boundary was in the sample especially if there were no segregations.

Furthermore, during the APT measurements of lift-out tips attached to silicon posts problems appeared. The different heat conductivities of molybdenum and silicon produced a heat accumulation which caused melting of several tips. However, also electro-polished tips were used as a post and led to better APT results as shown in

Table 4.3. Just the platinum weld weakened the stability of the tip during the measurement. The reconstruction of such tips showed no segregations. Due to the “blind preparation” it was not certain if the examined volume contained a “clean” grain boundary or not.

Additionally, electro-polished tips were produced and sharpened in the FIB. However, for these tips similar problems occurred as for the lift-out prepared tips. In the first annular milling steps the boundary was visible, but when the radii were below ~500 nm the grain boundary was not visible anymore (see Figure 4.4). However, these tips did not contain any weak points in the volume and no differences in heat conductivity appeared. Therefore, many ions were detected during the APT analyses as summarized in Table 4.4. The reconstruction of an electro-polished tip out of the as-deformed state (Figure 4.5) without TEM characterization showed no segregations. Due to the low visibility of the grain boundary in the tip after the milling process in the FIB/SEM it was not sure if a boundary was in the analyzed part of the tip.

Therefore, TEM analyses during the FIB preparation steps of pre-electro-polished tips were performed to give information about the exact position of the grain boundaries. In previous studies, this method has already been used to study grain and phase boundary segregations [40,74]. The FIB/TEM combination improved the preparation process due to the clear identification of the grain boundary in the tips as shown in Figure 4.6 and Figure 4.7. Furthermore, the shank and the radius of each tip could be measured exactly which was useful to define a correct reconstruction of the tip. Small protrusions on top of the tips were identified easily in the TEM (see Figure 3.26) and the tips were re-sharpened for a correct shape. These TEM analyses avoided non successful APT measurements.
The TEM images in Figure 4.6 show a boundary in the first 80 nm in the tip of the as-deformed state. Therefore, this grain boundary must be in the detected volume of the APT measurement of this tip. As depicted in Figure 4.6, the reconstruction showed no segregations at this grain boundary. This could be caused by two facts. Either the grain boundary does not contain any impurities or a subgrain boundary in the as-deformed state was measured. The same might be the case for the reconstruction of the tip without TEM characterization shown in Figure 4.5.

The recrystallized state only contained high-angle grain boundaries. A representative measurement (Figure 4.7) showed a boundary with a “segregated region” and grain boundary segregations. Phosphor, nitrogen and oxygen were detected at the grain boundary. The “segregated region”, possibly a former pore, contained the same

contaminating elements as measured by GDMS as for example phosphor, nitrogen or potassium. Most of the potassium is located in the upper part of this former pore and all other elements accumulated beneath. It is assumed that impurities are still located in such pores during the deformation process and diffuse along the grain boundary upon subsequent annealing treatment.

As reference analysis technique, AES was performed. In previous studies AES [6,11,12,29,33] and SIMS [63] had been the most frequently used methods to study such segregations on fracture surfaces. Due to the fact that B. Gludovatz [33] already performed AES for investigations of the fracture behavior of tungsten and the good spatial resolution of AES this technique was also used in this study.

Recrystallized molybdenum showed mostly intergranular fracture with some transgranular islands. The AES spectra of the inter- and trancrystalline areas were almost identical as shown in Figure 4.13. No differences of any element could be identified on the fracture surfaces. Furthermore, also sheet 1 and sheet 2 showed no distinctions in the spectra of the inter- and transgranular point analyses. Due to these results, no grain boundary segregations were visible according to the AES analyses. However, the molybdenum peak at ~125 eV of the transgranular fracture surface was shifted to lower energies and showed sharper contours in the intergranular fracture surface as shown in Figure 4.13. This peak shift led to the assumption that phosphor was present at the boundaries. Phosphor has a peak at 123 eV and pure molybdenum has a peak duplet with maxima at 124 eV and 129 eV in the AES spectrum. An overlay of these signals causes a shift of the resulting peak in the spectras.

B. Gludovatz [33] investigated the influence of impurities on the fracture behavior of tungsten and discovered phosphor at grain boundaries. However, he assumed that small amounts of impurities have no direct correlation to the fracture behavior in tungsten, but they do have an impact on the ductility in the form of initiators for cracks or pores. In this study potassium, calcium, barium, and oxygen were detected in the micropores of the molybdenum sheets at the grain boundaries. Especially, oxygen and potassium were present in the pores as shown in Figure 4.14, Figure 4.16 and Figure 4.17. These micropores originate from former sinter porosity which was closed during the deformation process of the sheets. Based on thermodynamic reasons, elements like potassium, oxygen and barium accumulated there as shown in Figure 4.15.

According to APT the segregation of phosphor at a grain boundary in the recrystallized sheet 1 correlates with the peak shift in the spectra of the intergranular fracture surfaces

of the AES measurements. Thus, both methods indicated phosphor at the grain boundaries. In case of AES a monolayer of atoms is necessary to get a reliable peak for an element. Individual atoms at an interface cannot be identified with AES. Due to the atomic resolution of the APT individual atoms are visible.

6 Conclusion

In this work, a site-specific APT investigation method with atomic resolution was developed to study grain boundary segregations in technically pure molybdenum.
It was shown that:

- The FIB preparation technique for APT tips combined with TEM characterization improved the preparation process and gave information about the exact position of the grain boundaries in the tip.
- Grain boundaries with and without segregations were found.
- Due to the almost atomic resolution of the APT small amounts of impurities were detectable as for example grain boundary segregations as well as “clean” grain boundaries in molybdenum.
- Complementary AES measurements showed chemically almost identical inter- and transgranular fracture surfaces. However, a peak shift at 125 eV indicates the presence of phosphor at the grain boundaries. This assumption correlates with the APT results.

The described preparation technique could be used in the future to study the content and location of grain boundary segregations in more detail in order to analyze the influence of these impurities on grain boundary strength and thus the mechanical properties of molybdenum.

References

[1] W. Martienssen, H. Warlimont, Springer Handbook of Condensed Matter and Materials Data, Springer, Berlin, Heidelberg, New York, 2005, pp. 91-116.

[2] J.S. Hirschhorn, Journal of the Less-Common Metals 5 (1963) 493-509.

[3] E. Pink, R. Eck, in:, R.W. Cahn, P. Haasen, E.J. Kramer, K.H. Matucha (Eds.), Materials Science and Technology, VCH, Weinheim, New York, Basel, Cambridge, Tokyo, 2006, pp. 591–638.

[4] S. Primig, H. Leitner, H. Clemens, A. Lorich, W. Knabl, R. Stickler, International Journal of Refractory Metals and Hard Materials 28 (2010) 703-708.

[5] J.H. Schneibel, M.P. Brady, J.J. Kruzic, R.O. Ritchie, Zeitschrift für Metallkunde 96 (2005) 632-637.

[6] A. Kumar, B.L. Eyre, Proceedings of the Royal Society A: Mathematical, Physical and Engineering Sciences 370 (1980) 431-458.

[7] E. Pink, Planseeberichte Für Pulvermetallurgie 13 (1965) 100-104.

[8] M. Miller, A. Bryhan, Materials Science and Engineering: A 327 (2002) 80-83.

[9] M. Miller, E. Kenik, M. Mousa, K. Russell, A. Bryhan, Scripta Materialia 46 (2002) 299-303.

[10] J.S. Braithwaite, P. Rez, Acta Materialia 53 (2005) 2715-2726.

[11] H. Kimura, Transactions of the Japan Institute of Metals 29 (1988) 521-539.

[12] F. Benesolvsky, P. Braun, W. Färber, E. Lassner, H. Petter, B. Tiles, F.P. Viehböck, Planseeberichte für Pulvermetallurgie 23 (1975) 101-120.

[13] G. Gottstein, Physikalische Grundlagen der Materialkunde, 3rd edition, Springer, Berlin-Heidelberg-New York, 2007, pp. 83-100.

[14] G. Gottstein, L.S. Shvindlerman, Grain Boundary Migration in Metals, Thermodynamics, Kinetics, Applications, 2nd edition, CRC Press, Taylor & Francis Group, pp. 111-115

[15] H. Gleiter, Korngrenzen in metallischen Werkstoffen, 2. Auflage, Gebrüder Borntraeger, Berlin-Stuttgart, 1977.

[16] F.J. Humphreys, M. Hatherly, in: Recrystallization and Related Annealing Phenomena, 2nd edition, Elsevier Science, Oxford, 2004, pp. 91–120.

[17] H. Sautter, H. Gleiter, G. Bäro, Acta Metallurgica 25 (1977) 467476.

[18] M. Winning, Phys. Stat. Sol. (a) 201 (2004) 2867-2879.

[19] F.J. Humphreys, M. Hatherly, in:, Recrystallization and Related Annealing Phenomena, 2nd edition, Elsevier Science, Oxford, 2004, pp. 121–168.

[20] H. Gleiter, B. Chalmers, Progress in Materials Science 16 (1972).

[21] R.P. Messmer, C.L. Briant, Acta Metallurgica 30 (1982) 457-467.

[22] R. Haydock, Journal of Physics C: Solid State Physics 14 (1981) 3807.

[23] E. Wachowicz, a. Kiejna, Computational Materials Science 43 (2008) 736-743.

[24] P. Lejèek, S. Hofmann, Rev. Adv. Mater. Sci 21 (2009) 27-34.

[25] B.W. Kempshall, B.I. Prenitzer, L. a. Giannuzzi, Scripta Materialia 47 (2002) 447- 451.

[26] L.-S. Chang, E. Rabkin, S. Hofmann, W. Gust, Acta Materialia 47 (1999) 2951- 2959.

[27] P. Lejcek, S. Hofmann, A. Krajnikov, Materials Science and Engineering: A 234-236 (1997) 283-286.

[28] S. Suzuki, H. Matsui, H. Kimura, Materials Science and Engineering 47 (1981) 209-216.

[29] A. Krajnikov, F. Morito, V. Slyunyaev, International Journal of Refractory & Hard Materials 15 (1997) 325-339.

[30] C.B. Geller, R.W. Smith, J.E. Hack, P. Saxe, E. Wimmer, Scripta Materialia 52 (2005) 205-210.

[31] S. Tsurekawa, T. Tanaka, H. Yoshinaga, Materials Science and Engineering: A, 176 (1994) 341-348.

[32] J.B. Brosse, R. Fillet, M. Biscondi, Scripta Metallurgica 15 (1981) 619-623.

[33] B. Gludovatz, S. Wurster, T. Weingärtner, a. Hoffmann, R. Pippan, Philosophical Magazine 91 (2011) 3006-3020.

[34] V. Hoffmann, M. Kasik, P.K. Robinson, C. Venzago, Analytical and Bioanalytical Chemistry 381 (2005) 173-188.

[35] A. Bogaerts, R. Gijbels, Spectrochimica Acta Part B 15 (1998) 1-42.

[36] F.L. King, J. Teng, R.E. Steiner, Journal of Mass Spectrometry 30 (1995) 1061.

[37] T. Nelis, J. Pallosi, Applied Spectroscopy Reviews 41 (2006) 227-258.

[38] P. Felfer, S.P. Ringer, J.M. Cairney, Ultramicroscopy 111 (2011) 435-439.

[39] F. Pérez-Willard, D. Wolde-Giorgis, T. Al-Kassab, G. a López, E.J. Mittemeijer, R. Kirchheim, D. Gerthsen, Micron 39 (2008) 45-52.

[40] J. Weidow, H.-O. Andrén, International Journal of Refractory Metals and Hard Materials 29 (2011) 38-43.

[41] M.K. Miller, R.G. Forbes, Materials Characterization 60 (2009) 461-469.

[42] M.K. Miller, Materials Characterization 44 (2000) 11-27.

[43] M.K. Miller, T.F. Kelly, K. Rajan, S.P. Ringer, Materials Today 15 (2012) 158-165.

[44] T.F. Kelly, M.K. Miller, The Review of Scientific Instruments 78 (2007) 031101.

[45] A. Cerezo, P.H. Clifton, M.J. Galtrey, C.J. Humphreys, T.F. Kelly, D.J. Larson, S. Lozano-Perez, Materials Today 10 (2007) 36-42.

[46] Imago Scientific Instruments, Product specification, http://www.atomic-force.com/Bilder/Imago/LEAPHRspecs.pdf [22/05/2013]

[47] E.W. Müller, T.T. Tsong, Field Ion Microscopy. Principles and Applications, American Elsevier Pub. Co., New York, 1969.

[48] M.K. Miller, G.D. Smith, Atom Probe Microanalysis: Principles and Applications to Materials Problems, MRS, Pittsburgh, 1989, pp. 37-59.

[49] A.J. Melmed, Journal of Vacuum Science & Technology B: Microelectronics and Nanometer Structures 9 (1991) 601-608.

[50] M.K. Miller, A. Cerezo, M.G. Hetherington, G.D.W. Smith, Atom Probe Field Ion Microscopy, Clarendon Press, Oxford, 1996, pp. 476-481.

[51] M.K. Miller, K.F. Russell, Ultramicroscopy 107 (2007) 761-766.

[52] P.R. Munroe, Materials Characterization 60 (2009) 2-13.

[53] N. Yao, Focused Ion Beam Systems, Basics and Applications, 1st edition., Cambridge University Press, 2007, pp. 1–30.

[54] M.K. Miller, K.F. Russell, G.B. Thompson, Ultramicroscopy 102 (2005) 287-298.

[55] M.. Phaneuf, Micron 30 (1999) 277-288.

[56] D.W. Saxey, J.M. Cairney, D. McGrouther, T. Honma, S.P. Ringer, Ultramicroscopy 107 (2007) 756-760.

[57] R. Rachbauer, S. Massl, E. Stergar, P. Felfer, P.H. Mayrhofer, Surface and Coatings Technology 204 (2010) 1811-1816.

[58] J.M. Cairney, D.W. Saxey, D. McGrouther, S.P. Ringer, Physica B 394 (2007) 267-269.

[59] H. Ilbach, in: Electron Spectroscopy for Surface Analysis, Springer, Berlin, Heidelberg, New York, 1977, pp. 1–11.

[60] H. Porter, D. Turner, Pure and Applied Chemistry 59 (1987) 1343-1406.

[61] G.C. Smith, Surface Analysis by Electron Spectroscopy, Measurement and Interpretation, Plenum Press, New York, 1994 pp. 33-35.

[62] P. Mueller, J. Vervoort, Secondary Ion Mass Spectrometer (SIMS), http://serc.carleton.edu/research_education/geochemsheets/techniques/SIMS.html [25/03/2013]

[63] A. Pebler, G.G. Sweeney, P.M. Castle, Metallurgical Transactions A 6 (1975) 991-996.

[64] P. Auger, J. Phys. Radium 6 (1925) 205-208.

[65] Nilsson A., Journal of Electron Spectroscopy and Related Phenomena 126 (2002) 3-42.

[66] R. Kosiba, Augerelektronenspektroskopie und niederenergetischer Ionenbeschuss von Siliziumkarbid, Technische Universität Ilmenau, 2004, http://d-nb.info/974555770/34 [05/22/2013].

[67] K.D. Childs, B.A. Carlson, L.A. La Vanier, J.F. Moulder, D.F. Paul, W.F. Stickle, D.G. Watson, Handbook of Auger Electron Spectroscopy, 3rd edition, Physical Electronics, Minnesota, 1995, pp. 2-7.

[68] G.C. Smith, Surface Analysis by Electron Spectroscopy, Measurement and Interpretation, Plenum Press, New York, 1994 pp. 93-98.

[69] S. Srivastava, L. Seigle, Metallurgical Transactions 5 (1974) 49.

[70] B. Simkin, M. Crimp, Ultramicroscopy 77 (1999) 65-75.

[71] W. McKenzie, E. Marquis, P. Munroe, Microscopy: Science, Technology, Applications and Education (2010) 1800-1810.

[72] H. Calderon, G. Kostorz, G. Ullrich, Materials Science and Engineering: A 160 (1993) 189-199.

[73] T. Weingärtner, private communication (2012)

[74] J. Weidow, H.-O. Andrén, Acta Materialia 58 (2010) 3888- 3894.

Proceeding: Planseeseminar 2013

Grain boundary segregations in technically pure molybdenum

K. Babinsky*, S. Primig*, W. Knabl**, A. Lorich**,T. Weingärtner***, J. Weidow****, H. Leitner*

* Montanuniversität Leoben, Department of Physical Metallurgy and Materials Testing, 8700 Leoben, Austria

** PLANSEE SE, 6600 Reutte, Austria

*** Institute for Applied Materials - Applied Materials Physics (IAM-AWP), Karlsruhe Institute of Technology (KIT), D-76344 Eggenstein-Leopoldshafen, Germany

**** Chalmers University of Technology, Department of Applied Physics, SE-412 96 Gothenburg, Sweden

Abstract

Molybdenum, a metal with excellent physical and chemical properties, is an interesting material for applications in lighting-technology, high performance electronics, high temperature furnace construction and sputtering targets. However, its applicability as a structural material is reduced because of the low brittle-to-ductile transition temperature, which is influenced mainly by the microstructure and the content of interstitial impurities.

In this study, it was attempted to analyze grain boundary segregations in technical pure molybdenum to understand the influence of these impurities on the resulting mechanical properties. Therefore, high sensitive analysis techniques such as atom probe tomography (APT), auger electron spectroscopy (AES) and chemical analysis methods were performed. APT is a powerful tool to study the concentration and location of segregations due to its almost atomic resolution for all elements. However, a site-specific sample preparation of grain boundaries with a dual focused ion beam/scanning electron microscope was required. Furthermore, AES analyzes were carried out to compare the obtained results with the APT measurements. The successful applicability due to the resolution of the individual methods is discussed.

Keywords

Molybdenum, grain boundary segregation, focused ion beam, auger electron spectroscopy, atom probe tomography

Introduction

Molybdenum is a metal with excellent physical and chemical properties for applications in lighting-technology, high performance electronics, high temperature furnace construction and sputtering targets. However, its fabrication and applicability as a structural material is limited because of the typical change of fracture behaviour due to the low brittle-to-ductile transition temperature near room-temperature [1]. In the deformed state at room-temperature molybdenum is ductile but recrystallization leads to room-temperature embrittlement which is believed to be caused by impurity segregations at grain boundaries [2]. The intergranular fracture is typical for bcc metals, like iron and molybdenum, but the influence of interstitial atoms on the mechanical properties is not well understood.

In the past, A. Kumar and B.L. Eyre [2] investigated binary molybdenum-oxygen and ternary molybdenum-oxygen-carbon alloys. These alloys showed intergranular fracture due to oxygen segregations. However, their measurements revealed that carbon has a beneficial effect on the grain boundary strength. Suzuki et al. [3] investigated the effect of recrystallization on the ductility of high purity molybdenum. He confirmed the increase of grain boundary strength due to the addition of carbon. V. Krajnikov et al. [4] studied welded molybdenum based alloys and suggested that in annealed molybdenum carbon strengthens the grain boundaries and reduces the oxygen segregation. Further investigations on bcc metals like molybdenum and iron were performed by H. Kimura [5]. Recrystallized molybdenum showed intergranular fracture even if the grain boundaries were free of impurities. Other authors assumed that the brittleness is an intrinsic property of molybdenum [6,7]. M.K. Miller et al. [8,9] investigated welded molybdenum alloys to understand the influence of the elements zirconium, carbon and boron. His atom probe tomography (APT) results showed no significant oxygen but zirconium, carbon and boron segregations at the grain boundaries. This replacement of segregation elements causes also a change in fracture mode from intergranular to transgranular failure [9].

An essential tool to analyze grain boundary segregations is auger electron spectroscopy (AES). It is possible to detect fractions of monolayers of elements on a surface to investigate the concentration and location of the impurities in the microstructure. Furthermore, new techniques for the preparation of atom probe tips by focused ion beam (FIB) expand the areas of application of the APT to analyze also grain boundaries with atomic resolution today. Especially with site-specific preparation, tips from a special region of interest in the bulk material can be produced. On the one hand, M.K. Miller [10] proposed the lift-out technique to prepare tips out of special regions such as grain boundaries. P. Felfer et al. [11], F. Pérez-Willard et al. [12] and J.M. Cairney et al. [13] used and improved these techniques. On the other hand, electro-polished tips can be produced and resharpened with a FIB [14]. For better visibility of a special region of interest in such tips transmission electron microscope (TEM) studies can support the sample preparation.

Although, M.K. Miller et al. [8,9] studied the influence of impurities in welded molybdenum alloys, technically pure molybdenum with no additional elements has not been examined so far.

In the present investigation, two different molybdenum sheets with different impurity concentrations were produced and studied by FIB/APT and AES as a complementary

technique. The main aim was to find the ideal preparation technique to analyze grain boundaries in molybdenum by APT. Additional measurements were performed in order to evaluate the feasibility of a combined FIB/TEM technique to produce specimens with grain boundaries in the first 100 nm of the tip.

Experimental and APT specimen preparation

The samples for the APT and AES analyzes were taken out from two sheets of technically pure molybdenum. They were produced and investigated in the as-deformed and recrystallized state. Table I summarizes the chemical composition of sheet 1 and 2. Sheet 2 has an increased potassium content. The sheets were produced by cold-isostatic pressing of molybdenum powder followed by a conventional sintering process. During the subsequent hot-rolling process, the final passes were carried out to assure a sufficient degree of deformation (>60%) for complete recrystallization upon annealing. This subsequent recrystallization annealing was performed for 2 h at 1300°C in hydrogen atmosphere. In Fig. 1 the microstructure of sheet 2 in the as-deformed and recrystallized state studied by electron channelling contrast imaging (ECCI) [15] in a Zeiss Evo 50 scanning electron microscope (SEM) is shown. The microstructure in Fig. 1b shows a recovered subgrain structure. Sheet 1 has a similar microstructure, for this reason no figure is shown here. The recrystallized grain size of sheet 1 was ~ 48 µm. Sheet 2 exhibits a grain size of ~55 µm parallel to the rolling direction. For the further tip preparation the microstructure, especially the grain sizes, had an influence for the preferred preparation method. The recrystallized state was used for the lift-out technique due to the good visibility of the grain boundaries as shown in Fig. 1. For the electro-polished tips the recrystallized and as-deformed states were taken.

Table I: Chemical compositions of the two sheets determined by Glow Discharge Mass Spectrometry (GDMS), sheet 2 has an increased potassium content. The absolute accurateness of applied GDMS is typically +/- factor of 2.

Sample	**Sheet 1**	**Sheet 2**
Element	**[µg/g]**	**[µg/g]**
C	< 8,5	< 6,5
O	≤ 12	< 5,9
N	<1,3	< 0,4
K	4	19
Ba	1,0	2,2
P	2,4	1,2
La	0,02	0,4
Fe	3,7	3,2
Si	1,1	1,3
Mg	0,9	1,1
Al	0,2	0,2
Ca	0,2	0,3
S	0,09	0,08
W	120	140

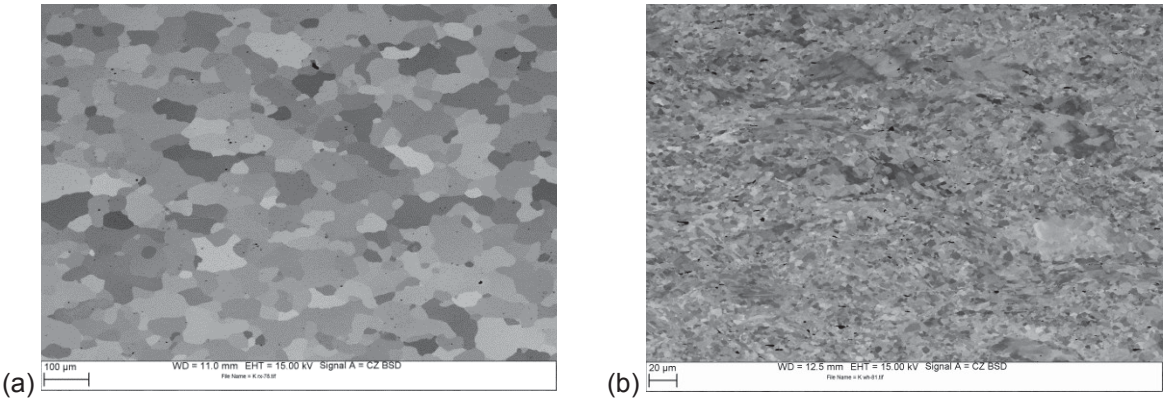

Fig. 1: Microstructure of sheet 2 in the (a) recrystallized and (b) as-deformed state studied by ECCI.

For the atom probe tip preparation two different techniques were used. Firstly, the lift-out technique proposed by Miller [10] was used to fabricate tips with a grain boundary out of the bulk material as shown in Fig. 2. For this method the recrystallized state was used due to the good visibility of the grain boundaries as shown in Fig. 1.

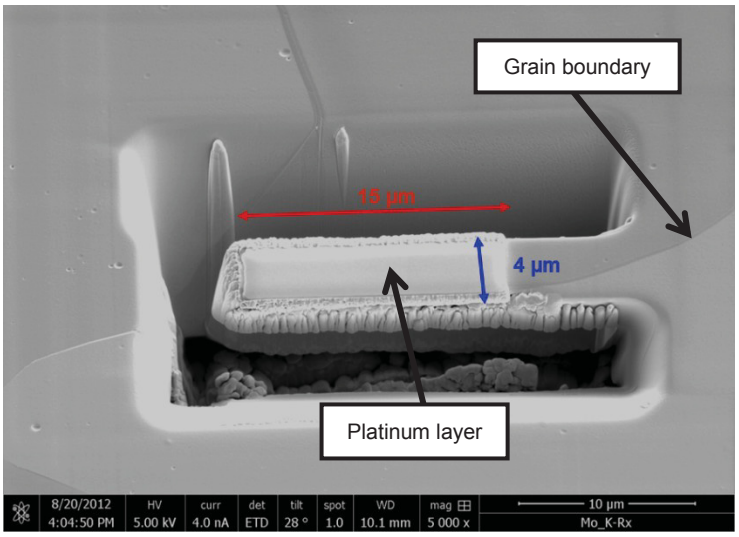

Fig. 2: Lift-out technique for the tip preparation of a wedge with a grain boundary. The grain boundary and the platinum layer are marked with arrows. The progression of the grain boundary under the surface is not visible.

The FIB work was performed on a FEI Versa 3D DualBeam (FIB/SEM) microscope with a Platinum gas injection system and an Omni probe 100-1 micromanipulator. All FIB preparation was carried out with an acceleration voltage of 30 kV and a suitable current for a balance between redeposition and cutting time. To protect the region of interest from gallium implantation, a platinum layer was deposited on the surface as shown in Fig. 2. After the clearance cutting, the wedges were lifted out with the micromanipulator and transferred to a post which is a silicon needle pad or a pre-electro-polished tip. The samples were attached to the post with platinum deposition weld [10]. Subsequently, annular milling was performed to give the tips the right radius and shank. In Fig. 3 a tip is shown after the first annular milling steps. The platinum layer, a grain boundary, the platinum weld and the post are marked with arrows.

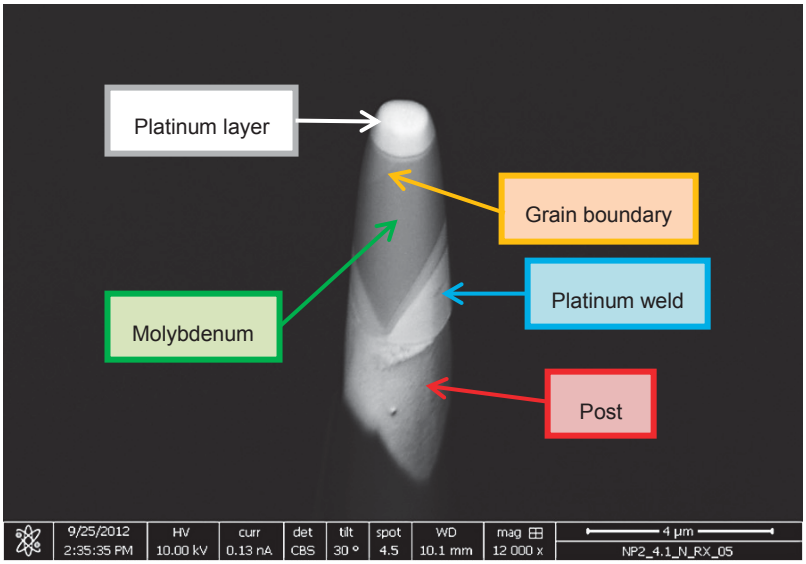

Fig. 3: FIB- prepared tip of molybdenum with a single grain boundary after the first annular milling steps.

The last preparation steps (cleaning) were carried out with an acceleration voltage of 5 and 2 kV in order to keep the gallium implantation low. Applying this preparation method, the grain boundaries were visible on the surface of the samples but their progression under the surface was not known as shown in Fig. 2.

Therefore, a second method was applied. Electro-polished tips were produced out of the as-deformed and recrystallized state [16] and sharpened with the FIB. As shown in Fig. 4, the grain boundary is clearly visible in the electro-polished tip after the first milling steps. With annular milling, the grain boundary should be positioned in the first 100 nm. However, it was always difficult to deduce if the grain boundary was in the volume examined or not for radii lower than ~500 nm.

In both methods, the poor visibility of the grain boundary during annular milling in the last preparations steps led to “blind preparation”. It was never clear if a boundary was in the first 100 nm.

(a)

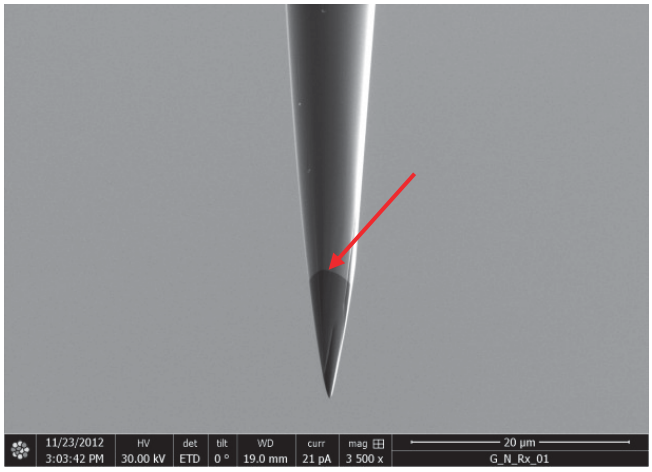

Fig. 4: FIB image of a sharpened electro-polished tip with a grain boundary at ~10 µm below the top of the tip. The arrow marks the grain boundary.

Therefore, a third method was applied. Electro-polished tips were produced [16], sharpened with a FIB and analyzed with a TEM to get information about the exact location of the grain boundary at small radii. This was carried out with a FEI Strata DB 235 DualBeam FIB at an acceleration voltage of 30 kV. The TEM analyzes were performed with a FEI Tecnai G2 TEM equipped with a LaB6 filament at 200 kV. The tips were characterized with the TEM between the milling steps to get information about the distance of the grain boundaries to the top of the tip. After sharpening in the FIB, the tips were analyzed in the TEM and removed to the FIB again to bring the grain boundary into the first 100 nm. A continuous change from FIB to TEM was necessary for this technique.
The ATP tips were measured with a LEAP 3000X HR from Cameca in laser mode. A laser energy of 0,6 nJ, a temperature of 60 K and a pulse rate of 200 kHz were used. The target evaporation rate was set to 0.5%. For the reconstruction of the analyses the IVAS 3.6.0 data software from Cameca was used.

As a complimentary method, AES was performed. The two sheets were analyzed after breaking them in-situ in the vacuum chamber. A PHI 680 Auger Nanoprobe with a Schottky field emission electron gun was used at the pressure between $1x10^{-9}$ mbar and $1x10^{-10}$ mbar. Due to fast deposition of oxygen on the surface, the measurements of oxygen were taken within 5 min of breaking the sample. Intergranular and transgranular fracture surfaces were characterized by point analyses to compare the difference between grain boundary and bulk material.

Results

Atom Probe Tomography

The lift-out technique proposed by Miller, was the first method applied to study a grain boundary in the atom probe. In accordance with publications it should be a perfect technique to have a grain boundary in the tip [11,12]. However, in this study many problems occurred. First of all the progression of the grain boundary under the surface was not known as seen in Fig. 2. The grain boundary was not visible anymore for lower radii than ~500 nm during the annular milling process. Additionally, there were problems with the heat discharge during APT measurements which caused melting of several lift-out tips.
In the case of the second method (electro-polished tips) similar problems appeared. The grain boundary was clearly visible in the tips for radii bigger than ~500 nm but lower radii led to “blind preparation” as well as for the lift-out technique. Fig. 5 shows two images of a tip during annular milling. In the first milling steps the grain boundary was visible, but after the last preparation steps the grain boundary disappeared. The reconstruction shown in Fig. 5c of an analyzed tip from the as-deformed state of sheet 2 showed just molybdenum and no impurities. No grain boundary was visible in this reconstruction. However, it cannot be deduced without doubt if a grain boundary without segregations was in the volume measured by APT in this case.

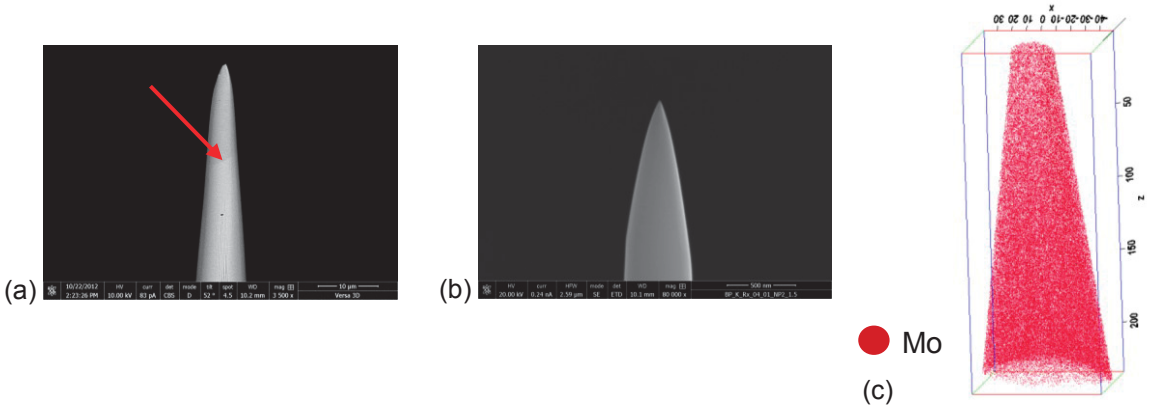

Fig. 5: (a) SEM image of a FIB- prepared tip of sheet 2, as-deformed state. The tip has a radius of ~2 µm after the first milling steps, the grain boundary is marked with an arrow. (b) SEM image of a FIB- prepared tip after the final annular milling with a tip radius of ~25 nm, the grain boundary is not visible anymore. (c) APT reconstruction of the tip after the atom probe measurement. It cannot be deduced without doubt if a grain boundary without segregations was in the measured volume. The inset in (c) shows the corresponding color code for the ions/molecules detected.

Due to the low visibility of the grain boundary during the last preparation steps with the FIB when the radii are below ~500 nm, TEM investigations were performed in order to determine the exact position of the boundary. In Fig. 6 the TEM bright (a) and dark field (b) images of a tip and the related reconstruction of the APT measurement (c) are shown. In the dark field image (b) only the lower part of the tip is visible. The tip was prepared out of sheet 2 in the as-deformed state. A grain boundary is visible within the first 100 nm, but the reconstruction shows no impurities at the grain boundary. Molybdenum, oxygen and gallium atoms are in the tip. The molybdenum and the molybdenum oxygen molecules were preferentially detected on one side of the tip because of the direction of the laser beam. Again, no segregation of impurities at the grain boundary can be seen (Fig. 6).
However, grain boundary segregations were found in some other specimens. The sample is from sheet 1 in the recrystallized state. Fig. 7 shows a TEM image (a) and the reconstruction (b) of a tip with a “particle” and a grain boundary with segregations.

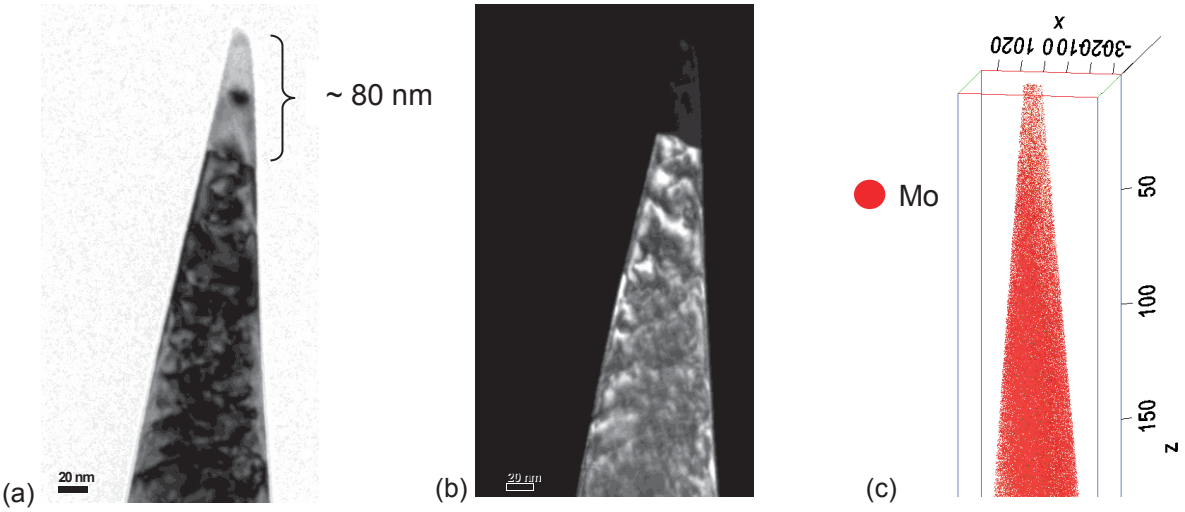

Fig. 6: TEM image of FIB prepared tip (a) bright field image (b) dark field image (c) APT reconstruction of the tip after the atom probe measurement. The inset in (c) shows the corresponding color code for the ions/molecules detected.

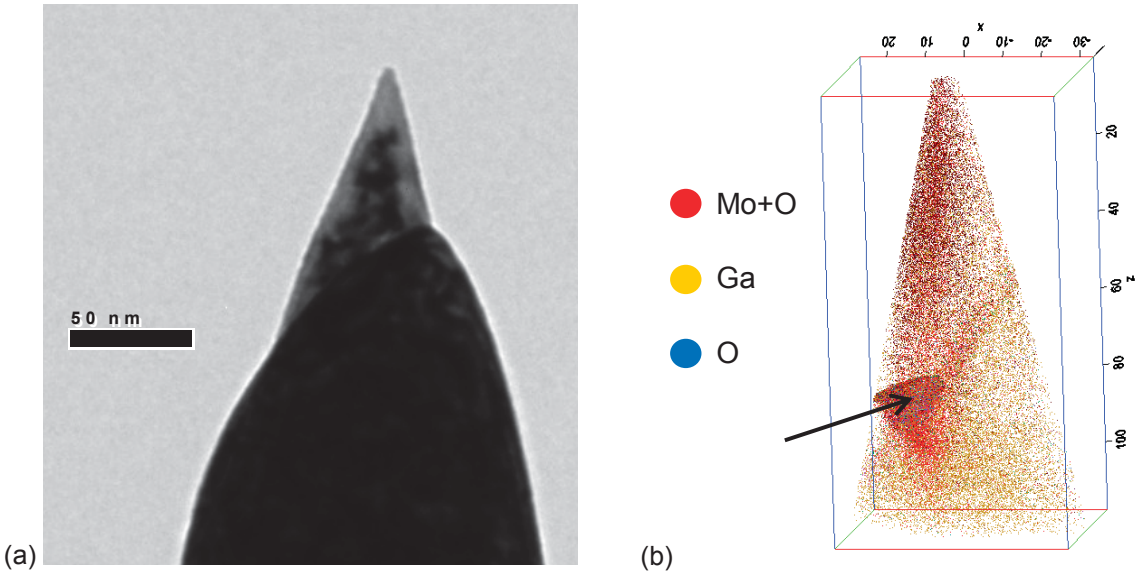

Fig. 7: TEM image of FIB prepared tip (a) bright field image (b) APT reconstruction of tip. The arrow in (b) marks a particle, the inset shows the color code for the ions/molecules detected. Mo atoms are blanked to point out the other elements.

The elements magnesium, oxygen, nitrogen, calcium, potassium, aluminum, barium, iron and silicon are concentrated in the particle which is marked by an arrow in Fig. 7. Phosphor and nitrogen were detected at the grain boundary with the atom probe as shown in the reconstruction of the same tip in Fig. 8.

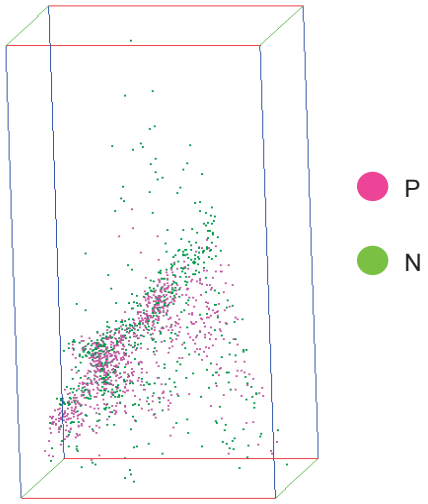

Fig. 8: APT reconstruction of the grain boundary. The Mo, MoO, Ga, O atoms and the elements in the particle are blanked in the reconstruction. The inset shows the color code for the ions/molecules detected.

The molybdenum and the molybdenum oxygen molecules are concentrated in the grain boundary, in the particle and on one side of the tip due to the direction of the laser beam. The concentration of gallium is also increased in the particle and at the grain boundary. The bulk composition as determined by ATP is shown in Table II.

Table II: Bulk composition of sample out of sheet 1, recrystallized state, as determined by APT.

Element	Content [at.%]
Mo	98,271
Ga	0,882
Mg	0,039
O	0,591
N	0,046
P	0,031
Ca	0,029
K	0,025
Al	0,009
Ba	0,018
H	0,039
Fe	0,015
Si	0,006

Auger Electron Spectroscopy

To compare the obtained results of the atom probe analysis, AES was performed. AES is a useful tool to study grain boundary segregations on fracture surfaces.
Fig. 9 shows a typical fracture surface of the recrystallized sheet 1. It can be seen that two kinds of fracture behaviour appear. Most of the area exhibits intergranular fracture, but transgranular failure is also visible. The circles indicate the point analyses for the AES spectra. To compare the results of the inter- and transgranular spectra, the curves were merged together as seen in Fig. 10.

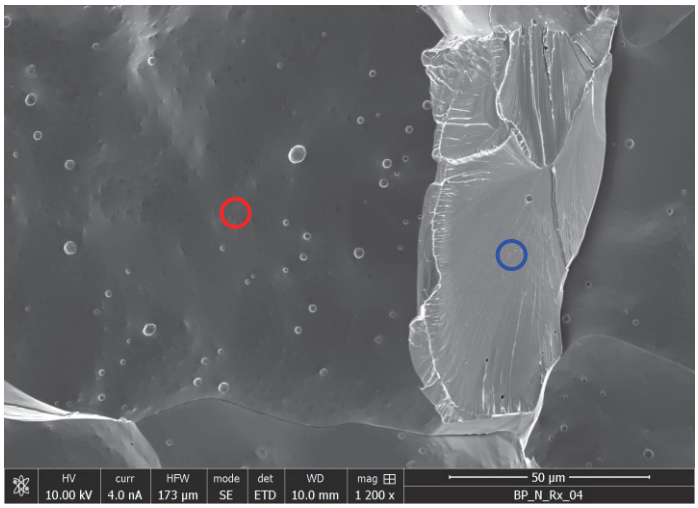

Fig. 9: Fracture surface of sheet 1, recrystallized state, with trans- and intergranular fracture. The red circle indicates the position for the measurement of the AES spectrum of the intergranular and blue of the transgranular fracture.

Fig. 10 shows the AES spectra of the point analyses of the inter- (red) and transgranular (blue) fracture surfaces. To improve the visibility of the auger electrons peaks, the differential signals of the curves were selected.

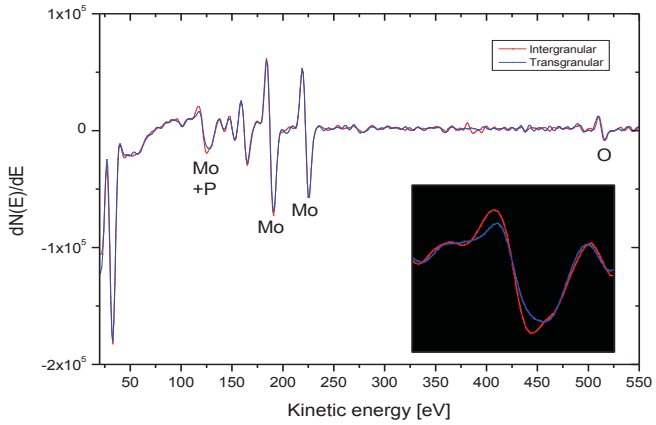

Fig. 10: AES spectrum of sheet 1, recrystallized state, transgranular fracture (blue), intergranular fracture (red). The inset in the bottom right corner is the magnification of the Mo +P peak at ~125 eV.

The auger measurements show the characteristic Mo and O peaks, but no impurities at the intergranular fracture surfaces. The inter- and transgranular fracture surfaces have no distinction in carbon, oxygen and potassium content, as shown in Fig. 10. Therefore, no segregations of these elements are detected at the grain boundaries by AES. In the inset in the bottom right corner of Fig. 10 it is apparent that the Mo peak at 125 eV for the intergranular analysis is sharper and higher than the peak for the transgranular analysis point. This led to the assumption that phosphor is present. Additionally, there is a little shift to the left visible at this peak. Fig. 11 shows the SEM image of several micropores and the AES spectrum determined in such a pore. Oxygen and potassium are visible in the AES spectra of such micropores. Other elements as calcium, barium and phosphor are sometimes also detected in the pores, but their peaks are close to the noise level.
The AES investigations of sheet 2 led to the same results as for sheet 1. No distinct differences of the two sheets exist in the case of the AES measurements.

(a)

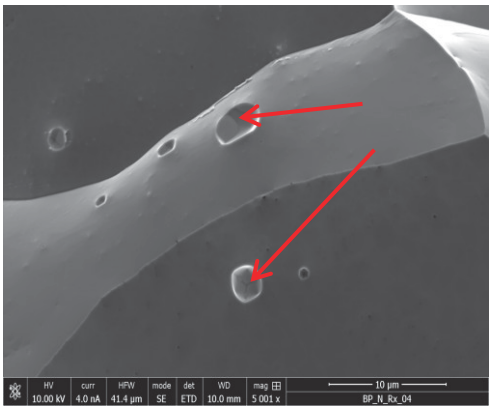

(b)

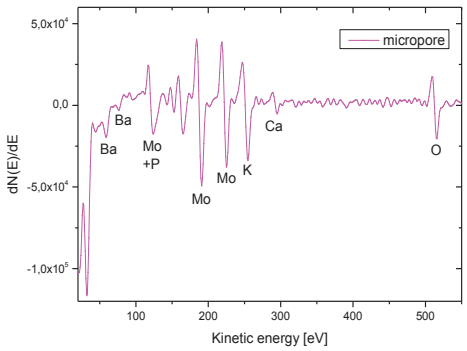

Fig. 11: (a) SEM image of micropores in sheet 1, recrystallized state. Pores are marked by red arrows. (b) AES spectrum of a micropore in sheet 1, recrystallized state.

Discussion

Due to state-of-the-art fabrication processes, it is possible to produce pure metals with impurity contents in parts per million ranges. However, impurities still cannot be completely avoided during the production and subsequent processing of pure metals. As shown in Table I, technically pure molybdenum contains e.g. impurity elements such as potassium, barium, iron, aluminium, phosphor, magnesium and silicon. In case of chemical analyzes as GDMS, the content of elements can be measured, but not their location in the microstructure to study the grain boundary segregations [17-19].
Due to the small amount of impurities in technically pure molybdenum, APT is a very suitable method to study these grain boundaries. The APT with its atomic resolution and the possibility to detect all elements of the periodic system, combined with site specific preparation techniques with the FIB is a powerful tool for investigations of the content and location of grain boundary segregations [9,11,12,14,20-22].
However, the standard lift-out-technique [10] led to problems during the preparation in this study. The grain boundaries were visible on the surface of the samples, but their progression

under the surface was not known as shown in Fig. 2. It could be possible that the grain boundary exited the wedge after some nanometers below the surface. A three dimensional view of the boundary was not possible. Furthermore, the visibility of the grain boundary during the annular milling process at radii lower than ~500 nm was very low and led to “blind preparation”. In case of the lift-out prepared tips there was no evidence, if a boundary was in the sample especially if there were no segregations. Additionally, electro-polished tips were produced and sharpened in the FIB. However, for these tips similar problems occurred as for the lift-out prepared tips. In the first annular milling steps the boundary was visible, but when the radii were below ~500 nm the grain boundary was not visible anymore.

The reconstruction of an electro-polished tip out of the as-deformed state (Fig. 5) without TEM characterization exhibited no segregations. Due to the low visibility of the grain boundary in the tip after the milling process in the FIB/SEM it was not sure if a boundary without segregations was in the analyzed part of the tip.

Therefore, TEM analysis in-between the FIB preparation steps of pre-electro-polished tips were performed to give information about the exact position of the grain boundaries. In the past, this method has already been used to study grain and phase boundary segregations [14,23]. The FIB/TEM combination improved the preparation process due to the clear identification of the grain boundary in the tips as shown in Fig. 6 and Fig. 7. Furthermore, the shank and the radius of each tip could be measured exactly which was useful to define a correct reconstruction of the tip.

The TEM images in Fig. 6 showed a boundary in the first 80 nm in the tip of the as-deformed state. Therefore, this grain boundary must be in the detected volume of the APT measurement of this tip. As visible in Fig. 6, the reconstruction showed no segregations at this grain boundary. This could be caused by two facts. Either the grain boundary does not contain any impurities or a subgrain boundary in the as-deformed state was measured. The same might be the case for the reconstruction of the tip without TEM characterization shown in Fig. 5.

The recrystallized state only contained high angle grain boundaries. A representative measurement (Fig. 7) showed a boundary with a “particle” and segregations. Phosphor and nitrogen were detected at the grain boundary. The “particle”, possibly a former pore, contained the same elements as measured by GDMS. It is assumed that impurities are still located in such pores during the deformation process and diffuse along the grain boundary upon subsequent annealing.

The AES measurements were performed as a complementary technique. In the past AES [2,4,5,24] and secondary ion mass spectroscopy (SIMS) [25] were the most frequently used methods to study such segregations. Nowadays, AES and SIMS are still used for such investigations of large as well as fine and ultra fine grains. With AES, the detections of monolayers of elements on a surface is possible [26]. In recrystallized technically pure molybdenum, the AES spectra of the transgranular and intergranular fracture surfaces were almost identical as shown in Fig. 10. No differences of the oxygen, potassium and carbon content could be identified on the fracture surfaces. Furthermore, sheet 1 and sheet 2 showed no differences in the spectra of the inter- and transgranular point analyses. Due to these results, no obvious grain boundary segregations were visible according to the AES

analyses. However, the molybdenum peak at ~125 eV of the transgranular fracture surface was shifted to lower energies and showed sharper contours in the intergranular fracture surface of all measurements. This peak shift led to the assumption that phosphor is present at the boundaries. Phosphor has a peak at 123 eV and pure molybdenum has a peak duplet with maxima at 124 eV and 129 eV in the AES spectrum. An overlay of these signals causes a shift of the resulting peak in the spectras.
B. Gludovatz [26] investigated the influence of impurities on the fracture behaviour of tungsten and discovered phosphor at the grain boundaries. Furthermore, his results showed that intergranular fracture does not have a direct relation to the differences in grain boundary impurities. Effects like the shape of grains, grain size distribution, texture, dislocation density and temperature influence the fracture behaviour more than grain boundary segregations. However, B. Gludovatz assumed that the impurities have no direct correlation to the fracture behaviour in tungsten, but they do have an impact on the ductility in the form of initiators for cracks or pores. In this study K, Ca, Ba and O were detected in the pores of the molybdenum sheets at the grain boundaries. These micropores were former sinter-pores which were compressed during the deformation process of the sheets. Based on energetical reasons, elements like potassium, oxygen and barium accumulated there as shown in Fig. 11.
According to the APT results the phosphor at the grain boundary of a tip out of the recrystallized sheet 1 correlates with the peak shift in the spectra of the intergranular fracture surfaces of the AES measurements. Both methods indicated phosphor at the grain boundaries. Due to the atomic resolution of the APT individual atoms are visible. For AES a monolayer of atoms is necessary to get a clear peak for an element. For this reason APT is the most applicable tool to study grain boundary segregations.

Conclusions

In this work, a site-specific APT investigation method with atomic resolution was found to study grain boundary segregations in molybdenum.
This work gives information about:

- The FIB preparation technique for APT tips combined with TEM characterisation improved the preparation process and gave information about the exact position of the grain boundaries in the tip.
- Grain boundaries with and without segregations were found.
- Due to the almost atomic resolution of the APT small amounts of impurities were detectable as for example grain boundary segregations as well as “clean” grain boundaries were found in molybdenum.
- Complementary AES measurements showed no difference in the inter- and transgranular fracture surfaces but a peak shift at 125 eV due to the presence of phosphor.

This preparation technique could be used in the future to study the content and location of grain boundary segregations in more detail in order to analyze the influence of impurities on the grain boundary strength.

Acknowledgements

This work (AES measurements) was carried out with the support of the European Community. We appreciate the support of the European Research Infrastructure EUMINAfab (funded under the FP7 specific programme Capacities, Grant Agreement Number 226460) and its partner the Karlsruhe Institute of Technology.

References

1. J.H. Schneibel, M.P. Brady, J.J. Kruzic and R.O. Ritchie, *Z. Metall.* ***96,*** 632-637, (2005)

2. A. Kumar and B. L. Eyre, *Proceedings of the Royal Society A: Mathematical, Physical and Engineering Sciences,* vol. 370, 431-458, (1980)

3. S. Suzuki, H. Matsui and H. Kimura, *Mater. Sci. Eng.* **47**, 209-216, (1981)

4. A.V. Krajnikov, F. Morito and V.N. Slyunyaev, *Int. J. Refract. Met. Hard Mater.* **15**, 325-339, (1997)

5. H. Kimura, *Transactions of the Japan Institute of Metals* **29**, 521-539, (1988)

6. C.B. Geller, R.W. Smith, J.E. Hack, P. Saxe and E. Wimmer, *Scr. Mater.* **52**, 205-210, (2005*)*

7. S. Tsurekawa, T. Tanaka and H. Yoshinaga, *Mater. Sci. Eng., A* **176**, 341-348, (1994)

8. M.K. Miller, E.A. Kenik, M.S. Mousa, K.F. Russell and A.J. Bryhan, *Scr. Mater.* **46**, 299–303, (2002)

9. M.K. Miller and A.J. Bryhan, *Mater.Sci. Eng., A* **327**, 80–83, (2002)

10. M.K. Miller, K.F. Russell and G.B. Thompson, *Ultramicroscopy* **102**, 287–298, (2005)

11. P. Felfer, S.P. Ringer and J.M. Cairney, *Ultramicroscopy* **111**, 435–439, (2011)

12. F. Pérez-Willard, D. Wolde-Giorgis, T. Al-Kassab, G.A. López, E.J. Mittemeijer, R. Kirchheim and D. Gerthsen, *Micron* **39** [5], 45–52, (2008)

13. J.M. Cairney, D.W. Saxey, D. McGrouther and S.P. Ringer, *Phys. B* **394** [2], 267–269, (2007)

14. J. Weidow and H.O. Andrén, *Int. J. Refract. Met. Hard Mater.* ***29*** [1], 38–43, (2011)

15. B.A. Simkin and M.A. Crimp, *Ultramicroscopy* **77,** 65-75, (1999)

16. T.F. Kelly and M.K. Miller, *Rev. Sci. Instrum.* **78** [3], 031101, (2007)

17. A. Bogaerts and R. Gijbels, *Spectrochim. Acta, Part B* **53**, 1-42, (1998)

18. F.L. King, J. Teng and R.E. Steiner, *J. Mass Spectrom.***30***,* 1061-1075, (1995)

19. V. Hoffmann, M.Kasik, P.K. Robinson and C. Venzago, *Anal. Bioanal. Chem.* **381** [1], 173–188, (2005)

20. M.K. Miller and R.G. Forbes, *Mater. Charact.* **60** [6], 461–469, (2009)

21. M.K. Miller, *Mater. Charact.* ***44*** [1–2], 11–27, (2000)

22. M.K. Miller, T.F. Kelly, K. Rajan and S.P. Ringer, *Materials Today* **15** [4], 158–165, (2012)

23. J. Weidow and H.O. Andrén, *Acta Mater.* **58** [11], 3888–3894, (2010)

24. F. Benesolvsky, P. Braun, W. Färber, E. Lassner, H. Petter, B. Tiles and F.P. Viehböck, *Planseebericht für Pulvermetallurgie,* Bd. 23, (1975)

25. A. Pebler, G.G. Sweeney and P.M. Castle , *Metall. Mater. Trans. A* **6** [5], 991-996, (1975)

26. B. Gludovatz, S. Wurster, T. Weingärtner, A. Hoffmann and R. Pippan, *Philos. Mag.* **9** *[22],* 3006–3020, (2011)